

ENSEMBLE SIMULATION AND FORECASTING OF SOUTH ASIAN MONSOON

by

Siraj Ul Islam

M.Phil. (Computational Physics), Quaid-e-Azam University, Pakistan, 2006

M.Sc. (Physics), Quaid-e-Azam University, Pakistan, 2003

B.Sc., Punjab University, Pakistan, 2000

DISSERTATION SUBMITTED IN PARTIAL FULFILLMENT OF
THE REQUIREMENTS FOR THE DEGREE OF
DOCTOR OF PHILOSOPHY
IN
NATURAL RESOURCES AND ENVIRONMENTAL STUDIES

UNIVERSITY OF NORTHERN BRITISH COLUMBIA

April 2015

© Siraj Ul Islam, 2015

UMI Number: 3663190

All rights reserved

INFORMATION TO ALL USERS

The quality of this reproduction is dependent upon the quality of the copy submitted.

In the unlikely event that the author did not send a complete manuscript and there are missing pages, these will be noted. Also, if material had to be removed, a note will indicate the deletion.

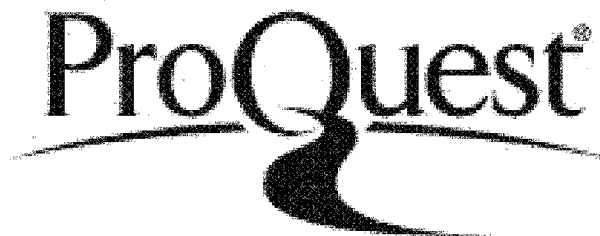


UMI 3663190

Published by ProQuest LLC 2015. Copyright in the Dissertation held by the Author.

Microform Edition © ProQuest LLC.

All rights reserved. This work is protected against unauthorized copying under Title 17, United States Code.



ProQuest LLC
789 East Eisenhower Parkway
P.O. Box 1346
Ann Arbor, MI 48106-1346

Abstract

This research thesis first examines the ability of Community Atmosphere Model (CAM) and Community Climate System Model (CCSM) in simulating the South Asian Monsoon (SAM) summer precipitation in a framework of ensemble. On this basis, the climatic relevant singular vectors (CSVs) perturbation theory is applied to investigate the optimal error growth of SAM seasonal forecast due to the uncertainties in the Pacific and Indian Oceans. Then, the ensemble prediction of SAM constructed by CSVs is evaluated, and further compared with one traditional ensemble method.

It is found that CAM4 adequately simulated monsoon precipitation, and considerably reduced systematic errors that occurred in its predecessors, although it tends to overestimate monsoon precipitation when compared with observations. In terms of monsoon interannual variability and its teleconnection with sea surface temperature (SST), CAM4 showed modest skill. In the CCSM4 coupled simulations, several aspects of the monsoon simulation are improved, including the cross-variability of simulated precipitation and SST. A significant improvement is seen in the spatial distribution of monsoon mean climatology where a too-heavy monsoon precipitation, which occurred in CAM4, is rectified. A detailed investigation of precipitation reduction, using sensitivity experiments, showed that the large systematic cold SST errors in the northern Indian Ocean reduces monsoon precipitation and delays the monsoon onset by weakening local evaporation.

The CSV analysis using CAM4 revealed that the SST uncertainties in Indian Ocean can result in much larger error growth of SAM seasonal forecast than those in the equatorial

Pacific Ocean. It is seen that the CSVs error growth rate changes significantly depending on the initial states whereas the CSVs patterns are insensitive to the initial conditions. The CAM4 comparison with CCSM4 coupled model indicated that the CSVs patterns from CAM4 are similar to those from CCSM4 while the error growth rate is lower in CAM4 than in CCSM4. CAM4 ensemble hindcasts, constructed using CSVs method and Time Lag Ensemble (TLE) method, for the period from 2000-2009, showed that the ensemble mean prediction by CSVs has a better skill than both TLE and control run prediction, indicating the merit of CSV for SAM ensemble forecast.

Overall, this thesis research has theoretical significance in understanding the uncertainties of SAM seasonal predictions and practical importance in developing a new ensemble method for SAM seasonal predictions.

Table of Contents

Abstract	ii
Table of Contents	iv
List of Tables	vii
List of Figures	viii
Glossary	xvii
Acknowledgements	xix
Chapter 1: Introduction	1
1.1 Asian Monsoon	1
1.2 Monsoon Simulations	3
1.3 Monsoon Seasonal Forecasts	5
1.3.1 Ensemble Strategies	7
1.4 Objectives and Outline	8
Chapter 2: Asian monsoon simulations by Community Climate Models CAM4 and CCSM4	12
2.1 Introduction	13
2.2 Models, Experiments and Validations	15
2.2.1 Models	15
2.2.2 Experimental Design	17
2.2.3 Validation	18
2.3 Simulations by CAM4 and CAM5	19
2.3.1 Climatological Mean and Seasonal Cycle	19
2.3.2 Monsoon Interannual Variability	26
2.3.2.1 Asian Monsoon Indices	26
2.3.2.2 Composite Analysis	28
2.3.3 Teleconnection of SAM with ENSO and IOD in CAM Simulations	30

2.4 Coupled Simulation using CSM4.....	33
2.4.1 Mean Climatology of CCSM4	33
2.4.2 Teleconnection of SAM with ENSO in Coupled Simulation.....	36
2.5 The Contribution of Air-Sea Interaction to SAM Simulation	39
2.6 Summary and Conclusions	42
Chapter 3: Further Investigation of ENSO-Monsoon relationship in climate models: A new validation strategy	68
3.1 Introduction	69
3.2 Models Experiments and Methodology	72
3.3 Results and Discussion	76
3.3.1 Composite Analysis	77
3.3.1.1 DJF-only Composite	78
3.3.1.2 JJAS-only Composite	79
3.3.1.3 DJF&JJAS Composite	80
3.3.2 Temporal Evolution of SST and SAM Rainfall	82
3.3.3 Response of Atmospheric Circulations	84
3.3.4 Response of Humidity and Land-Sea Thermal Contrast	85
3.3.5 Idealized Experiments	88
3.4 Summary and Conclusions	89
Chapter 4: Optimal error growth of South Asian Monsoon Forecast Associated with the uncertainties in the Sea Surface Temperature	104
4.1 Introduction	105
4.2 Method and Models	108
4.2.1 Estimation of Singular Vectors.....	108
4.2.2 Calculation of R and Application to the SAM Forecast System	110
4.2.3 Experimental Setups	111
4.2.4 Target Variable	114
4.3 The Optimal Error due to the SST Uncertainties in Indian and Pacific Oceans ..	114

4.3.1 Results during the 2000-2009 Period	115
4.3.2 Results during the 1980-2009 Period	118
4.3.3 The Results from the Coupled Model CCSM4	120
4.4 Sensitivity Experiments of CSV to some Parameters	121
4.4.1 Convergence of CSV with Number of EOFs	121
4.4.2 Convergence of CSV with Number of Ensemble Members	122
4.4.3 Validity of CSV	122
4.5 SAM Ensemble Forecast using CSVs	123
4.6 Summary and Conclusion	125
Chapter 5: Summary and Discussion	143
5.1 Thesis Summary	143
5.2 Discussion	147
References	150

List of Tables

Table 2.1: List of experiments used in CAM4, CAM5 and CCSM4 validation.	47
Table 2.2: Details of frequently used Asian monsoon indices. The correlation coefficient of simulated indices with observations is shown in last two columns.	49
Table 4.1: List of experiments used for CSV analysis including detail of perturbation domain, number of perturbation EOFs, number of ensembles and forecast years.	127

List of Figures

- Figure 1.1:** Seasonal (winter and summer) mean observed climatology of SAM precipitation (mm/day) and 850 mb wind vectors (m/s). 11
- Figure 2.1:** Seasonal mean (December–February; DJF) precipitation differences (biases) and root means square error (RMSE) from observation (CMAP) for (a, c) CAM4 and (b, d) CAM5. Units are in mm/day. 50
- Figure 2.2:** Same as Figure 2.1 but for the summer season (June–September; JJAS). 51
- Figure 2.3:** Seasonal mean (June–September; JJAS) precipitation and 850 mb winds from: (a) CAM4, (b) CAM5 and (c) observations (CMAP/NCEP). Precipitation (shaded) in mm/day and 850 mb winds (vectors) in m/s. 52
- Figure 2.4:** Time-latitude evolution of precipitation averaged over (50°–120°E) for: (a) CAM4, (b) CAM5 and (c) observations (CMAP). Precipitation annual cycle area averaged over SAM region is shown in (d). Units are in mm/day. 53
- Figure 2.5:** Seasonal mean (June–September; JJAS) precipitation differences from observations (CMAP) for: (a) CAM5_BAM (CAM5 with Bulk Aerosol Model (BAM) scheme), (b) CAM5_BAM_CAMRT (CAM5 with BAM and CAMRT (radiation) Schemes), (c) CAM5_BAM_HB (CAM5 with BAM and HB (Holtslag-Boville, boundary layer turbulence) schemes) and (d) CAM5_BAM_CAMRT_HB (CAM5 with BAM, HB and CAMRT schemes). Units are in mm/day. 54

Figure 2.6: Time series of Indian summer rainfall (ISR) index for (a) CMAP, (b) CAM4 and (c) CAM5. Details of this index are given in Table 2.1. The time series are normalized and thus unitless. 55

Figure 2.7: Time series of (a) Webster–Yang (WY) index, (b) Indian Monsoon index (IMI), (c) Western North Pacific monsoon (WNPM) index, and (d) South Asian monsoon (SAM_i) index of observation (CMAP/NCEP, black line), CAM4 (blue line) and CAM5 (red line). Details of all the indices are given in Table 2.1. The time series are normalized and thus unitless. 56

Figure 2.8: Difference between model (CAM4 and CAM5) and observed (NCEP) JJAS mean velocity potential ($10^{-6}/s$) and corresponding divergent winds (m/s) at (a), (b) 850 and (c), (d) 200 mb. 57

Figure 2.9: June–September (JJAS) anomaly precipitation composites of weak (1982, 1984, 1986, 1987, 1989 and 2002) and strong (1980, 1981, 1983, 1988, 1994, 1996, 1998 and 2007) monsoon years for (a, b) observation (CMAP), (c, d) CAM4 and (e, f) CAM5. Units are in mm/day. 58

Figure 2.10: The linear regression of observed June–September (JJAS) Niño3.4 ($-5^{\circ}S-5^{\circ}N, 120^{\circ}-170^{\circ}W$) and IOD ($(-10^{\circ}S-10^{\circ}N, 50^{\circ}-70^{\circ}E) - (-10^{\circ}S-0^{\circ}, 90^{\circ}-110^{\circ}E)$) SST indices with June–September (JJAS) observed and simulated precipitation and 850 mb winds. (a, b) observation (CMAP/NCEP), (c, d) CAM4 and (e, f) CAM5. 59

Figure 2.11: Lag-lead correlation of monthly mean precipitation with (a) Niño3.4 (-60

5°S–5°N, 120°–170°W) and (b) IOD ((-10°S–10°N, 50°–70°E) - (-10°S–0°, 90°–110°E)) indices. Area averaged (0°–40°N, 55°–100°E) time series (ISR) of observed CMAP (solid black line) precipitation, observed All-India Precipitation (AIR - dashed black line) time series and simulated (CAM4, solid blue line and CAM5, solid red line) time series are correlated with observed Niño3.4 and IOD SST indices. The month with negative (positive) sign indicate that SST leads (lags) the ISR with maximum lead of 12 months (1 year). Month 0 and 12 indicates June whereas month 4 and 8 correspond to February and October (minus sign for previous month). Correlations are calculated using a 5 month sliding window.

Figure 2.12: June–September (JJAS) mean differences between simulation and climatology (CMA) for: (a) CAM_CLIM (CAM4 climatology run) and (b) CCSM4. Shading corresponds to the precipitation difference in mm/day. 61

Figure 2.13: Same as Figure 2.3 but for CCSM4. Precipitation (shaded) in mm/day and 850 mb winds (vectors) in m/s. 62

Figure 2.14: The variance power spectrum for (a) observed SST (HadSST) and (b) CCSM4. Niño3.4 (-5°–5°N, 120°–170°W) SST index is in a solid red line and IOD ((-10°S–10°N, 50°–70°E) - (-10°S–0°, 90°–110°E)) index is in a solid blue line. 63

Figure 2.15: The linear regression (Top) of CCSM4 June–September (JJAS). Niño3.4 (-5°S–5°N, 120°–170°W) SST index with June–September (JJAS) simulated precipitation and 850 mb winds. Lag-lead correlation (Bottom) of CCSM4 monthly mean precipitation with CCSM4 Niño3.4 (-5°S–5°N, 120°–170°W) SST index. Area 64

averaged (0° – 40° N, 55° – 100° E) time series (ISR) of observed CMAP (solid black line) precipitation and observed All-India Precipitation (AIR - dashed black line) time series are correlated with observed Niño3.4 SST index. Correlations are calculated using a 5 month sliding window.

Figure 2.16: Seasonal SST differences between CCSM4 and observation (HadSST) 65
for a thirty year mean climatology during: (a) December–February (DJF), (b) March–
May (MAM), (c) June–August JJA and (d) September–November SON. The shading
corresponds to model SST bias in $^{\circ}$ C (red for warm SST and blue for cold SST).

Figure 2.17: June–September (JJAS) differences of (a) CAM4_POP (simulation 66
forced with the predicted SST of CCSM4) from observation (CMAP/NCEP) and (b)
from CCSM4. Shading corresponds to the difference in mm/day whereas vector
represents 850 mb winds in m/s.

Figure 2.18: Annual cycle of observed SST (HadSST, solid black line) and simulated 67
SST (CCSM4, blue dotted line and CCSM4_TR, red dotted line) over (a) Arabian Sea
(40° – 80° E, 7° – 30° N) and (b) Bay of Bengal (80° – 100° E, 7° – 30° N). (c) June–
September (JJAS) mean precipitation difference of CAM4_AS_BoB (CAM4
climatology SST run with SST modification in both Arabian Sea and Bay of Bengal)
from CAM4_CLIM (CAM4 climatology SST run). (d) Same as (c) but for CAM4_AS
run (with SST modification in Arabian Sea only). The shading corresponds to the
difference in mm/day.

Figure 3.1: Lag lead correlation of monthly mean SAM precipitation with (a) Niño3.4 92

(-5°S-5°N, 120°-170°W) and (b) northern Indian Ocean (NIO, 5°-25°N, 60°-100°E) indices. Area averaged (5°-25°N, 60°-100°E) time series (ISM) of observed CMAP (solid black line) precipitation, CAM4 (solid blue line) and CCSM4 (solid red line) time series are correlated with observed Niño3.4 and northern Indian Ocean SST indices except for CCSM4 case where CCSM4 simulated SST are used. Month with a negative (positive) sign indicate that SST leads (lags) the ISR with maximum lead of 12 months (1 year). Month 0 and 12 indicates June whereas month 4 and 8 correspond to February and October (minus sign for previous month). Correlations are calculated using a 5 monthly sliding window.

Figure 3.2: Bimonthly composite anomalies of observed SST (HadSST) for DJ, FM, AM, JJ, and AS (top to bottom). The 1st, 2nd and 3rd columns represent DJF-only, JJAS only and DJF&JJAS types respectively (see text for detail). Shading corresponds to the values in C. 93

Figure 3.3: Bimonthly composite anomalies of precipitation for DJ, FM, AM, JJ, and AS in DJF-only type (top to bottom). The 1st, 2nd and 3rd columns represent observed (CMAP), CAM4 and CCSM4 respectively. Shading corresponds to the values in mm/day while the contour shows their significance. 94

Figure 3.4: Same as Figure 3.3 but for the JJAS only type. 95

Figure 3.5: Same as Figure 3.3 but for the DJF&JJAS type. 96

Figure 3.6: Same as Figure 3.2 but for CCSM4 simulated SST. 97

Figure 3.7: Composite JJAS rainfall anomalies (mm/day) for the DJF-only type, 98
JJAS-only type and DJF&JJAS type based on observed (CMAP) and simulated
(CAM4 and CCSM4) precipitation.

Figure 3.8: Area averaged composite of normalized 3-month running mean anomalies 99
of Niño3.4 SST (green curves), northern Indian Ocean SST (NIO, red curves), CAM4
or CCSM4 precipitation (blue curves) and CMAP precipitation (IMR, black curves) in
(a) DJF-only type, (b) JJAS-only type, and (c) DJF&JJAS type. SST curves in left
column are from observation while right column SST curves are from CCSM4
simulation.

Figure 3.9: Observed (top), CAM4 (center) and CCSM4 (bottom) JJAS mean 100
composite anomalies of velocity potential and the corresponding divergent winds at
850 mb height (left column) and at 200 mb height (right column) for the JJAS-only
and DJF&JJAS types. Shading corresponds to the velocity potential in 10^6 s^{-1} and
vectors in m/s.

Figure 3.10: Composites of normalized 3-month running mean anomalies of surface 101
(2 m) air humidity over the region of 0° – 10° N and 50° – 80° E (solid curves) and 500–
200 mb thickness difference (10 m) between area 20° – 40° N, 50° – 100° E and 08° –
 20° N, 50° – 100° E in (a) DJF-only type, (b) JJAS-only type, and (c) DJF&JJAS type.
Left column is for CAM4 and observation while right column shows CCSM4
simulated curves.

Figure 3.11: Composite JJAS rainfall anomalies (mm/day) and 850 mb winds for the 102

DJF&JJAS type based on CAM4_ENSO_IO and CAM_ENSO experiments. See text for detail of the experiments.

Figure 3.12: JJAS mean composite anomalies of velocity potential and the corresponding divergent winds at 850 mb height (top left) and at 200 mb (top right) for DJF&JJAS type based on CAM4_ENSO_IO and CAM_ENSO experiments. (bottom) Composite of normalized 3-month running mean anomalies for CAM4_ENSO_IO and CAM4_ENSO experiments for DJF&JJAS type. 103

Figure 4.1: First three leading correlation EOFs patterns of the June SST over (a) Indian Ocean and (b) Pacific Ocean. These patterns are calculated from monthly observed SST for time period 1980 to 2009, and are added as perturbation in the instantaneous initial states of persistent SST. 128

Figure 4.2: SST anomalies for May of each forecast year. Each anomaly pattern is calculated based on the mean SST climatology of 1980-2009 and is kept persistent throughout the forecast. Units are in °C. 129

Figure 4.3: Mean climatology of June, July, August and September for Outgoing Longwave Radiation (OLR). NCEP OLR is shown in left column and CAM4 control run is in right column. Mean is calculated over the period 1980 to 2009. The shading corresponds to OLR values in W/m^2 . 130

Figure 4.4: The optimal leading Climatology relevant Singular Vectors (CSVs) of SST and corresponding OLR final patterns (FPs) of, optimized for 4 months (lead time 3) over the Indian Ocean domain. Each individual CSV and FP is shown starting from 131

year 2000 to 2009. The SST units are °C and OLR is in W/m^2

Figure 4.5: The first leading EOF patterns of the CSVs (left) and FPs (right) 132
computed over 10 individual CSV patterns for all the 4 lead times. CSVs are extracted
over Indian Ocean. The SST units are in °C and OLR is in W/m^2 .

Figure 4.6: Same as Figure 4.5 but for CSVs calculated over Pacific Ocean and 133
corresponding FPs over SAM region. The SST units are in °C and OLR is in W/m^2 .

Figure 4.7: Same as Figure 4.6 but for CSV calculated over combined Indian-Pacific 134
Ocean. Only FPs are shown here.

Figure 4.8: Annual variation of singular values averaged over all the lead times for (a) 135
Indian Ocean (b) Pacific Ocean and (c) IO30 experiments. (d) The lead time variation
of singular values over all the three cases (see text for detail).

Figure 4.9: Same as Figure 4.5 but for CSVs and FPs calculated over Indian Ocean 136
using IO30 experiment. 30 years CSVs and FPs are used for EOF analysis. The initial
conditions for IO30 experiment are generated using CAM4 prescribed SST run.

Figure 4.10: The spatial correlation for (a) Indian Ocean, (b) Pacific Ocean and (c) 137
IO30 experiments. It is computed between the first EOF mode (obtained by all CSVs)
and each individual CSV pattern, same as in Tang and Deng (2011).

Figure 4.11: (Spatial) The optimal leading SST CSVs and OLR FPs for lead time 0, 138
1, 2 and 3 obtained using CCSM4 model. The domain of perturbation is Indian Ocean.
The SST units are °C and OLR is in W/m^2 . (Line) Lead time variation of CCSM4

singular values over Indian Ocean.

Figure 4.12: Spatial patterns of the leading CSV (left column) based on the increasing number of EOFs used in the perturbation. 10 leading SST correlation EOFs are used by increasing EOFs from 3 to 10 in each CSV and FPs calculation. The optimization time is 4 months. Right column shows associated FPs. The SST units are in °C and OLR is in W/m^2 . 139

Figure 4.13: The convergence of the leading singular values with increasing number of ensemble members, optimized for 4 month time interval. Each color line represent individual year. In each year, 20 singular values are calculated by increasing the ensemble size from 1 to 20 in the CSV method. 140

Figure 4.14: Leading EOF of OLR FPs, at lead time 3, (a) calculated using CSV as perturbation and (b) estimated by applying linear propagator R to CSV i.e. by linear approximation. For (a), the difference of perturbed and control forecast is calculated each year and leading EOF is extracted using all the differences. In (b), EOF pattern is calculated using estimated FPs from linear approximation for all the 10 years (2000-2009). 141

Figure 4.15: Root mean square error (RMSE) of the SAM ensemble forecast generated using CSV perturbation. (a) RMSE calculated over 10 years (2000-2009 using observed initial conditions) whereas in (b) RMSE is for 30 years forecast (1980-2009 using CAM4 control initial conditions). Error bar is drawn using bootstrap method. 142

Glossary

AGCM:	Atmospheric General Circulation Model
APCC:	Asian Pacific Economic Cooperation (APEC) Climate Center
AIR:	All-India Rainfall
CGCM:	Coupled General Circulation Model
CAM:	Atmospheric General Circulation Model
CLIPAS:	Climate Prediction and its Application to Society
CCSM:	Community Climate System Model
CSV:	Climatology Relevant Singular Vector
CLM:	Community Land Model
CICE:	Community Ice Code
CPC:	Climate Prediction Center
CMAP:	CPC Merged Analysis of Precipitation
CFCAS:	Canadian Foundation for Climate and Atmospheric Sciences
DEMETER:	Development of a European Multimodel Ensemble System for Seasonal to Interannual Prediction
DJF:	December, January and February
FP:	Final Pattern
EOF:	Empirical Orthogonal Function
EAM:	East Asian Monsoon
ENSO:	El Niño/La Niña and the Southern Oscillation
HPC:	High Performance Computing Lab
IM:	Indian Monsoon

IOD:	Indian Ocean Dipole
ISR:	Indian Summer Rainfall
ITCZ:	Intertropical Convergence Zone
IPCC:	Intergovernmental Panel on Climate Change
GCM:	General Circulation Model
JJAS:	June, July, August and September
POP:	Parallel Ocean Program
PROVOST:	Prediction of climate variations on seasonal to interannual timescales
MAM:	Modal aerosol scheme
NSERC:	Natural Sciences and Engineering Research Council
NCEP:	National Centers for Environmental Prediction
NRES:	Natural Resource and Environmental Science
NCAR:	National Center for Atmospheric Research
NCL:	NCAR Command Language
RMSE:	Root mean square error
SAM:	South Asian Monsoon
SAMi:	South Asian Monsoon index
SST:	Sea Surface Temperature
SVD:	Singular Vector Decomposition
Westgrid:	Western Canada Research Grid
WNPM:	Western North Pacific Monsoon
WY:	Webster-Yang

Acknowledgements

I want to express immense gratitude to my supervisor Dr. Youmin Tang and co-supervisor Dr. Peter Jackson for their professional guidance and encouragement throughout this research work. Their keen interest, healthy discussion and enlightening criticism enabled me to complete my dissertation. Without their kind and valuable help, it would have almost been impossible for me to accomplish my research goals. I am deeply grateful to my committee members, Dr. Bill Merryfield, Dr. Erik Jensen and Dr. Jianbin Li for their valuable suggestions and support during my thesis research. I wish to say special thanks to the faculty of Natural Resource and Environmental Science (NRES) program for providing an excellent research environment in the department. I am also grateful to the anonymous reviewers for their comments and suggestions to improve my research manuscripts.

I extend my thanks to UNBC High Performance Computing (HPC) lab and Western Canada Research Grid (Westgrid) for providing supercomputing facilities for my research work. I am thankful to National Center for Atmospheric Research (NCAR) for providing models, input datasets and technical assistance. Thanks to NCAR Command Language (NCL) developers for helping me to unlock the power of data processing and graphical analysis.

Heartiest thanks to my lab members Dejian Yang, Manoj Nambiar, Waqar Younas, Yanjie Cheng and Zewang Deng for their helpful comments, suggestions, and discussions. Thanks are due to my friends in the Prince George community for being terrific fellows through the years. They never failed to show concern when things got stressful.

Finally I wish to record my deepest obligation to my parents, brothers, sister (late), and my wife (Ambreen) for their prayers, encouragement and love which always keep me on the right track. The debt I owe to my family has no measures.

This research work is supported by Canadian Foundation for Climate and Atmospheric Sciences (CFCAS) under research grant GR-7027 and Natural Sciences and Engineering Research Council (NSERC) Discovery grant to Dr. Youmin Tang.

Chapter 1

Introduction

1.1 Asian Monsoon

The monsoon is one of the most dynamic and prominent phenomena of the climate system and has a large effect on weather and climate anomalies at both local and global scales. The monsoon system is caused by the seasonal reversal of winds due to differential heating between land and ocean, and results in seasonally changing heavy precipitation patterns. The dominant monsoon systems around the globe are the Asian, Australian, African and American monsoons (Webster et al. 1998). Among these various monsoon systems, the Asian summer monsoon comprising the East Asian Monsoon (EAM) and the South Asian Monsoon (SAM) (Lau and Li 1984) receives the heaviest seasonal precipitation during the summer and has a major impact on global atmospheric circulations. The SAM region includes parts of the Arabian Sea, the Indian subcontinent and the Bay of Bengal (Goswami et al. 1999). The Indian subcontinent is characterized by complex topographical features, such as the Himalayas (in the north and north east) and the Western Ghats (along the western coast of India). Both of these extensive mountain ranges strongly influence the SAM circulations. Figure 1.1 shows the seasonal mean precipitation and 850 mb winds climatology over South Asian region. In winter (December, January and February, DJF), surface winds originating from South Asia sweep across the equator to meet the south Indian Ocean trades winds in the southern hemisphere. The precipitation in winter is therefore mostly confined in the equatorial Indian Ocean while the Indian subcontinent exhibits dry conditions. During the summer season in the months of June, July, August and September (JJAS), the winds blow

north from the Indian Ocean south of the Indian subcontinent and produce heavy rains contributing around 75% of SAM annual precipitation (Hastenrath and Polzin, 2004). The seasonal winds reversal in the SAM region is associated with the surface temperature contrast between the Indian subcontinent and the Indian Ocean, caused by the different responses of land and sea to solar heating during April and May. The onset of the summer monsoon involves the formation of a low pressure region over the SAM region that is called the monsoon trough. The monsoon trough is part of the Inter-tropical Convergence Zone (ITCZ) between the wind patterns of the southern and northern hemispheres.

The SAM precipitation has a very strong temporal and spatial variation due to the interaction between regional topography, atmospheric circulation and slowly varying sea surface temperature (SST) anomalies. Many studies have shown that the significant SAM variability is linked to El Niño/La Niña and the Southern Oscillation (ENSO), a coupled atmosphere-ocean interaction in the tropical Pacific Ocean (e.g. Sikka 1980; Rasmusson and Carpenter 1983 and Shukla 1987). ENSO influences the SAM regions either through teleconnections or ocean current anomalies, or both. In addition to ENSO, SST in the Indian Ocean also modulates SAM variability by means of the Indian Ocean Dipole (IOD; Saji et al. 1999; Ashok et al. 2001). Other large scale boundary conditions such as soil moisture (Webster et al. 1998) and snow cover (Bamzai and Shukla 1999; Kripalani and Kulkarni 1999) also modify the SAM dynamics, intensity and onset. Along with large-scale influences, it is seen that any variation in SAM is partially controlled by the atmospheric internal dynamics and random fluctuations (Krishnamurthy and Shukla 2000; Goswami and Ajaya 2001; Saha et al. 2011). The combination of these interactions result in significant interannual or intraseasonal variation of moisture availability over the SAM region either in the form of extreme dry or

wet conditions or delay of SAM onset. The relative role of these interactions makes SAM a very complex dynamical system.

Being a major convective system in the northern hemisphere, the fluctuations in SAM intensity affects the lives of many people due to the agrarian basis of their society. The fluctuations are often associated with delay in the onset of SAM, floods, droughts, and other climatic extremes (Malik et al. 2010) and significantly disturb the water budget, agricultural practice and economy of the region causing enormous socio-economic impacts. In view of the dependence of water availability and agriculture on monsoon precipitation, study of monsoon dynamics and its forecasting becomes an issue of immense importance. A detailed understanding of the role of different external forcing and other mechanisms that modulate SAM precipitation is essential for skillful SAM prediction as well as for societal and economical needs of the South Asian region. An accurate seasonal forecast can help planners mitigate the adverse impact in case of monsoon failure or amplification. Indeed, many efforts have been made to explain the process, variability and teleconnection of monsoon, but a full understanding of the phenomenon and its predictability is still being developed.

1.2 Monsoon Simulations

The past few decades have witnessed steady improvements in the skill of global climate models (GCMs) in simulating and forecasting climatic systems. These improvements have been largely driven by improved numerical schemes, increased resolution, advanced computational power and enhanced quality of input observational data. The overall framework of the dynamical simulations and predictions is refined based on comprehensive model tests and evaluation of their outputs on various time scales. The assessment of a

GCM's simulation determines the fidelity with which models simulate different processes and predict climate.

In the case of the SAM, conceptual models or fully coupled climate models are widely used either to understand the mechanisms involved in SAM development or to improve its prediction. Using these models, many studies have investigated the SAM dynamics focusing on different boundary condition such as SST (Webster et al. 1998; Ju and Slingo 1995; Wang et al. 2003; Loschnigg and Webster 2000; Lau and Nath 2000), snow (Shen et al. 1998; Becker et al. 2000; Jhun and Lee 2004; Wang et al. 2008), soil moisture (Webster et al. 1998; Walker and Rowntree, 1977; Shukla and Mintz 1982; Xue et al. 2006) and orography (Rodwell and Hoskins 1995; Wu et al. 2007). These studies, along with many others, have been beneficial in identifying the essential mechanisms and processes for SAM, and in improving its predictions.

While the current versions of GCMs can provide credible quantitative estimates of climate and can reasonably well simulate the mean climate anomalies of many variables (Randall et al. 2007, Liang et al. 2009, Lee et al. 2010 and many more), they still show significant discrepancies in simulating relatively local-scale systems such as monsoons (Kang et al. 2004; Wang et al. 2004; Covey et al. 2003; Meehl et al. 2005). The SAM variability at seasonal and interannual time scales and its relationship with local and remote SST anomalies are not well reproduced in Atmospheric General Circulation Models (AGCMs) due to large systematic errors (Kang and Shukla 2006). Although the Coupled General Circulation Model's (CGCMs) mean state could generally lead to a realistic simulation of monsoon teleconnection (Lau and Nath 2000; Turner et al. 2005), a comparison between uncoupled and coupled model simulations suggested that the SST biases of coupled models

partially offset the benefits of an active air-sea coupling (Cherchi and Navarra 2007, Islam et al. 2013). It is also seen that climate model bias in the mean state and in the seasonal cycle could degrade the seasonal and interannual predictability skill (Gadgil and Sajani 1998; Sperber et al. 2001). It is therefore important to identify systematic errors in monsoon simulations if the models are to be used for prediction. One of the key motivations of this thesis is therefore to study the systematic errors in uncoupled and coupled models for their simulations of the monsoon system.

1.3 Monsoon Seasonal Forecasts

The tremendous advances in understanding and modeling climate variability and predictability have made seasonal prediction an active area of research. As a result, seasonal climate prediction and the related uncertainties using multiple climate models has become operational (e.g. Lee et al. 2009; Palmer et al. 2004). In current dynamical models, the skill of seasonal predictions for some large scale climate systems is gradually approaching the practical limit of predictability that arise due to the nonlinear scale interactions inherent in the atmosphere (Lorenz 1963) coupled with an incomplete knowledge of the initial state (i.e. chaos) (Kang and Shukla, 2006). These nonlinear interactions impose a theoretical limit of predictability which can be defined as the performance of a perfect model with perfect initial conditions. The theoretical (inherent) and practical predictability limits have been estimated in many studies to investigate the potentials for further improvement in dynamical seasonal predictions (e.g. Younas and Tang, 2013).

Charney and Shukla (1981) initiated research on SAM seasonal forecasting by reporting its potential predictability due to the slowly varying boundary conditions such as SST. They

documented the potential to predict SAM beyond the limit of deterministic predictability based on its close interaction with tropical SST. Therefore the practical value of SAM prediction depends on the accurate simulation of forcing's signal (mainly from tropical SST) and its strength compared to the strength of unpredictable variability inherent in the atmosphere.

Substantial efforts have been devoted to the study of monsoon predictability either by dynamical models (e.g. Rajeevan et al. 2011; DelSole and Shukla, 2012) or by statistical models (e.g. Delsole and Shukla, 2002). While many different methodologies are used to improve the monsoon forecast skill, the overall skill of dynamical SAM forecast is considerably lower than the model forecast skill over the tropical central Pacific region (Kang et al. 2002; Wang et al. 2004). Different initiatives and projects such as “Asia-Pacific Economic Cooperation Climate Center/Climate Prediction and its Application to Society (APCC/CliPAS, Wang et al. 2009)”, “Development of a European Multimodel Ensemble System for Seasonal to Interannual Prediction (DEMETER, Palmer et al. 2004)” and “Prediction of climate variations on seasonal to interannual timescales (PROVOST, Doblus-Reyes et al. 2000)”, focusing seasonal dynamical forecasting, have been performed using both AGCMs (Tier-2) and CGCMs (Tier-1) models. The results from these projects have shown that the monsoon prediction skill mainly depends on simulation of accurate ENSO signal in models. The skill of dynamical model is limited mainly by inherent nonlinear characteristics of the atmosphere and the inaccurate simulation of ENSO signal (Kang et al. 2004). This means that the predictability of the SAM depends on the external forcing and the relative contributions from the internal dynamics of the monsoon system.

1.3.1 Ensemble Strategies

Practical forecast system requires a careful distinction between model errors and uncertainties in initial conditions (states). Both of these are not realistically distinguishable due to the reason that the estimation of the initial conditions involves a forecast model and thus model errors affects initial condition errors (Leutbecher and Palmer, 2008). Even if the models become perfect, the error due to the uncertainty involved in its initial conditions can degrade the forecast skill. The uncertainties present in initial states may grow due to the chaotic nature of the evolution equations of the dynamical system, thereby significantly decreasing the forecast skill. One practical approach to sample these uncertainties is to perturb the initial conditions and run the model with each set of perturbed initial conditions. The resulting group of model simulations is known as an ensemble which improves the forecasting skill by reducing the nonlinear error growth and averaging out unpredictable components. Many studies have shown that ensemble prediction can decrease the prediction error that originates from the uncertainty in initial conditions (Molteni and Palmer (1993) and Buizza et al. 1998; Yoo and Kang 2005).

Generating an ensemble in a forecast system can improve the forecast skill by diminishing the initial uncertainties. The crucial issue is to design a reliable ensemble forecast strategy that should include the major uncertainties of forecast initial states. Many operational centers still face the difficulty that the ensemble perturbations from a single model have limited error growth at early forecast lead times as compared to the amplitude of the mean error (Palmer et al. 2004; Saha et al. 2006, Kug et al. 2011). This implies that their initial perturbations used to generate ensemble may not be optimal.

Thus, it is necessary to treat the uncertainty of the initial condition in an optimal way so that error growth in the forecast system is realistic. It has been a challenge to construct optimal ensemble prediction at seasonal time scales for uncoupled or coupled GCM, which is another motivation for this thesis research.

1.4 Objectives and Outline

Correct representation of the monsoon system in climate models and its skillful seasonal prediction are important for different socioeconomic sectors of South Asia such as water resources, agriculture and other climate-sensitive sectors. This thesis therefore addresses the SAM simulations and ensemble forecasts using state of the art climate models. The long standing objective of this thesis research is to (i) investigate models' capability in predicting SAM variability and in characterizing its teleconnections to SST in Indian and Pacific Oceans and (ii) to improve SAM seasonal forecast skill by sampling initial uncertainties including the analysis of the factors and mechanisms that yield these uncertainties. The specific objectives of this research are:

- i) Evaluate models for their performance in reproducing SAM precipitation with an emphasis on the mean climatology, seasonal and interannual variability in an AGCM and a CGCM.
- ii) Analyze SAM variability and its relationship with SST anomalies of Indian and Pacific Oceans in the AGCM and CGCM, including a detailed comparison of SAM response to the prescribed SST in AGCM and to the simulated SST in CGCM. The impact of SST bias on the SAM simulation.

- iii) Implement and analyze the optimum perturbation growth of SAM seasonal prediction in AGCM and CGCM. Discuss the main characteristics of the leading optimum perturbation patterns, corresponding final patterns, and perturbation growth rate over the SAM region. Investigate the sensitivity of optimum perturbation and optimal growth to various parameters.
- iv) Use the optimum perturbation to generate ensemble SAM forecasts. Compare the forecast skill with that of control forecast and traditional ensemble forecast. Investigate the practicality of the optimum ensemble method in maximizing the benefit of dynamical forecasts.

To accomplish the above objectives, this thesis is organised into five chapters. Except Chapter 1, all chapters independently address one or more objectives described above. Chapter 2 is devoted to the detailed investigation of climate models performance in simulating SAM. Both coupled and uncoupled models are validated by means of different analysis and sensitivity experiments. Chapter 3 extends the analysis presented in Chapter 2, by further investigating the teleconnections of SAM to SST of the equatorial Pacific Ocean. The philosophy, design and implementation of optimum perturbation theory are discussed in Chapter 4 followed by the construction of ensemble SAM forecast. Chapter 5 summarizes and concludes the overall findings of the thesis.

This research has theoretical components and practical significance to seasonal forecast research. The results from this thesis may leverage existing activities and resources to achieve better and skillful SAM seasonal forecasting capability. Indeed, a good perturbation method for ensemble generation can effectively improve sub-seasonal to seasonal forecast of SAM

which could have profound impacts on agricultural planning, water resource management and other socio-economic activities of the region.

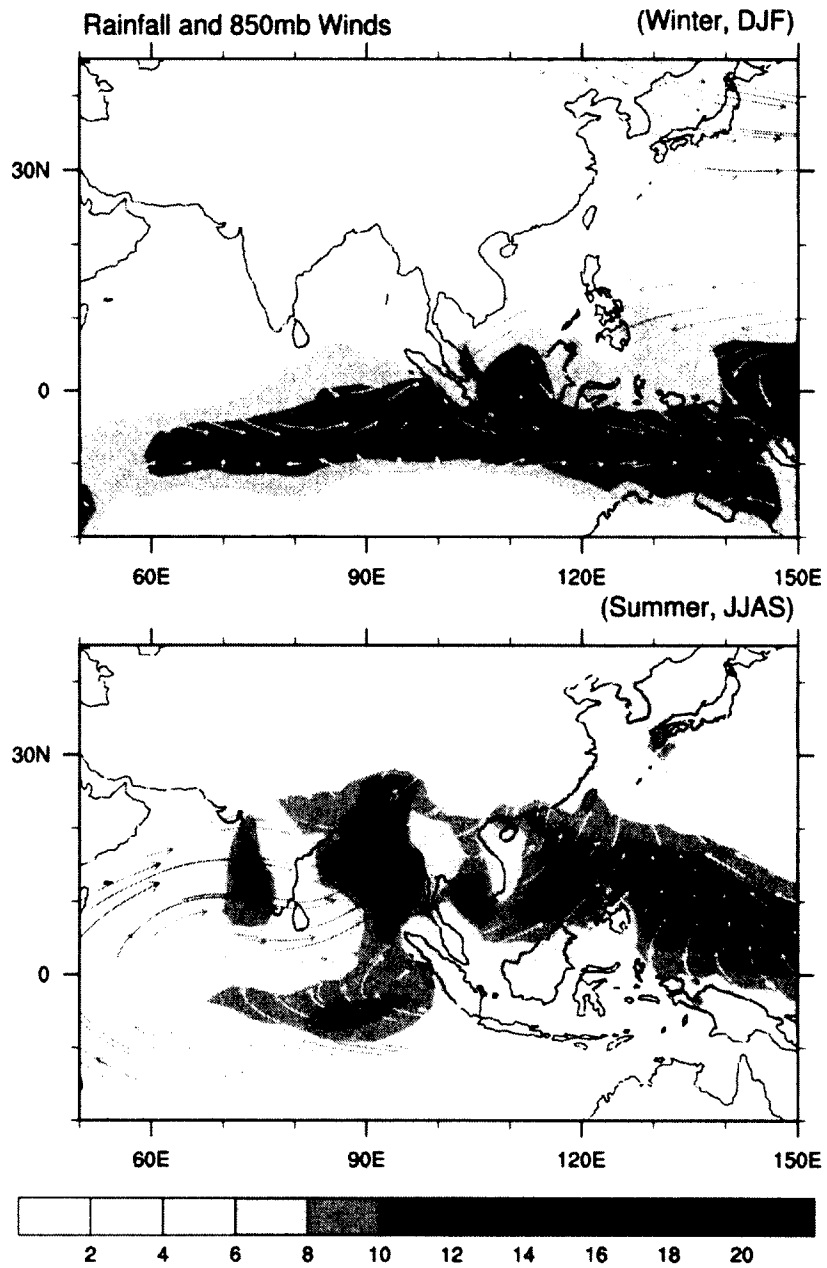


Figure 1.1: Seasonal (winter and summer) mean observed climatology of SAM precipitation (mm/day) and 850 mb wind vectors (m/s).

Chapter 2

Asian monsoon simulations by Community Climate Models

CAM4 and CCSM4

Islam S, Y Tang and P Jackson (2013), Asian monsoon simulations by Community Climate Models CAM4 and CCSM4, Climate Dynamics, DOI 10.1007/s00382-013-1752-6

Published version is available at:

<http://link.springer.com/article/10.1007%2Fs00382-013-1752-6>

This paper is reformatted to serve as Chapter 2 in the thesis.

2.1 Introduction

Climate models have been significantly improved in simulating the mean global climate (Randall et al. 2007) and in predicting climate anomalies at the seasonal time scale (Liang et al. 2009, Lee et al. 2010; Kang et al. 2002; Kang and Shukla 2006; Wang et al. 2004). These models are fairly good at simulating the average atmospheric state and large scale patterns, but poorer at simulating relatively small and local atmospheric systems such as the monsoon. In some of the studies such as Kang et al. 2004 and Wang et al. 2004, it has been seen that even when forced with observed SSTs, GCM performance over the SAM region is not satisfactory and presents large systematic biases. Even in CGCMs, which are believed to simulate the most realistic physical processes, there are notable biases in simulation of the mean climate and its variability (Covey et al. 2003; Meehl et al. 2005). These discrepancies include a Pacific cold bias, a double ITCZ, and a westward shift of ENSO variability (AchutaRao and Sperber 2006; Covey et al. 2000; Joseph and Nigam 2006). Gimeno et al. (2010) have shown that the northern Indian Ocean, particularly the Arabian Sea, is an important moisture source for SAM and any changes in Indian Ocean SSTs affect monsoon precipitation by altering the amount of moisture available for transport towards South Asia. Furthermore, due to the strong air-sea coupling over the Indian Ocean, any variation in the strength of the SAM precipitation influences the SST variation which significantly complicates the detection of monsoon variability related to other changes in the lower boundary of the atmosphere in the coupled model.

It has been a challenging issue to correctly simulate the monsoon variability at seasonal and interannual time scales (Annamalai et al. 2007; Dai 2006; Kripalani et al. 2007; Lin 2007; Waliser et al. 2007) and the relationship between SST anomalies and SAM precipitation

variability (Annamalai and Liu 2005; Meehl and Arblaster 2002; Shukla and Paolino 1983; Rasmusson and Carpenter 1983). The link between the SAM precipitation and ENSO has been well documented in both observations and modeling. For example, it has been reported that the warm phase (El Niño) is associated with weakening of the Indian monsoon and an overall reduction in SAM summer precipitation, while the cold phase (La Niña) is associated with the strengthening of the Indian monsoon and an enhancement of SAM summer precipitation (Kanamitsu and Krishnamurti, 1978; Krishnamurti et al. 1989; Palmer et al. 1992; Pant and Parthasarathy, 1981; Rasmusson and Carpenter, 1983; Shukla and Paolino, 1983; Shukla and Mooley, 1987; Sikka, 1999). Meehl et al. 2012, described SAM as a fully coupled air-sea-land system which can be better reproduced by air-sea coupled models. Many other studies also reported that coupled models perform better than atmosphere-only GCMs in simulating the SAM (e.g. Kumar et al. 2005 and Wang et al. 2005).

As discussed above, an intensive research effort has been made to improve simulation of monsoon systems by climate models and significant progress has been made in recent years. Among these models, community climate models developed at the US National Center for Atmospheric Research (NCAR) have played an important role in monsoon research due to their complete physical dynamics and easy implementation. In this chapter we evaluate NCAR climate models, i.e., the Community Atmosphere Model version 4 and version 5 (CAM4 and CAM5) and the Community Climate System Model version 4 (CCSM4).

The important factors affecting monsoon-SST relationships, such as air-sea coupling and SST bias, need to be studied in detail to determine the strengths and weaknesses of these models. A systematic evaluation is also important if these models are to be used for seasonal prediction or climate change studies. In this chapter, we therefore explore in detail the

strengths and limitations of CAM4, CAM5 and CCSM4 in simulating SAM precipitation with an emphasis on the mean climate, seasonal and interannual variability and the relationship between SAM and SST (local and remote). Our focus is placed on: 1) the SAM interannual variability when simulations are forced with observed SST; and 2) the role of air-sea coupling and the impact of SST bias in simulating the SAM. For the latter (2), using sensitivity experiments, we also examine the effect of northern Indian Ocean SST bias on SAM.

This chapter is organized as follows. Section 2.2 describes models, data and experiments. Section 2.3 investigates the mean climatology, annual cycle and evaluates simulated monsoon interannual variability in CAM4 and CAM5. Section 2.4 highlights and compares the coupled simulations of CAM4 (CCSM4) in terms of the mean climatology and SAM-SST relationship as well as the effect and importance of air-sea coupling over the SAM region. To address the effect of CCSM4 SST bias on the SAM precipitation, section 2.5 explores results of sensitivity experiments followed by summary and conclusions in section 2.6.

2.2 Models, Experiments and Validations

2.2.1 Models

Simulations are performed using the CAM4, CAM5 and CCSM4 models. These models are the latest in a succession of AGCMs and CGCMs that have been made widely available to the scientific community from NCAR. For the convenience of the reader we briefly introduce each model, but refer interested readers to the cited references for full details of each model. The models description discussed below is mostly adopted from the cited reference.

CAM4 (Neale et al. 2010a) is developed from CAM3 (Collins et al. 2006a) with modifications to the deep convection (Neale et al. 2008) and the polar cloud fraction in extremely cold conditions parameterization schemes (Vavrus et al. 2008). It uses an updated convection parameterization scheme (Neale et al. 2008; Richter and Rasch 2008). This model can be used with three different dynamic schemes (an Eulerian spectral scheme, a semi-Lagrangian scheme and a finite volume scheme) along with different resolution settings. CAM5 (Neale et al. 2010b) is modified significantly compared to CAM4, with a range of improvements in the representation of physical processes. It includes a new shallow convection scheme (Park and Bretheron, 2009), a stratiform cloud microphysical scheme (Morrison and Gettelman 2008), an updated radiation scheme (Lacono et al. 2008) and 3-mode modal aerosol scheme (MAM3) (Liu et al. 2011).

The CCSM4 (Gent et al. 2011) coupled model descended from its predecessors, CCSM3 (Collins et al. 2006b) and CCSM2 (Kiehl and Gent 2004). It contains a new coupler that exchanges fluxes and state information among all the embedded models. These embedded models are the CAM4 atmospheric model, the Community Land Model (CLM4), the Los Alamos Parallel Ocean Program ocean model version 2.2 (POP 2.2) (Smith and Gent 2002) and the Community Ice Code version 4 (CICE4) sea ice model (Hunke and Lipscomb, 2008). The CLM4 model operates on the same grids as the CAM4 model whereas CICE4 uses the same horizontal grid as POP 2.2, which has a displaced dipole grid (Smith and Kortas, 1995).

2.2.2 Experimental Design

A series of experiments are performed to achieve three goals: i) exploring and comparing the ability of CAM4, CAM5 and CCSM4 in simulating the SAM; ii) evaluating the contribution of air-sea coupling to the simulation and iii) investigating the effect of SST bias on SAM precipitation. These experiments can be generally categorized as below:

1) Control runs: Thirty-two years (1978 to 2008) of uncoupled simulations are performed using the CAM4 and CAM5 atmospheric models forced with observed prescribed SST (HadSST, Reynolds et al. 2002) and sea ice data. Both models share the same $1.9^\circ \times 2.5^\circ$ horizontal resolution using the finite volume dynamical core with 26 (in CAM4) and 30 (in CAM5¹) vertical levels using a hybrid terrain-following coordinate system. Higher resolution simulation of CAM4 and CAM5 models are also performed using $0.9^\circ \times 1.25^\circ$ horizontal grids.

2) Climatology run: CAM4 is also run forced with the climatological (based on the observations from 1982-2001) seasonal cycle of SST and sea ice for thirty years. This is referred to as CAM4_CLIM.

3) Coupled run: In the case of the CCSM4 coupled experiment, a 100-year coupled integration is performed using present day climatological forcing. The output of the last 30 years of this coupled simulation is used². In this simulation, the horizontal resolution of $1.9^\circ \times 2.5^\circ$ and finite volume grids in both the atmospheric and land model is used, whereas the

¹ CAM5 is run for different set of schemes. Standard run (control) of CAM5 has 30 vertical levels with all the default setting. The remaining set of CAM5 runs will be denoted with their particular name throughout the text.

² Subject to the computational conditions, the spin-up run was carried out 70 years, which basically allows atmospheric states to reach equilibrium.

ocean and ice models share the same $1^\circ \times 1^\circ$ resolution with a displaced pole grid. To facilitate comparison, observational datasets are interpolated to the resolution of model grids.

4) **Sensitivity runs:** Idealized experiments using different boundary forcings are performed with CAM4 and CAM5. Details of these experiments are given in the relevant sections.

Even a realistic model always contains random components and uncertainties such as those in boundary forcing or in initial conditions. To alleviate the impact of these random components and obtain a deterministic response of the model behavior to forcing (such as SST), an ensemble strategy is used for the above experiments except for the coupled run. For the control run, ensembles are constructed through perturbing the initial conditions, which allows us to separate the “SST-forced” (or external) response (Rowell et al. 1995). The perturbation of the initial conditions is performed by using the initial conditions lagged in time. For the climatology run, the same method is used to construct the ensembles. A detailed summary of all the experiments and the ensemble runs is given in Table 2.1. All simulation results from the control and climatology runs used for validation and presented in the next sections are the ensemble mean, unless otherwise indicated.

2.2.3 Validation

The following validation steps are used to examine the performance of the models in simulating the SAM monsoon: i) the simulated SAM precipitation and winds by the CAM4 and CAM5 control runs are compared against the observed counterparts in terms of climatology, interannual variability, and the relationship to SST. ii) The climatological means from the CAM4 runs are compared against those from CCSM4 to explore the effects of air-

sea coupling on the SAM simulation. iii) To explore the impact of SST bias on monsoon simulations, CAM4 forced with a modified SST climatology that contain SST bias, is compared with that forced with the observed SST climatology (CAM4_CLIM).

The metrics and methods used to evaluate the simulations include mean bias, Root Means Square Error (RMSE), variance, correlation and regression analysis. In all the uncoupled simulations, the first year of the integration output is discarded as a spin-up time, which is considered sufficient for atmospheric-only simulations. In the case of coupled runs, the first seventy years are discarded as the ocean model needs more time for equilibration. Observed precipitation data from the Climate Prediction Center (CPC) Merged Analysis of Precipitation (CMAP; Xie and Arkin 1997), on a $2.5^{\circ} \times 2.5^{\circ}$ grid, is used for validation of precipitation. The All-India Rainfall time series (AIR; Parthasarathy et al. 1995), which is a combination of 306 uniformly distributed station measurements, is also used in the analysis. National Centers for Environmental Prediction (NCEP; Kistler et al. 2001) reanalysis data, also on a $2.5^{\circ} \times 2.5^{\circ}$ grid, are used to validate winds. Observed SST (HadSST) data (Reynolds et al. 2002) are used for coupled model SST validation.

2.3 Simulations by CAM4 and CAM5

We first examine ensemble mean simulations of CAM4 and CAM5 forced with prescribed observed SST and sea ice data. Before focusing on the SAM, we evaluate both models over the tropical region.

2.3.1 Climatological Mean and Seasonal Cycle

The distribution of precipitation bias and root mean square error (RMSE) is shown in Figures 2.1 and 2.2 for the winter (December-February, DJF) and summer (June-September, JJAS)

seasons. The whole tropical region is shown to assess overall model differences. Bias and RMSE are calculated by comparing model output data with observations (CMAP) for the time period 1979-2008.

The model bias for winter (DJF) precipitation simulations are shown in Figures 2.1a and 2.1b for CAM4 and CAM5 respectively and their corresponding RMSE are shown in Figures 2.1c and 2.1d. Significant large-scale spatial biases (Figures 2.1a and 2.1b) over the equatorial Indian Ocean and western Pacific Ocean, along with many regional biases, are found in the CAM4 and CAM5 simulations. The magnitude of these biases is higher in CAM4 whereas CAM5, to a large extent, significantly rectifies them in its simulation. Major improvements in the CAM5 simulation occur over the South African land areas where the precipitation overestimation seen in the CAM4 simulation is diminished. The RMSE patterns (Figure 2.1c and 2.1d) further highlight the improved winter precipitation in the CAM5 simulation. In summer, when the precipitation activity over the northern hemisphere is enhanced, both models show biases in the form of excessive precipitation over the western Indian Ocean, central China, Himalayas, and in the subtropical Pacific Ocean (Figures 2.2a and 2.2b). Over the eastern Indian Ocean, China Sea, central parts of Africa and in the west and east Pacific Ocean, the models underestimate precipitation. The spatial patterns of bias from both models are similar, but the magnitude of biases is higher in the CAM4 simulation whereas CAM5 is able to reduce many regional biases. Compared to the land, biases are significantly higher over the ocean. High magnitudes of RMSE (Figure 2.2c and 2.2d) are seen over the northern Indian Ocean (Arabian Sea and Bay of Bengal) and the complex topography of the Himalayas. Similar to the winter, the summer RMSE of the CAM5 simulation is less than for the CAM4 simulation.

In general it is seen that, while both CAM4 and CAM5 are able to capture many observed features, they have regional biases somewhat similar to those in previous versions of these models (i.e., CAM3, reported in Meehl et al, 2006). In fact, these precipitation biases especially over the Indian and Pacific Oceans are probably an intrinsic error of the atmospheric model itself, as seen in Lin (2007) and our simulations. Compared to CAM4, the CAM5 simulation is improved with less regional bias.

The magnitudes of tropical two meter air temperature biases (not shown) in both CAM4 and CAM5 are small except in areas with complex topography such as the Himalayan region which is true for many climate models (IPCC 2007). Both models showed warm biases over most of the tropical domain. Larger errors are in regions of sharp elevation changes which may result simply from the mismatches between the models' smoothed topography and the actual topography.

As this chapter mainly focuses on the Asian region, the rest of the analyses for CAM4 and CAM5 include only the Asian domain, and particularly discuss the South Asian region (summer season only). Figure 2.3 shows seasonal mean summer precipitation and 850 mb winds for (a) CAM4, (b) CAM5 and (c) observations (CMAP/NCEP). In the observations, there are two precipitation maxima, with heavier precipitation around the northern Indian Ocean and a weaker precipitation maximum along the equatorial Indian Ocean. This is an important characteristic of the SAM precipitation. Although both of these maxima are captured in the models, significant large-scale biases such as excessive precipitation over the Arabian Sea and diminished precipitation in the central and the eastern Indian Ocean extending into the Bay of Bengal is seen. Simulations also show reduced precipitation along the coast of Bangladesh and excessive rain over the Western Ghats of India. CAM4 simulates

excessive precipitation in the eastern Arabian Sea and in the Bay of Bengal, with the maximum center around the Bay of Bengal shifted to the west of the observed maximum center. This is also true for the CAM5 simulation but the spatial magnitude of the precipitation is reduced bringing its climatology close to the observation. This same conclusion regarding the CAM4 simulation is found in the recent study by Meehl et al. (2012). Apart from the SAM region, the East Asian monsoon system, covering both subtropics and mid-latitudes, is well captured in both models. CAM5 shows spatial patterns similar to those observed whereas the CAM4 simulation is drier than observations over the South China Sea. All simulations show very good correlation and RMSE skill for the East Asian monsoon, compared with the SAM.

In the observed 850 mb winds pattern (Figure 2.3c), the most important features are the monsoon westerlies, the northward movement of the low pressure area from the Bay of Bengal and the low level jet stream passing across the equator onto the Indian subcontinent. The strengthening of westerly 850 mb winds during the summer monsoon seasons can be seen in both models (Figure 2.3a and 2.3b) over the 10°N to 2°5N latitude belt extending eastward from the western Arabian Sea through India and Bay of Bengal. The Bay of Bengal is considered as the moisture source of heavy precipitation events over the central South Asian region (Malik et al. 2010) and precipitation over this central region is mainly caused by the northward movement of low pressure areas from the Bay of Bengal (Lal et al. 1995). This interpretation is seen in both CAM4 and CAM5 simulations showing strong winds flowing from the Bay of Bengal to the north over central South Asia. In general, CAM4 and CAM5 are able to simulate the winds circulation at 850 mb (such as the equatorial monsoon

flow and lower level jet stream) realistically, even though there are biases in the strength of monsoon westerlies over the Indian region.

The simulation of the seasonal migration of the ITCZ is a challenging issue in GCMs. Many studies (such as Hack et al 1998 and Wu et al 2003) reported that most GCMs are unable to reproduce the seasonal migration of the ITCZ precipitation. Gadgil and Sajini (1998) found that the atmospheric models which can simulate the northward migration of the ITCZ can also simulate the interannual variation of the Indian monsoon reasonably well, whereas in models with poor SAM simulation, the ITCZ remains over the equatorial oceans in all seasons. Over the SAM region, the seasonal migration of the ITCZ from the equatorial region in winter to the heated continent in summer is the most important feature of seasonal variation. We therefore briefly analyze the seasonal migration of ITCZ in our model simulations by analyzing the mean January and July surface winds (not shown). It is found that this planetary scale feature of the general circulation is well captured by both CAM4 and CAM5. Also the location and strength of both the westerly jets over the northern Indian region during January and the tropical jets during July (early Monsoon) are fairly well reproduced in simulations which indicate that both models realistically capture the large shift of the ITCZ from January to July.

We have also performed simulations of CAM4 and CAM5 at higher resolution ($0.9^\circ \times 1.25^\circ$) to analyze the effect of better resolved topography (which is an important aspect for the simulation of precipitation). We found (not shown here) that increasing the resolution improved the simulation over areas of complex terrain such as the Western Ghats and Himalayas in the SAM region. The Western Ghats capture much of the rain on the Arabian Sea-facing side, while the other side of these mountains (to the east in southeastern India)

remains dry in the summer season. This is a localized effect and can only be seen in the higher resolution simulation. Also in the higher resolution run, heavy precipitation on the coastal mountain slopes of Myanmar, across the Bay of Bengal, is well simulated but with the same overestimation in the amount as seen in the lower resolution run. Also the excessive precipitation over the Tibetan Plateau in CAM4 (also the case in CAM5) is reduced in its higher resolution simulation. Both higher resolution simulations are somewhat closer to observations for the complex terrain regions of the SAM.

The seasonal evolution of SAM precipitation is examined in time-latitude diagrams averaged over the SAM longitudes (50° to 120° E) for observations, CAM4 and CAM5 (Figure 2.4). In the observations (Figure 2.4c), a well-defined seasonal precipitation pattern that varies with latitude and moves significantly northward from 5° N in winter to 20° N in summer is visible. In models (Figure 2.4a and 2.4b), the northward shift of precipitation starting in winter and reaching a maximum in summer is well captured but there are considerable systematic errors such as the simulated summer precipitation northward extent reaching too far north with a second maximum around 30° N. In the CAM4 and CAM5 simulations, the precipitation reaches a maximum at 15° N and exhibits an essentially realistic seasonal migration, but the simulations have heavier than observed precipitation over the Western Ghats. The overestimation is higher in CAM4 than in CAM5 along with more penetration of precipitation towards the north. In CAM5, the maximum contour of precipitation is somewhat reduced and is comparable to observations. The annual cycle of precipitation averaged over the latitude and longitude of the SAM region is simulated quite well in models, with a well-defined seasonal cycle as shown in Figure 2.4d. Several characteristics of the annual cycle of SAM precipitation, such as the rapid onset between May and June, the

sustained high precipitation from June to August and the slow withdrawal during September to October, are well simulated by both models. As noted earlier in the discussion of spatial patterns, both models produce realistic seasonal variation of precipitation in the SAM region, but with considerable overestimation. The annual cycle highlights this overestimation more clearly by showing excessive precipitation in the months July, August and September as well as in December, January and February.

From the above discussion of mean climatology simulations, it is seen that CAM5 has significantly improved simulations compared to CAM4. We further investigate this improvement by performing different sets of CAM5 simulations using the same radiation (CAMRT), aerosol (BAM) and boundary layer (HB, Holtslag-Boville, 1993) schemes which are used in the CAM4 default configuration. This switching of new schemes (in CAM5) with old ones (in CAM4) allowed us to explore the effect of each individual scheme in improving CAM5 simulations over the SAM. We named each individual experiment of CAM5 as CAM5_BAM, CAM5_BAM_CAMRT, CAM5_BAM_HB and CAM5_BAM_CAMRT_HB (see Table 2.1 for details). Figure 2.5 represents the summer precipitation difference of CAM5_BAM, CAM5_BAM_CAMRT, CAM5_BAM_HB and CAM5_BAM_CAMRT_HB from observation. Comparing these differences, with the default CAM4 and CAM5 runs (Figure 2.2a and 2.2b), reveals that the implementation of new boundary layer schemes (UW moist turbulence) in CAM5 has the greatest effect (in our case) on decreasing the overestimation seen in the CAM4 simulation. As reported by Park and Bretheron, (2009), the new UW moist turbulence scheme improved the cloud top boundary layers in the CAM model. They used the CAM3.5 version to test this scheme and found significant reduction in model bias. In our case, although the new RRTMG radiation scheme and the full

representation of aerosol indirect effects do not contribute as much to the improved SAM simulation, virtually every atmospheric process (revised/replaced) and its physical representation in the new version makes an improvement in the simulation (the individual discussion of all these new features of CAM5 is beyond the scope of this study).

2.3.2 Monsoon Interannual Variability

In this section, the monsoon variability is examined by focusing on the simulation of monsoon indices (precipitation and circulation) for both CAM4 and CAM5 models. The strong and weak monsoon composite analysis is also discussed to further explore the simulation's interannual variability. It has been well recognized that the interannual variability of many climatological variables on earth can stem from ENSO, which is the strongest interannual variability of the earth's climate system. Thus, the link between simulated SAM precipitation and ENSO is also explored using lag correlation. This is also performed to explore the relationship between the Indian Ocean Dipole (IOD, Saji et. al, 1999) and SAM precipitation.

2.3.2.1 Asian Monsoon Indices

We examine the models simulations of monsoon interannual variability with several commonly used monsoon indices, including Indian Summer Rainfall (ISR), the Webster–Yang monsoon index (WY index) (Webster and Yang 1992), the Southeast Asian Monsoon (SEAM) index or Western North Pacific Monsoon (WNPM) index (Wang and Fan 1999), Indian Monsoon (IM) index (Wang et al. 2001) and South Asian Monsoon Index (SAM_i, here the subscript *i* denotes “index” to differentiate it from SAM) (Gowani et al. 1999). The definitions of these indices are given in Table 2.2.

Figures 2.6 and 2.7 show the simulated and observed interannual variability of ISR, WY, IMI, WNPM, and SAMi monsoon indices normalized with their respective standard deviation. All these indices are circulation indices except ISR which represents SAM precipitation. To analyze model simulations for individual strong and weak monsoons, the ISR index is separated from the circulation indices (Figure 2.7) and is presented in Figure 2.6. In Figure 2.6a, the observed ISR index representing the strength (strong and weak monsoon) and interannual variation of SAM precipitation, is shown. Strong monsoon years such as 1980, 1988 and 2007 are differentiable in the observations, whereas in CAM4 and CAM5 (Figure 2.6b and 2.6c) only the year 1988 has the same sign. Both 1980 and 2007 are characterized as weak monsoon years in both models, opposite to the observations. Similarly, the observed weak monsoon years 1984, 1986 and 2002 are simulated as strong monsoon years in model. This means that both CAM4 and CAM5 failed to capture the interannual variability of the SAM, except in some years. We find that there are large errors in the simulation of some extreme seasons which lead to the overall poor skill. Considering SAM extreme precipitation, for those associated with ENSO, both models simulate at least the sign of SAM accurately. For example, the La Niña of year 1988 is successfully simulated by both models while CAM4 failed to spatially capture the El Niño year of 1987. This analysis suggests that the low skill in simulation of monsoon interannual variation arises mainly from a poor simulation ENSO-Monsoon teleconnections rather than the lack of air-sea interaction (coupling). Since the SAM has remote and local SST teleconnections, the poor simulation of SAM interannual variability in these atmospheric models (forced with observed SST) can be explained by analyzing the ENSO-Monsoon teleconnection and regression of Niño SST on SAM precipitation. We will further discuss this issue in the next section.

In case of circulation indices (Figure 2.7), it is seen that both CAM4 and CAM5 show considerable skill in simulating the interannual variation of the WY and WNPM indices with significant correlation coefficients (see Table 2.2). For the IM and SAMi indices, correlation coefficients are insignificant, meaning that these indices are not well simulated in these models. As the WNPM index represents the East Asian summer monsoon, the significantly higher correlation of this index means that East Asian monsoon circulations are better simulated in both models compared to the SAM. Analyses of monsoon spatial patterns also support this result. This may be due to the fact that the East Asian monsoon has a stronger response to ENSO than the Indian monsoon.

To get better insight into the simulated circulation in CAM4 and CAM5 simulations, summer mean velocity potential and divergent wind anomalies are calculated for both models and observations (NCEP). These show upper-level convergence and lower-level divergence over the equatorial central Pacific, and upper-level divergence and lower-level convergence over the SAM region (not shown here). In Figure 2.8, we analyze the difference between model and observation (NCEP) of the summer mean velocity potential and corresponding divergent winds at 850 mb and 200 mb. Although some of the circulation indices have higher correlation for CAM4 than CAM5, the overall spatial patterns from the CAM5 simulations are better. At both atmospheric levels, over the Pacific and Indian regions, CAM5 have much better skill (less difference) compared to CAM4.

2.3.2.2 Composite Analysis

Modeling extreme events is one of the most challenging issues and validating model extreme event simulations is therefore important to assess their performance. In this subsection, we

focus on several particular years which were recorded as strong and weak monsoon years over the SAM region (as seen in Figure 2.6). Strong and weak monsoon years are characterized on the basis of significant weak or strong summer precipitation over the monsoon region. Years with anomalies of summer mean precipitation greater than 0.5 standard deviation above the mean are categorized as strong monsoon years (1980, 1981, 1983, 1988, 1994, 1996, 1998 and 2007) and those with mean precipitation less than -0.5 standard deviation below the mean are categorized as weak monsoons (1982, 1984, 1986, 1987, 1989 and 2002). Composites of weak and strong monsoon years from observations (CMAP), CAM4 and CAM5 are shown in Figure 2.9. The observed weak and strong monsoon composites have a large-scale structure with anomalies of the same sign over many parts within the SAM region. The observed weak (Figure 2.9a) monsoon composite has negative anomalies over the whole Indian region whereas in the strong monsoon (Figure 2.9b) composite there are positive anomalies over the Indian land area, Bay of Bengal, and the maritime continent. The models composites (Figures 2.9c, 2.9d, 2.9e and 2.9f) show that the simulations failed to reproduce the observed anomaly patterns with some areas having significant differences. For its weak monsoon composite, CAM4 and CAM5 have a much different pattern with more intense and large scale positive anomalies (which is opposite from the observed composite patterns) over the Western Ghats and Bay of Bengal. CAM4 and CAM5 to some extent, reproduce the strong monsoon composite over southern India. In short, both models show poor skill in differentiating the strong and weak monsoon years. This is also seen in the models ISR index (Figure 2.6) as both showed poor skill in simulating the interannual variability of the SAM region. This is probably due to the simulated overestimation of precipitation, as well as strong internal dynamics (noise) in the models. An examination of the interannual variability of CAM4 and CAM5 monsoon simulations show

that, although the observed SST tends to enhance the variability, the internal dynamics also produce considerable interannual variability in these simulations. It is interesting to note that the large variance in control runs is dominated by a few events such as 1983, 1988 and 2007. For many years, the interannual variability produced by internal dynamics is often larger than that in the control runs, suggesting that the interannual variability generated purely by internal dynamics is comparable to that forced by the slowly varying SST boundary forcing in many cases. This is probably the reason why these models perform poorly in differentiating strong and weak monsoon seasons.

2.3.3 Teleconnection of SAM with ENSO and IOD in CAM Simulations

In this section, we explore how well CAM4 and CAM5 capture SAM-ENSO and SAM-IOD relationships. We perform regression analysis to analyze spatial patterns of these relationships whereas lag-lead correlation is used for temporal analysis. Figure 2.10 shows the linear regression of Niño3.4 (-5°S – 5°N , 120° – 170°W) and IOD ($(-10^{\circ}\text{S}$ – 10°N , 50° – $70^{\circ}\text{E})$ - $(-10^{\circ}\text{S}$ – 0° , 90° – $110^{\circ}\text{E})$) SST indices with JJAS precipitation and 850 mb winds for observations and both models. Unless stated otherwise, all regression maps show the covariance of the normalized Niño3.4 and IOD indices. The regression of precipitation and 850 mb winds onto the Niño3.4 index is an important key to understand the behavior of CAM4 and CAM5 in simulating realistic ENSO properties as these fields are direct indicators of the connection between the ocean and the atmosphere. In Figure 2.10a, the regression of the observed Niño3.4 index with precipitation and 850 mb winds is shown. The observations reveal enhanced precipitation over the Bay of Bengal, accompanied by a westerly winds anomaly and decreased precipitation over most of the Indian region. In the models' results, (Figure 2.10c and 2.10e) quite realistic patterns are seen over the equatorial

Indian Ocean whereas over the Western Ghats and central India, both CAM4 and CAM5 have opposite response compared to observations. In the IOD regression pattern, (Figure 2.10d and 2.10f), spatial modes are well reproduced over the Indian Ocean (enhanced precipitation over the western equatorial Indian Ocean and decreased precipitation over the Eastern Indian Ocean) whereas over the Indian subcontinent the models have the opposite sign similar to the ENSO regression.

The analysis above show that precipitation response to local and remote SST in the models' simulations is not preserved. To further investigate this issue, the lagged correlation of Niño3.4 and IOD indices with the simulated ISR index is shown in Figure 2.11. The area averaged (0° – 40° N, 55° – 100° E) time series of observed CMAP precipitation (ISR, solid black line), observed All-India Precipitation index (AIR, dashed black line) and simulated (CAM4, solid blue line and CAM5, solid red line) time series are correlated with observed Niño3.4 and IOD SST indices. The months with negative (positive) sign indicate that SST leads (lags) the ISR with maximum lead of 12 months (1 year). Months 0 and 12 indicate June whereas months 4 and 8 correspond to February and October (minus sign for previous months). Correlations are calculated using a 5-month sliding window. The observed positive correlations occur when the SST leads the SAM precipitation and negative correlations occur when SST lags the SAM precipitation. A negative correlation is seen for SST from the same summer to the following winter, showing a weak (strong) SAM in El Niño (La Niña) developing years. The highest negative correlations occurs when the monsoon leads Niño 3.4 SSTs which suggests, as reported in Kirtman and Shukla 2000, that monsoons can provide favorable conditions for triggering or enhancing El Niño or La Niña events in the Pacific during the following winter. The observed ISR index has significant lagged and lead

correlations with SST, with the highest value of around 0.5 when monsoon precipitation is slightly led by SST. This suggests a cross-interaction between monsoon and ENSO, namely, ENSO impacts on SAM precipitation and meanwhile the monsoon variability may affect the ENSO evolution, intensity, and periodicity. The mutual influence between ENSO and SAM has been widely reported in other studies as well (Chung and Nigam 1999; Kitoh et al. 1999; Meehl and Arblaster 1998; Wang et al. 2004). It is noted that the difference in correlation magnitude between Figure 2.11a and those in other studies (Kirtman and Shukla 2000; Yasunari 1990) may be accounted for a dramatic change of the ENSO-SAM relationship in the late 1970s, since Figure 2.11a is obtained only using the data after 1979. In the CAM4 and CAM5 simulations, this relationship is poorly captured, particularly when SST lags monsoon. CAM4 shows a somewhat comparable result when SST leads monsoon. Both of these models failed to maintain the monsoon and ENSO relationship because, as discussed in the composite analysis, the internal dynamics of these models can overwhelm the Pacific SST influence on monsoon precipitation. In Figure 2.11b, the lag-lead correlation of SAM with IOD is computed. A positive correlation during late spring and the simultaneous summer is seen. The correlation changes to negative in the following fall, suggesting a negative feedback of SAM on the IO. For the models, the simultaneous response is not clear but when IOD leads monsoon, both models show a comparable response to the observations.

Overall the above analysis shows that the interannual skill of CAM4 and CAM5 in simulating SAM is poor. Both models failed to differentiate strong and weak monsoon which is indirectly linked to their poor reproduction of the ENSO-monsoon relationship. The correct representation of the ENSO-SAM relationship in models is crucial, since it is the basis for seasonal forecasts of SAM using climate models. The poor skill of CAM4/CAM5 interannual

variability, even when forced by observed SST, is attributed to the models' poor skill in simulating the SST-precipitation relationship over the Indian and Pacific oceans and a lack of atmosphere-ocean coupling that has been reported as critical for skillful simulation of the monsoon (Wang et. al. 2005). Since this lack of atmosphere-ocean coupling in GCMs is one of the possibilities for their poor skill, we focus our analysis on the coupled CCSM4 model in the next section and compare its simulation with CAM4 and observations.

2.4 Coupled Simulation using CCSM4

We investigate the mean climatology and relationship between SAM precipitation and SST in the CCSM4 coupled model, which will allow insight into the role of coupling on the simulation of SAM precipitation. As previously discussed, CCSM4 uses CAM4 as its atmospheric model and POP2.2 as its ocean model. Along with observations, we will also contrast CCSM4 with the CAM4 results presented in previous sections. Here we will mainly use the CCSM4 climatology run whereas for some sensitivity experiments, data from a CCSM4 transient run (CCSM4_TR, downloaded from NCAR) forced with observed forcing of greenhouse gases) is also used.

2.4.1 Mean Climatology of CCSM4

We first analyze, as for the atmospheric simulations, the coupled model over the tropical region including both Indian and Pacific Oceans. Figure 2.12b shows the JJAS mean precipitation difference (in mm/day) between CCSM4 and CMAP observation. The difference between the CAM4 climatology run (CAM4_CLIM) and observations is also shown in Figure 2.12a. CCSM4 shows significant differences, particularly over the Indian and Pacific Ocean. Specifically, the coupled simulation underestimates precipitation over the

western and eastern equatorial Pacific and over the eastern Indian Ocean, and it overestimates precipitation over the western Indian Ocean and central equatorial Pacific Ocean. These differences, shown in Figure 2.12, result from the ocean component of CCSM4. The SST bias from the ocean model influences the precipitation directly, making it different from the observed precipitation climatology. Comparing CCSM4 with CAM4_CLIM shows that CCSM4 precipitation biases are at a broad scale (especially over oceans). In CCSM4, the negative precipitation bias increases over the equatorial area in the Pacific Ocean. This is probably due to the feedbacks of air-sea coupling in the coupled model that amplifies the bias in the atmospheric and oceanic components. Same as reported in Gent et al., (2011), CCSM4 has the double ITCZ bias, characterized by heavy simulated precipitation over most of tropical Pacific and the equatorial Indian Ocean, and light precipitation in the west and central Pacific between 15° and 30° south. The double ITCZ problem was also present in previous versions of the CCSM model. Lin (2007) found that most of the current coupled models and uncoupled models have this double ITCZ problem to some extent. Focusing on the SAM region reveals that while the CAM4 simulation overestimates precipitation over much of this region, the coupled simulation is more realistic and comparable to observations although the amounts are still overestimated somewhat. This is similar to results from the CCSM3 model reported in Meehl et al, 2006. The CCSM4 simulation has reduced bias over the Arabian Peninsula and the western coast of India (Figure 2.12b), which is a direct consequence of the thermodynamic air-sea interactions in the Arabian Sea, Bay of Bengal, and South China Sea, which are absent in uncoupled simulations. Meehl et al. 2012 also reported that the CCSM4 simulation over the SAM region is much better than the CAM4 simulation. It is also reported in Wang et al. (2004) that the implementation of air-sea coupling could improve the model simulation of monsoon

precipitation and circulation in the Asian monsoon. The absence of air-sea coupling in CAM4 results in continuous heating of the atmosphere by the prescribed SST (warm SST) which increases the evaporation, resulting in increased precipitation in its simulations. This amplifies the SAM variability and therefore CAM4 simulations overestimate precipitation in the SAM region. We will further discuss air-sea coupling and role of SST bias in the next section. In general, CCSM4 shows a large reduction in precipitation and less bias over the SAM region particularly over Arabian Sea and west equatorial Indian Ocean as compared with the CAM4 simulation. The reduction of SAM precipitation in the coupled model can also be seen in the seasonal cycle (not shown) averaged over the region.

Seasonal mean summer precipitation and 850 mb winds pattern from CCSM4 simulation, shown in Figure 2.13, is more realistic and comparable to the observations as compared to CAM4 and CAM5 simulation (Figure 2.3). The extreme high precipitation area over the northern West Indian Ocean is diminished in the coupled simulation making it more comparable to observations. However, CCSM4 also removed the heavy observed precipitation over the Bay of Bengal making its simulation different than observation. This is a significant shortcoming of the coupled simulation. Also, in CCSM4 runs, the precipitation is more concentrated in the western Indian Ocean, which was also seen in CCSM3 (Meehl et al, 2006). Considering these spatial patterns only, the overall mean climatology of CCSM4 seems to be more realistic and much better than from the uncoupled simulation, providing evidence that coupled air-sea interaction is necessary for climate models.

2.4.2 Teleconnection of SAM with ENSO in Coupled Simulation

A correct ENSO-monsoon relationship is one of the prerequisites needed for a coupled model to produce reliable simulations of the monsoon. Here we document the ability of CCSM4 to reproduce the observed lag-lead relationships between the SAM and ENSO, and to understand how systematic errors may affect the simulation of this relationship. We first discuss the simulation of Niño3.4 and IOD indices in the coupled model. Figure 2.14 shows the variance spectrums of monthly Niño3.4 and IOD index for (a) observation and (b) CCSM4. In the observations, the broad peak shows a probable frequency of ENSO events of 3 to 6 years (0.24/year) with the maximum variance of about 20. In the CCSM4 simulation, the same frequency of 3 to 6 years is seen with maximum peak at 4 years although the CCSM4 Niño3.4 variability is significantly larger than the observed variability. In the previous version of CCSM i.e. CCSM3, the ENSO frequency (about 2 years) was reported as very poor by Collins et al. (2006). This shows that the new version of CCSM has significant improvements in its dynamics and can therefore simulate the ENSO properties more closely to observation. For the case of the IOD spectrum, being irregular in its oscillatory period, there is no well-defined peak in the observed frequency whereas in CCSM4, the peak of the IOD spectrum remains in phase with that of the Niño3.4 index showing a frequency of 3 to 6 years. Also these results show that the IOD index varies significantly with ENSO in CCSM4. The observed IOD variance is very small whereas the model variability is significantly larger showing a similar pattern as the Niño3.4 index.

Figure 2.15 (top) shows the linear regression of the CCSM4 simulated JJAS Niño3.4 (-5°S – 5°N , 120° – 170°W) SST index with JJAS precipitation and 850 mb winds. Comparison of this regression pattern with Figure 2.10 reveals the improved spatial Niño3.4 regression

pattern of the CCSM4 simulation, which is due to the improved and coherent atmospheric response in coupling. This can be also seen in Figure 2.15 (bottom), representing lag-lead correlation of CCSM4 simulated SAM precipitation with simulated Niño3.4 SST index. The observations show positive correlation when precipitation lags ENSO and strong negative correlations when precipitation leads ENSO. The CCSM4 can partially capture the observed variation of correlation timing but with quite different magnitudes. Comparing CCSM4 lag-lead correlation with CAM4 (Figure 2.11) shows significant improvement in the coupled simulation relationship. This is probably due to an improved or consistent SST simulation and its interaction with atmosphere, which is absent in atmosphere-only simulations. The response of ENSO to SAM precipitation (i.e. SST lagging the monsoon) is realistic in CCSM4, better than in CAM4. The lag-lead correlation for ENSO suggests that in the CCSM4, SST has significant biases over the central equatorial Pacific and Indian Ocean. The fact that CCSM4 reveals a better connection between ocean and atmosphere in its simulation, although the Niño3.4 amplitude is considerably larger than the observed one, supports the low sensitivity to SST in the CAM4 model. Apparently, the atmospheric component (i.e. CAM4 in CCSM4) shows a realistic response to ENSO variability only when being forced by a strong SST signal which is confirmed by CAM4 sensitivity experiments (not shown or discussed further here).

Since SST and precipitation are strongly coupled in the tropics, an unrealistic simulation of SST distribution should lead to an unrealistic SAM-ENSO relationship. To assess this we analyzed the average mean seasonal SST differences between CCSM4 and the observed climatology over the Indian and Pacific oceans. This also helps further investigate the SAM improvements in coupled simulations. In the observed mean SST climatology (not shown

here) the most important feature is the warm pool region over the west Pacific with SSTs more than 28°C and a cold SST tongue along the east Pacific associated with easterly trade winds along with a strong east-west SST gradient across the equatorial Pacific. A north-south irregularity is present in the eastern Pacific where warm water is located north of the equator and cold water is present along the west coast of South America. This north-south irregularity is important for the formation of the annual cycle (Xie 1994) and ENSO (Cane and Zebiak 1986). CCSM4 SST patterns, showed almost the same climatology but with significant differences in magnitude. Figure 2.16 shows the difference between the simulated CCSM4 SST climatology and the observed SST climatology for DJF, MAM, JJA and SON seasons. In CCSM4, the model simulates warm SSTs over most of the Pacific and Indian Oceans in all four seasons whereas over the eastern equatorial Pacific and northern East Indian Ocean, the model has cold SST biases in spring and summer. The cold SST bias in the equatorial Pacific significantly reduces the temperature of the warm pool whereas the warm biases near the coast of Peru reduce the meridional SST gradient. This may be the cause of the double ITCZ in the CCSM4 simulations, as seen in Figure 2.12b. Comparing the SST bias in summer with the summer precipitation bias of CCSM4 (Figure 2.12) reveals that the negative precipitation anomalies over much of the Pacific Ocean are largely associated with the cold SST bias in the same region. This most likely originates from errors in the atmospheric model. As reported in Li and Hogen 1999, and Manganello and Huang 2008, deficiencies in the simulated SSTs are likely responsible for some of the unrealistic ENSO properties in the coupled model. Although CCSM4 simulated summer monsoon precipitation in South Asia is considerably improved, the SST bias over the Pacific Ocean (ENSO region) can still lead to a spurious response of the SAM to ENSO in CCSM4.

2.5 The Contribution of Air-Sea Interaction to SAM Simulation

In previous sections, we investigated the SAM simulations using CAM4 and CCSM4. Their differences were due to two factors: 1) the role of coupling in CCSM4 which is absent in CAM4; 2) the SST consistency in CCSM4. To better isolate the role of coupling in simulating the SAM, we designed another set of experiments referred as to CAM4_POP, in which the predicted SST by CCSM4 forces CAM4. These experiments allow us to investigate the air sea coupling in CCSM4 and its effect on SAM precipitation. An ensemble strategy is used as discussed in section 2.2, and therefore the following discussions are from the ensemble mean analysis.

The difference between the CAM4_POP and CCSM4 (Figure 2.17b) reveals that the precipitation and westerly winds in the CAM4_POP simulation are enhanced over the northern Indian Ocean including the Arabian Sea and Bay of Bengal. These differences show that SAM monsoon precipitation is amplified in the absence of the air-sea coupling. A considerable increase is also seen in the variance (not shown here), revealing that the monsoon variability is amplified by about half as compared with the CCSM4. The absence of the air-sea coupling keeps SSTs warm in the Indian Ocean (as discussed previously), which increases the local evaporation and precipitation. This suggests that the air-sea coupling works to stabilize the monsoon and hence suppress the variability, which is the case in CCSM4 simulations. Figure 2.17a shows the difference between observations (CMAP/NCEP) and CAM4_POP mean precipitation and winds. The spatial pattern in this case is almost same as seen in Figure 2.12b for the SAM region. This means that the reduction in excessive precipitation seen in the CCSM4 simulation is not only due to the air-sea interaction but also due to the more consistent SST simulation in the coupled model

integration. In other words, the more consistent SST simulated in CCSM4 (different from observation in magnitude) is responsible for decreasing the overestimation of precipitation.

To further elaborate this point we performed another set of experiments and analyzed the CCSM4 SST in the Indian Ocean and its effect on SAM monsoon. For this set of experiments, we used the SST data from the CCSM4 transient run (CCSM_TR). The CCSM4_TR precipitation is similar to precipitation in the CCSM4 run, but the SST bias is more significant in CCSM4_TR simulation.

The Indian Ocean SST bias, seen in Figure 2.16, prompted us to find its influence on the SAM. Comparison of CCSM4 and CAM4 runs suggests that the coupled model cold SST biases significantly reduce monsoon precipitation as seen in Figure 2.17. The role of these biases is for CCSM4 to remove the overestimation (reduction in the monsoon) seen in the CAM4 simulation. Gimeno et al. (2010) have shown the northern Indian Ocean to be an important moisture source for Indian monsoon precipitation and therefore understanding the monsoon dependence on Indian Ocean SST, and correctly representing this in climate models, is important in order to realistically predict monsoon fluctuations.

In Figure 2.18a and 2.18b, the annual cycle of SST over the northern Indian Ocean for two separate regions, the Arabian Sea and Bay of Bengal, is shown for observation and for both the CCSM4 and CCSM4_TR coupled model runs. In CCSM4, the magnitude of the cold SST bias in the Arabian Sea is small, diminishing after the summer season, whereas CCSM4_TR shows a large cold bias throughout the year, with a slight decrease in its magnitude during the fall. Over the Bay of Bengal, instead of a cold SST bias, both models show a warm SST bias, with a larger bias in the CCSM4 climatology run. This means, from January to July, the cold

bias becomes more confined to the Arabian Sea in these models, while a warming appears in the Bay of Bengal.

To further analyze the role of this Indian Ocean bias, we designed two different sensitivity experiments with CAM4 using climatological SST repeated every year but with the addition of the CCSM4 northern Indian Ocean SST bias into the SST climatology. In the first experiment, we added the annual cycle of CCSM4_TR SST bias (bounded in the Ocean region 7°-30°N, 40°-100°E) covering the whole northern Indian Ocean to the annual cycle of climatological SST (named as CAM4_AS_BoB). To remove any discontinuity at the boundary of the modified region, the bias is added in a tapered manner over the region, being highest at the center and approaching zero at its boundaries. In the second set of the experiments, the bias of CCSM4_TR SST is confined only to the Arabian Sea covering 7°-30°N, 40°-80°E (named as CAM4_AS). Both of these experiments are compared against the CAM4 climatology run (CAM4_CLIM) forced with the climatological SST cycle (see Table 2.1 for details). To account for uncertainties, each simulation is performed three times starting with three different initial conditions. As mentioned previously, CAM4 is not very sensitive to the small changes in its boundary conditions which means that only a strong anomaly added to its boundary condition will produce a significantly altered simulation. We therefore use the CCSM4_TR simulated SST in this case which has larger magnitude of SST bias, especially in the Arabian Sea. In Figure 2.18c and 2.18d, precipitation differences of both of these experimental setups from the CAM4_CLIM run are shown. In CAM4_AS_BoB, a significant reduction in the precipitation is seen over the whole Indian subcontinent, Arabian Sea and Bay of Bengal. Also the increased precipitation is seen over the West Indian Ocean around 10°N. In the second experiment (CAM4_AS) where we used

the SST bias only over the Arabian Sea, the reduced precipitation over the Bay of Bengal diminished while the Arabian Sea continued to be affected by the bias. Both these experiments support our conclusion that the reduction of CCSM4 SAM precipitation is mainly due to the SST bias in northern Indian Ocean. The weakened (reduced precipitation as compared to CAM4) monsoon seen in the CCSM4 run is therefore mainly caused by systematic cold SST biases of northern Indian Ocean particularly in the Arabian Sea. This cold bias keeps the ocean cool, and thus reduces evaporation, which results into the reduction of SAM precipitation. This issue needs more attention in the coupled model to improve monsoon simulation. CCSM4, while being revised with improved physics and dynamics, needs improvement in its oceanic component.

2.6 Summary and Conclusions

The SAM precipitation is an important climatic feature due to its profound influence on droughts and floods over Asia, along with its influence on the global general circulation. Improved and accurate simulation of the SAM system is therefore crucial to predict decadal and seasonal climate as well as projecting long-term climate change in the region. Also it is necessary to assess whether climate models can realistically simulate monsoon systems before using them for such predictions. This chapter discussed selected features of the SAM precipitation in the simulations of NCAR's versions of the uncoupled (CAM) and coupled (CCSM) climate models. Simulations using CAM4, CAM5 and CCSM4 models are performed and compared against observations to identify improvements and discrepancies in these newly updated models. Along with the simulated mean climatology of the region, the interannual variability and SAM-ENSO/IOD teleconnections are evaluated using lag-lead

correlation and regression analysis. The improvements due to air-sea interactions and impact of SST biases from the CCSM4 are assessed in coupled model simulations.

It is found, in the comparison of atmosphere-only simulations, that the improvements in CAM4 and CAM5 dynamics and convection parameterizations have eliminated many regional differences (especially for CAM5). Many improvements in these simulations, compared to previous versions, are seen in both models. The detailed structure of spatial patterns and the seasonal cycle of monsoon precipitation are well reproduced in both CAM4 and CAM5. The annual cycle of average precipitation is well simulated along with its major characteristics such as the rapid monsoon onset between May and June, the high precipitation during June-August and slow withdrawal during September-October. The large northward shift of the ITCZ from January to July is also well simulated by both CAM4 and CAM5 and its location and strength are fairly well reproduced. Increasing the resolution shows a pronounced improvement in precipitation simulation with a reduction in many regional biases, especially over regions of complex terrain. The CAM5 new dynamics and physics showed improved simulation results over the SAM region. Sensitivity experiments using CAM5 showed that the implementation of new boundary layer schemes (UW moist turbulence) in CAM5 contributes to decreasing the CAM4 simulation overestimation.

Analysis showed that both CAM4 and CAM5 poorly simulate the ENSO-monsoon teleconnection. These models partially captured the monsoon interannual variability with inconsistencies in oscillatory period and amplitude. It is also found that the simulation of East Asian summer monsoon is much better than the simulation of the SAM in both CAM4 and CAM5. The better simulation of the WY and WNPM monsoon indices and poor simulation of the IM, SAMi and ISR monsoon indices in both CAM4 and CAM5 also supported this

conclusion. Both the models are able to simulate the winds circulation such as equatorial monsoon flow and lower level jet stream very well. Both models simulate excessive precipitation over the western Indian Ocean and subtropical Pacific Ocean whereas decreased precipitation is simulated over the eastern Indian Ocean, China Sea and South America. Over the SAM region their simulations show significant large-scale biases such as excessive precipitation over the Arabian Sea and over the Western Ghats of India, and reduced precipitation over the eastern Indian Ocean extending into the Bay of Bengal.

The CCSM4 simulated SAM precipitation is considerably improved compared with CAM4 with the reduction of many biases particularly over the Arabian Peninsula and the western coast of India. The results showed that the air-sea coupling has significantly improved the monsoon simulation. Along with these improvements, interrupted northward progression and delayed onset of the monsoon over the SAM region is seen. The CCSM4 underestimated the precipitation over the equatorial area in the Pacific Ocean. Also CCSM4 still has the double ITCZ problem that was also present in the previous versions of the CCSM model (CCSM3). CCSM4 showed a systematic cold bias in the simulation of SSTs over the tropical Pacific Ocean and hence showed problems in simulating the observed SST-precipitation relationship. Analysis over the whole tropical region revealed that biases in CAM4 and CCSM4 are somewhat similar to those in previous versions of these models.

The frequency of ENSO in CCSM4 is found to be more realistic than was simulated in its previous version (CCSM3). The SAM-ENSO teleconnection in the CCSM4 climatology run is partially captured. Significant cold biases over the equatorial Pacific Ocean are found in CCSM4, particularly in winter and early summer. It is seen that the air-sea coupling can improve the simulation of precipitation. Forcing CAM4 with coupled model SST clarified the

impact of the air-sea coupling in the interannual variability of the SAM precipitation. The local air-sea coupling over the SAM region acts to modulate the activity of the SAM summer monsoon as well as the remote SST forcing. The SST continuously warms over the SAM region as the feedback from the atmosphere to the ocean does not exist in the CAM4 model forced with SST from the coupled model. The SST warming contributes to increased evaporation, which results in the monsoon destabilization over the SAM region. Another impact, the absence of the air-sea coupling, enhances heavier precipitation in the SAM. It is found that, along with air-sea interaction, SST bias in the CCSM4 model plays an important role in simulation of SAM precipitation variability and magnitude. Using CAM4 sensitivity experiments, the influence of the coupled model SST bias in the northern Indian Ocean on SAM precipitation is investigated. It is found that the reduction of SAM precipitation in the coupled simulation, as compared to the uncoupled simulation, is mainly due to cold SST bias in the Arabian Sea.

The strengths and limitations in simulating Asian summer monsoon in CAM4, CAM5 and CCSM4, depend mainly on how well they simulate the mean state of atmosphere, its variability, the internal dynamics of monsoon systems and ocean-atmosphere interactions. Although these recent model versions have many improvements and are able to capture the observed features of SAM precipitation, many biases are still present. This chapter shows that while the NCAR systems models can serve as tools in simulating and understanding Asian monsoon climate systems, they still have simulation errors that need further consideration. Along with the improvements in the model physics and resolution, understanding of the coupled physical processes in conjunction with the complex topography over the SAM region is crucial. As the ocean dynamics also play an important role in Indian

Ocean SST, further studies are needed to clarify its relative importance compared with the role of air-sea interaction in SST cooling during the SAM. It is necessary for the coupled model to simulate realistic SST variation to improve the SST climatology, which can then improve the SAM precipitation teleconnection in CCSM4. In general, modeling monsoon fluctuations mainly depends on understanding the fundamental processes that affect local climate, good parameterization and representation of these processes and the methods used for numerical implementation of these processes.

Table 2.1: List of experiments used in CAM4, CAM5 and CCSM4 validation.

Experiment Name	Model Used	Time Period	Description / Boundary Conditions (BC)	Ensemble size
CAM4	CAM4	1978-2008	1.9° x2.5° horizontal resolution and 26 vertical levels. Prescribed observed SST data as BC	10
CAM5	CAM5	1978-2008	1.9°x2.5° horizontal resolution and 30 vertical levels. Prescribed observed SST data as BC	10
CAM4_CLIM	CAM4	30 years	1.9°x2.5° horizontal resolution and 26 vertical levels. Climatology SST data repeated each year	05
CCSM4	CCSM4	100 years	1.9°x2.5° horizontal resolution and 26 vertical levels for CAM4 and 1°x1° horizontal resolution with 60 vertical levels for POP2.2. Present day climatology forcing	01
CAM5_BAM	CAM5	1978-2008	1.9°x2.5° horizontal resolution and 30 vertical levels with Bulk Aerosol Model (BAM) scheme. Prescribed observed SST data as BC	01
CAM5_BAM_CAMRT	CAM5	1978-2008	1.9°x2.5° horizontal resolution and 30 vertical levels with BAM and CAMRT (radiation) schemes.	01

			Prescribed observed SST data as BC	
CAM5_BAM_HB	CAM5	1978-2008	1.9°x2.5° horizontal resolution and 30 vertical levels with BAM and HB (Holtslag-Boville, boundary layer turbulence) schemes. Prescribed observed SST data as BC	01
CAM5_BAM_CAMRT_HB	CAM5	1978-2008	1.9°x2.5° horizontal resolution and 30 vertical levels with BAM, HB, and CAMRT schemes. Prescribed observed SST data as BC	01
CAM4_POP	CAM4	1971-2000	Same as CAM4 but with predicted SST from CCSM4 climatology run	03
CAM4_AS_BoB	CAM4	1978-2000	Same as CAM4_CLIM but with climatology SST data modified in the AS and BoB region	03
CAM4_AS	CAM4	1978-2000	Same as CAM4_CLIM but with climatology SST data modified in the AS region only	03
CLIM = climatology, BC= Boundary Conditions, AS = Arabian Sea, BoB = Bay of Bengal				

Table 2.2: Details of frequently used Asian monsoon indices. The correlation coefficient of simulated indices with observations is shown in last two columns.

Name of the Index	Type of Index	Definition	Reference	Correlation	
				CAM4	CAM5
Indian Summer Rainfall (ISR)	Precipitation	PREC (5°– 40°N, 60°– 100°E) averaged JJAS precipitation over the domain	-	-0.13	-0.31
Webster–Yang monsoon (WY)	Circulation	U850 - U200 (0°–20°N, 40°– 110°E) vertical shear of zonal winds between 850 mb and 200 mb levels	Webster and Yang 1992	0.38	0.45
Western North Pacific Monsoon (WNPM)	Circulation	U850 (5°–15°N, 90°– 130°E) - U850 (22.5°– 32.5°N, 110°–140°E) difference of 850 mb zonal winds	Wang and Fan 1999	0.66	0.60
Indian Monsoon (IM)	Circulation	U850 (5°–15°N, 40°–80°E) - U850 (20°–30°N, 70°– 90°E) difference of 850 mb zonal winds	Wang et al. 2001	-0.037	-0.11
South Asian Monsoon Index (SAM _i)	Circulation	V850 - V200 (10°–30°N, 70°– 110°E) vertical shear of meridonal winds between 850 mb and 200 mb levels	Goswami et al. 1999	-0.26	-0.13

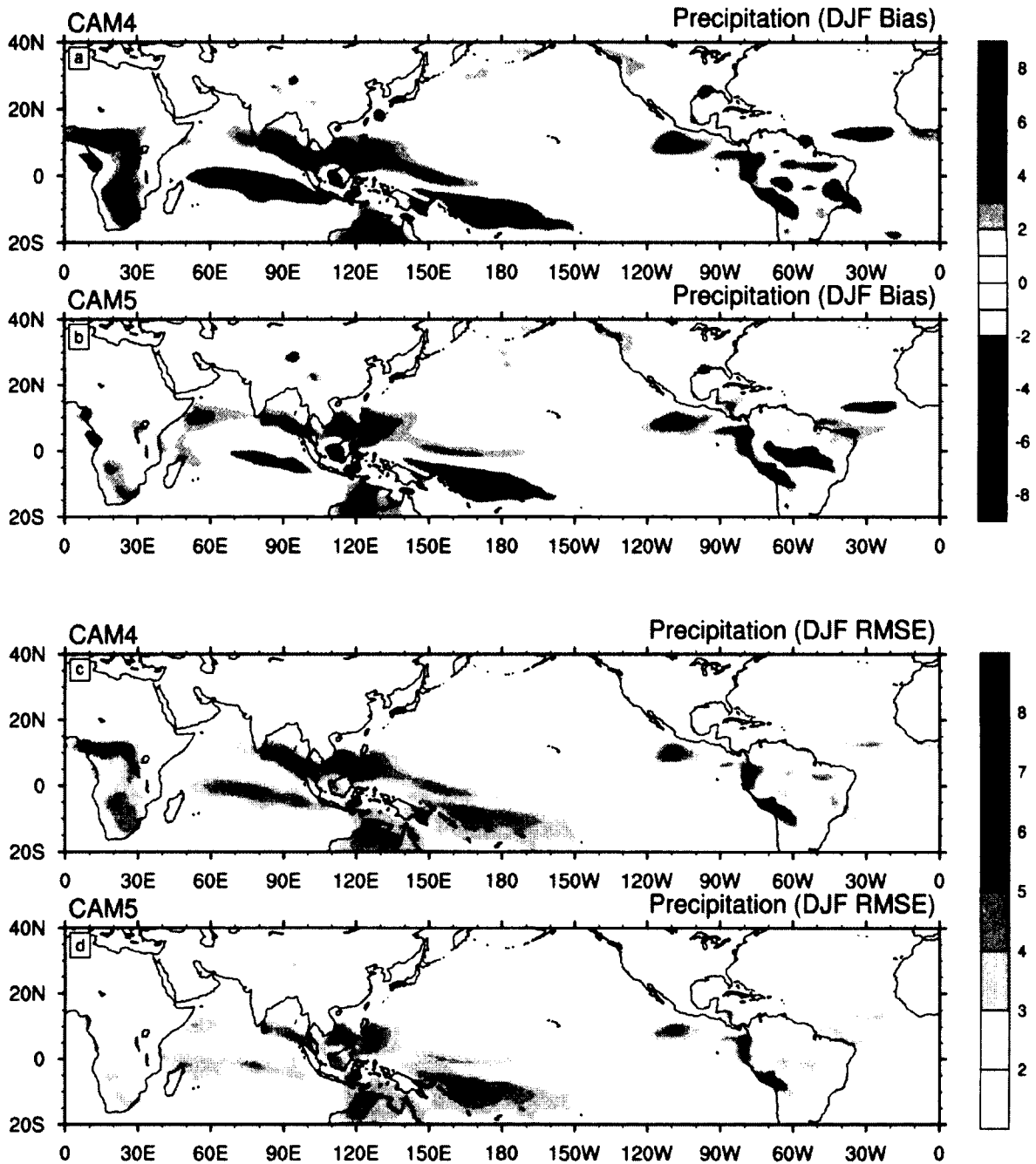


Figure 2.1: Seasonal mean (December–February; DJF) precipitation differences (biases) and root means square error (RMSE) from observation (CMAP) for (a, c) CAM4 and (b, d) CAM5. Units are in mm/day.

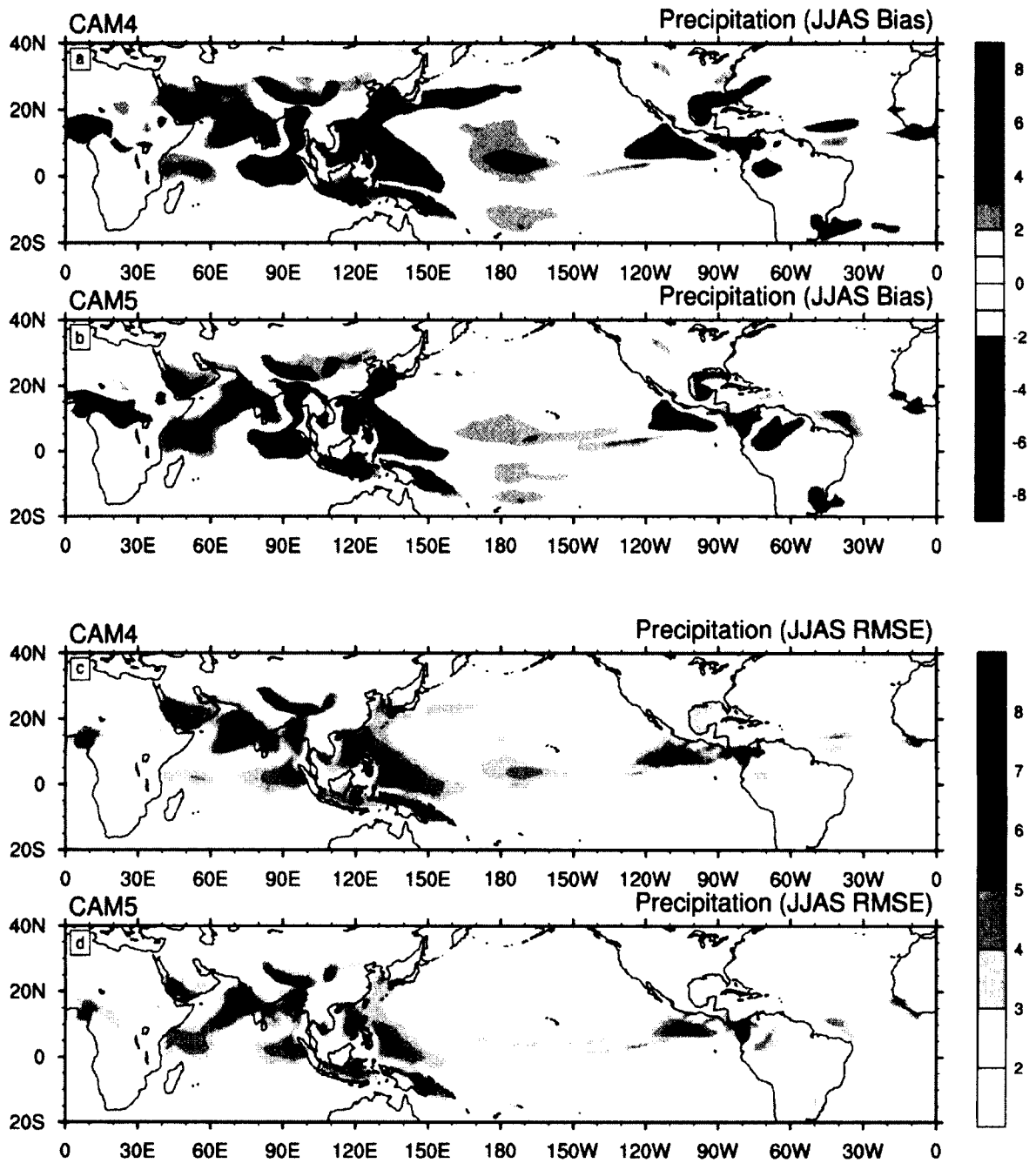


Figure 2.2: Same as Figure 2.1 but for the summer season (June–September; JJAS).

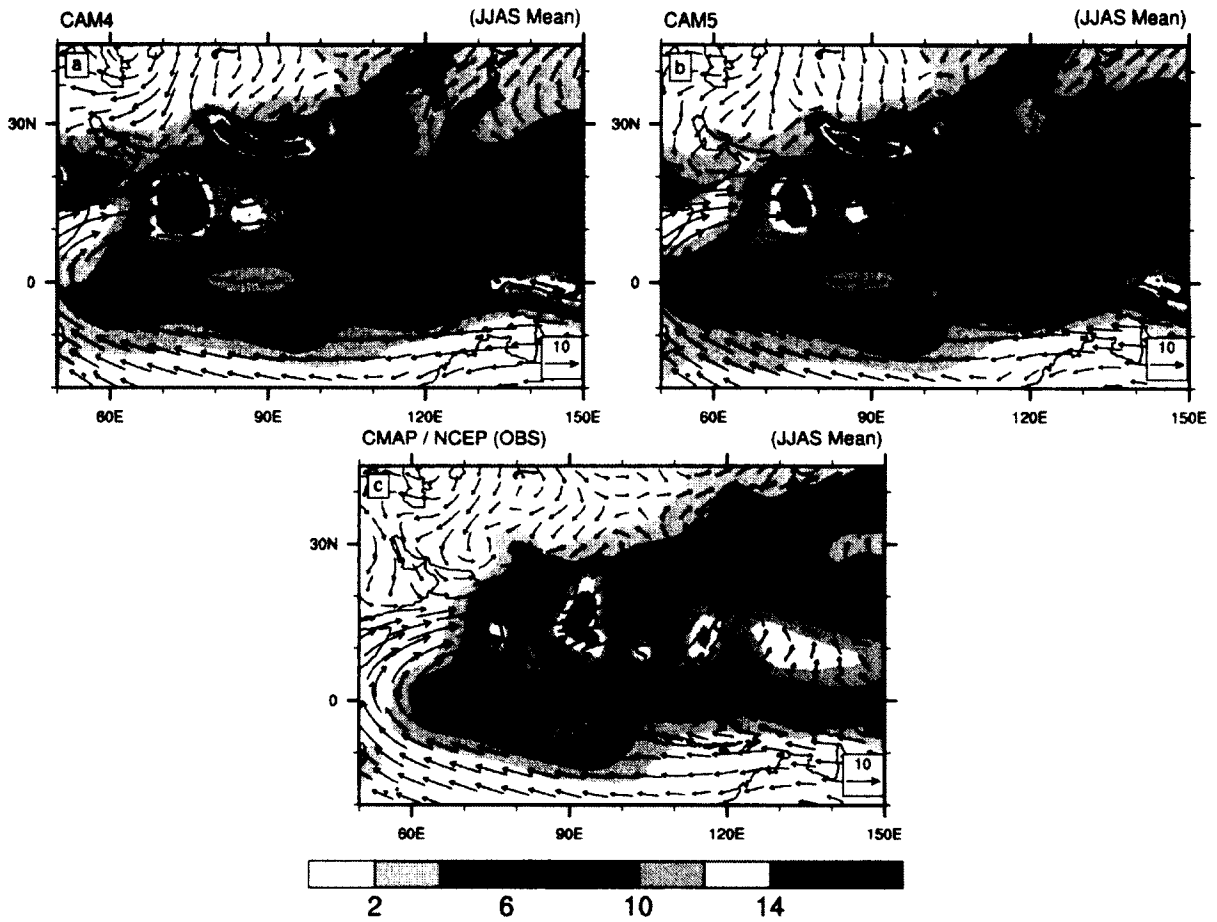


Figure 2.3: Seasonal mean (June–September; JJAS) precipitation and 850 mb winds from: (a) CAM4, (b) CAM5 and (c) observations (CMAP/NCEP). Precipitation (shaded) in mm/day and 850 mb winds (vectors) in m/s.

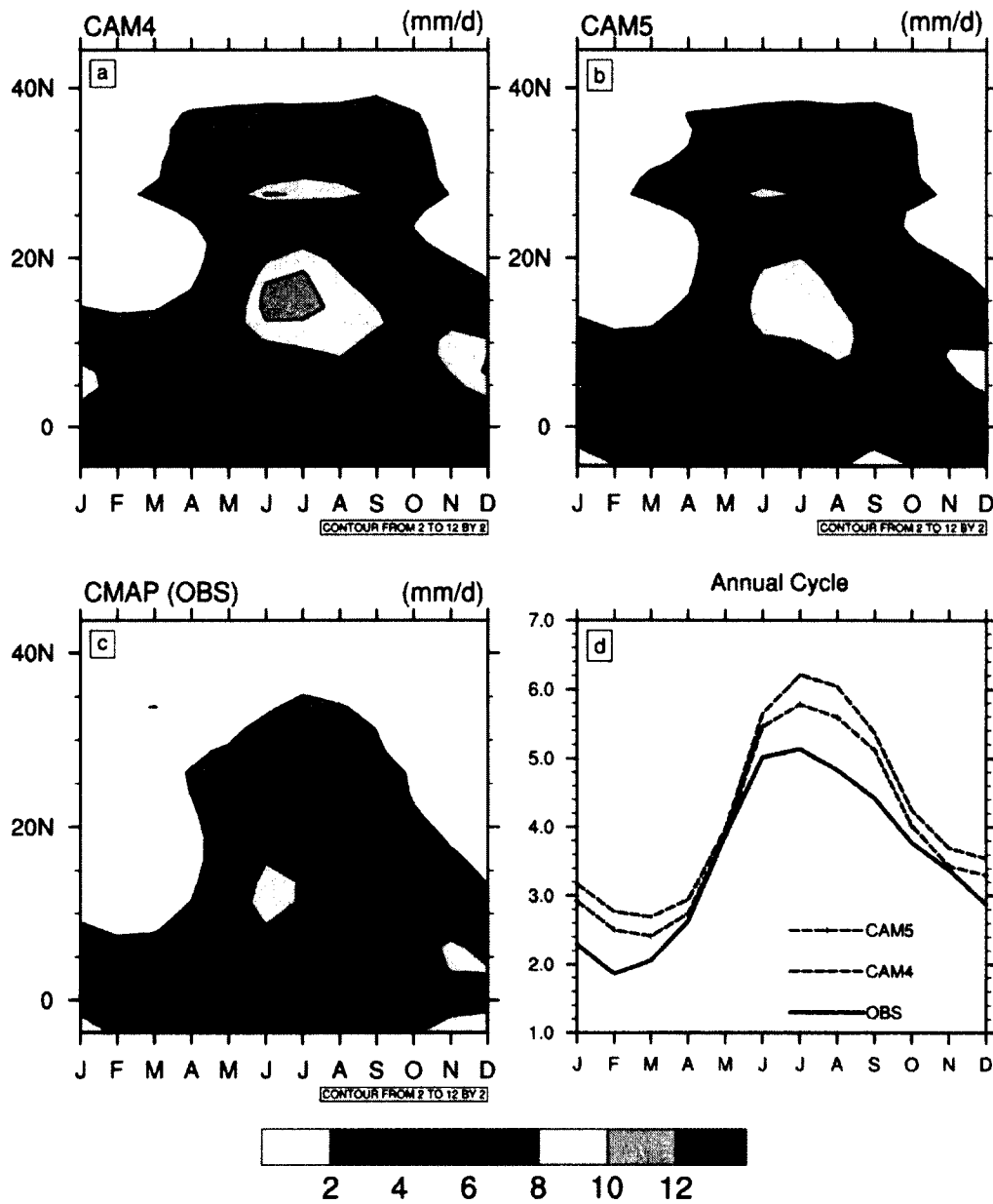


Figure 2.4: Time-latitude evolution of precipitation averaged over (50°–120°E) for: (a) CAM4, (b) CAM5 and (c) observations (CMAP). Precipitation annual cycle area averaged over SAM region is shown in (d). Units are in mm/day.

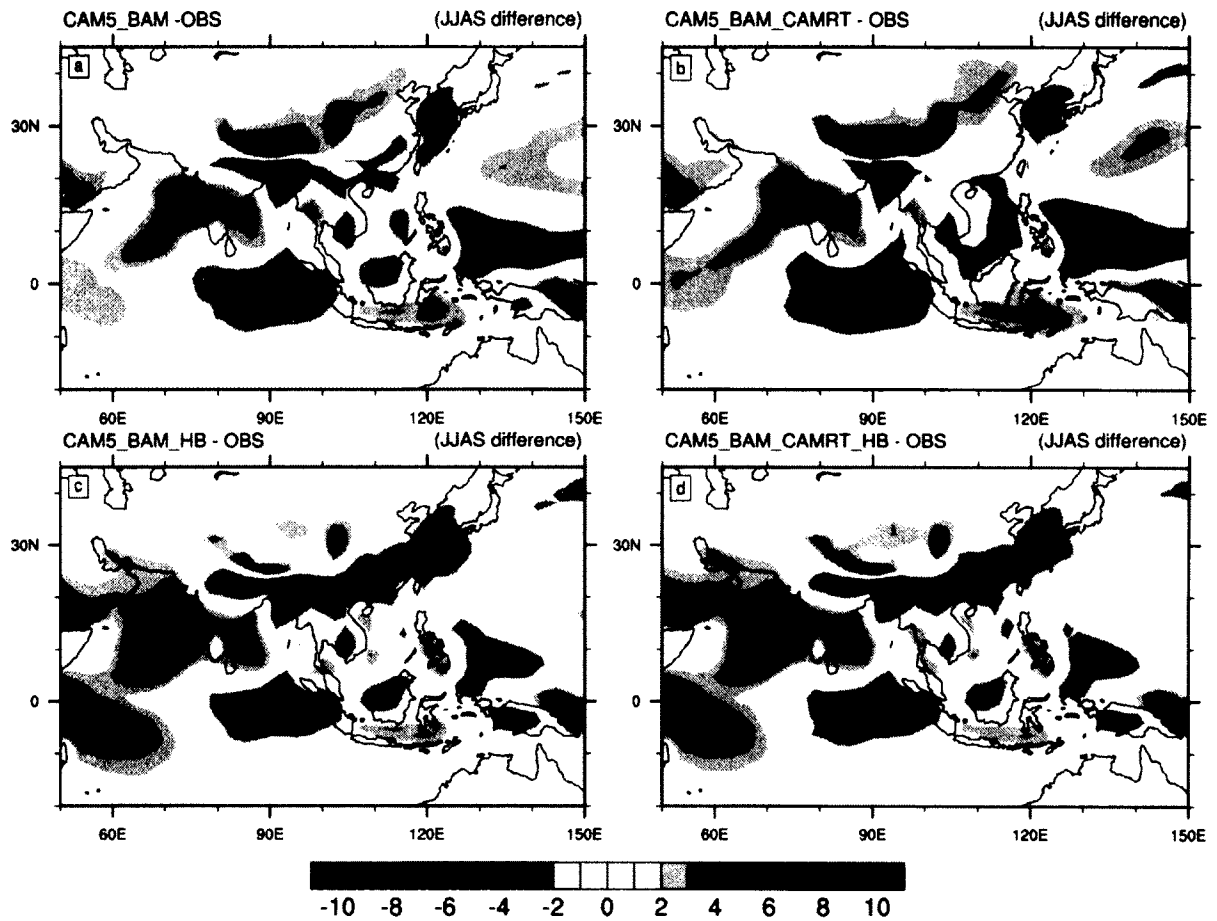


Figure 2.5: Seasonal mean (June–September; JJAS) precipitation differences from observations (CMAP) for: (a) CAM5_BAM (CAM5 with Bulk Aerosol Model (BAM) scheme), (b) CAM5_BAM_CAMRT (CAM5 with BAM and CAMRT (radiation) Schemes), (c) CAM5_BAM_HB (CAM5 with BAM and HB (Holtslag-Boville, boundary layer turbulence) schemes) and (d) CAM5_BAM_CAMRT_HB (CAM5 with BAM, HB and CAMRT schemes). Units are in mm/day.

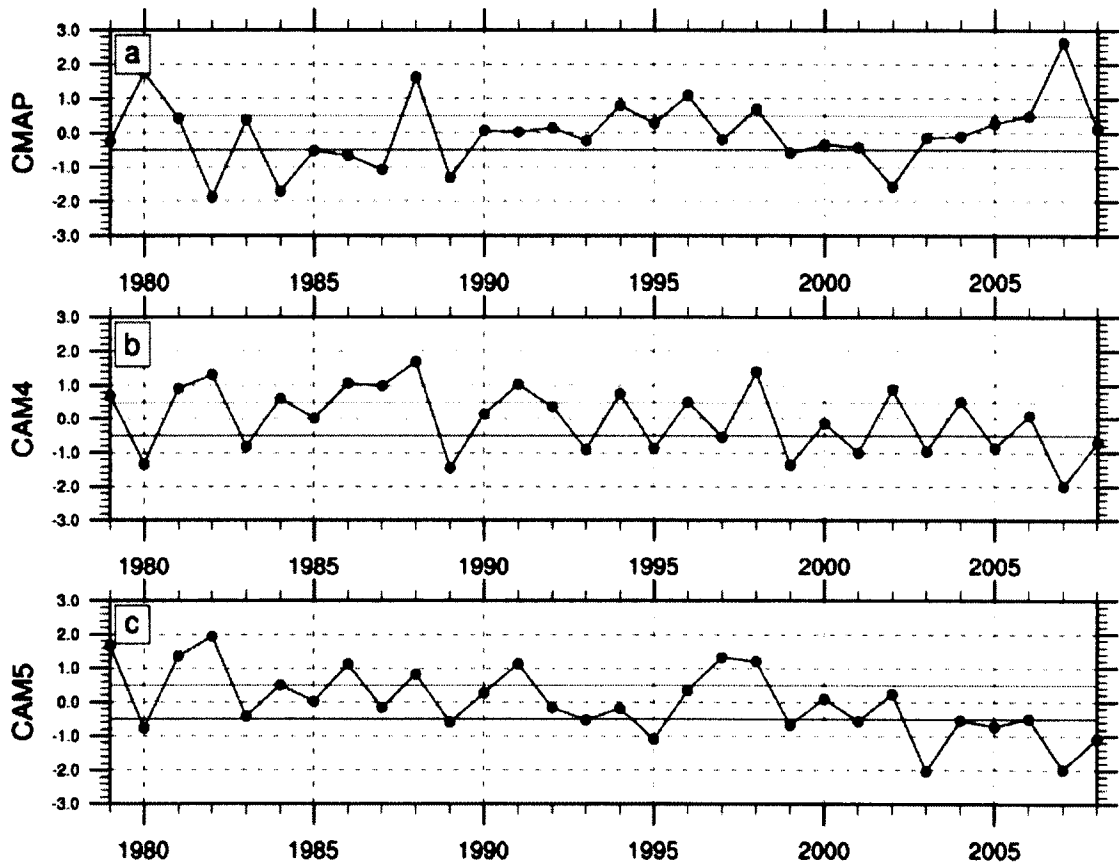


Figure 2.6: Time series of Indian summer rainfall (ISR) index for (a) CMAP, (b) CAM4 and (c) CAM5. Details of this index are given in Table 2.1. The time series are normalized and thus unitless.

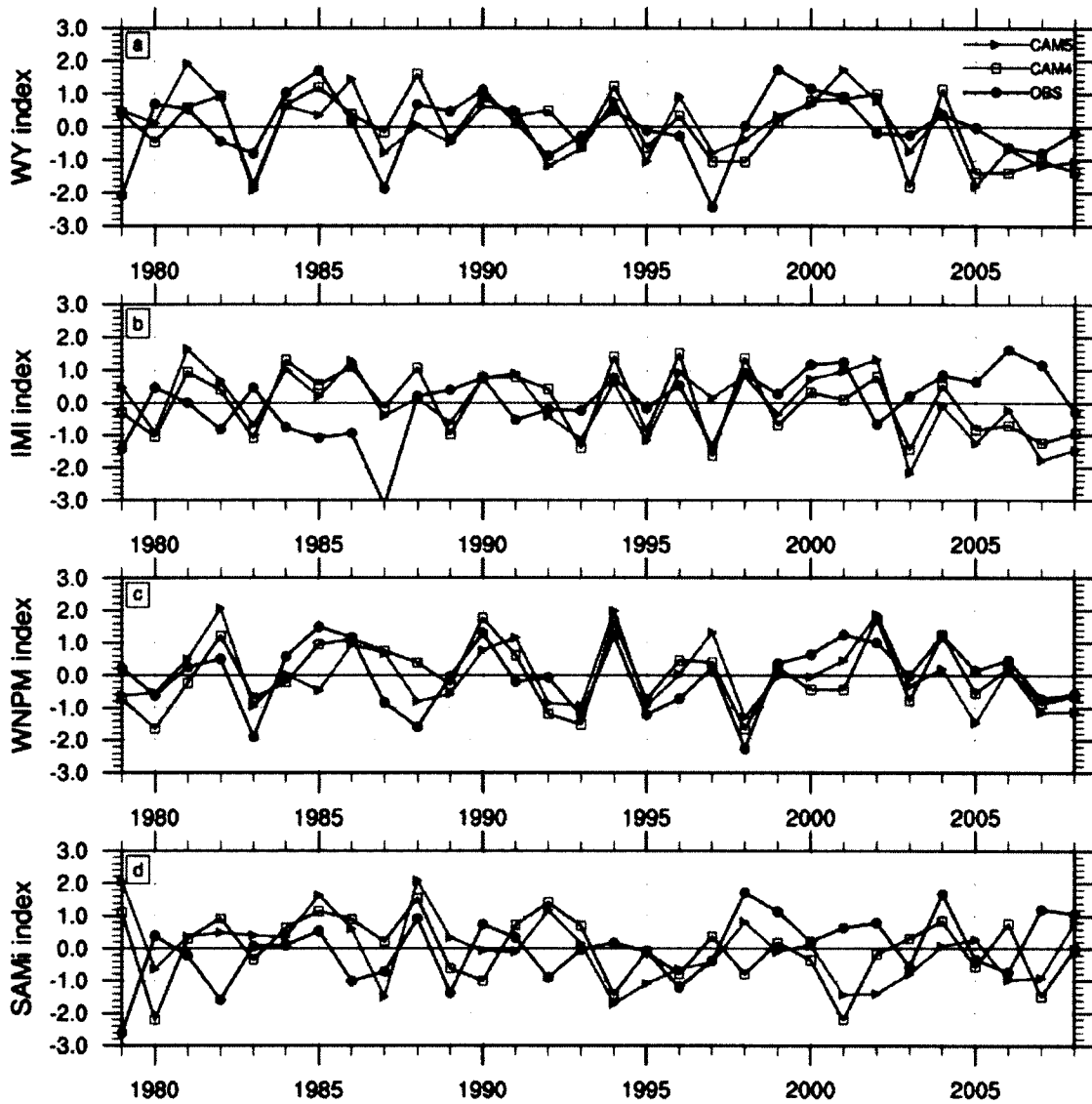


Figure 2.7: Time series of (a) Webster–Yang (WY) index, (b) Indian Monsoon index (IMI), (c) Western North Pacific monsoon (WNPM) index, and (d) South Asian monsoon (SAM_i) index of observation (CMAP/NCEP, black line), CAM4 (blue line) and CAM5 (red line). Details of all the indices are given in Table 2.1. The time series are normalized and thus unitless.

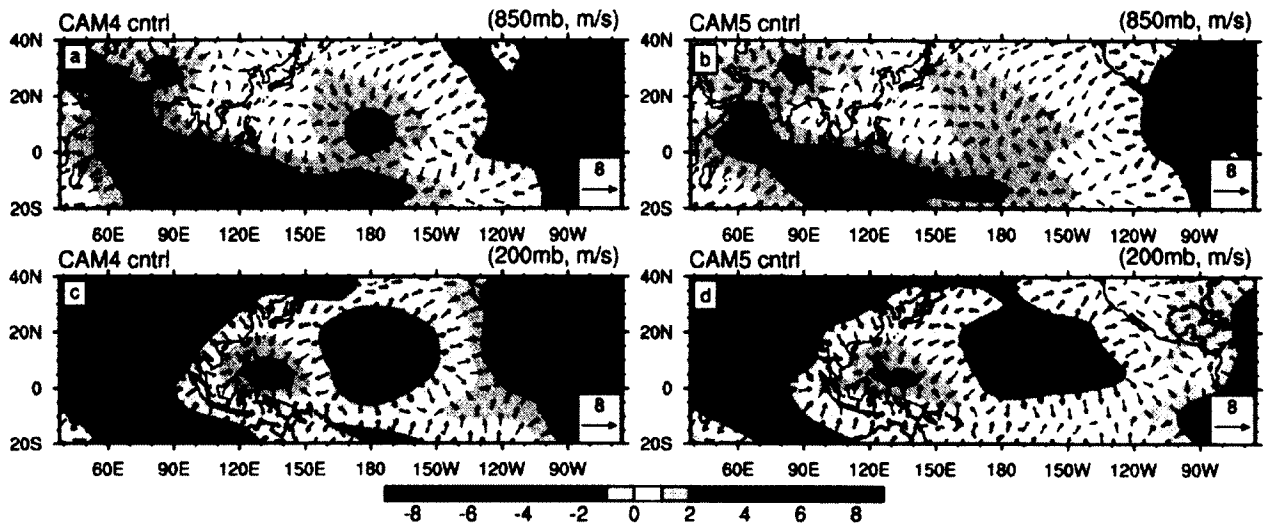


Figure 2.8: Difference between model (CAM4 and CAM5) and observed (NCEP) JJAS mean velocity potential ($10^{-6}\text{m}^2/\text{s}$) and corresponding divergent winds (m/s) at (a), (b) 850 and (c), (d) 200 mb.

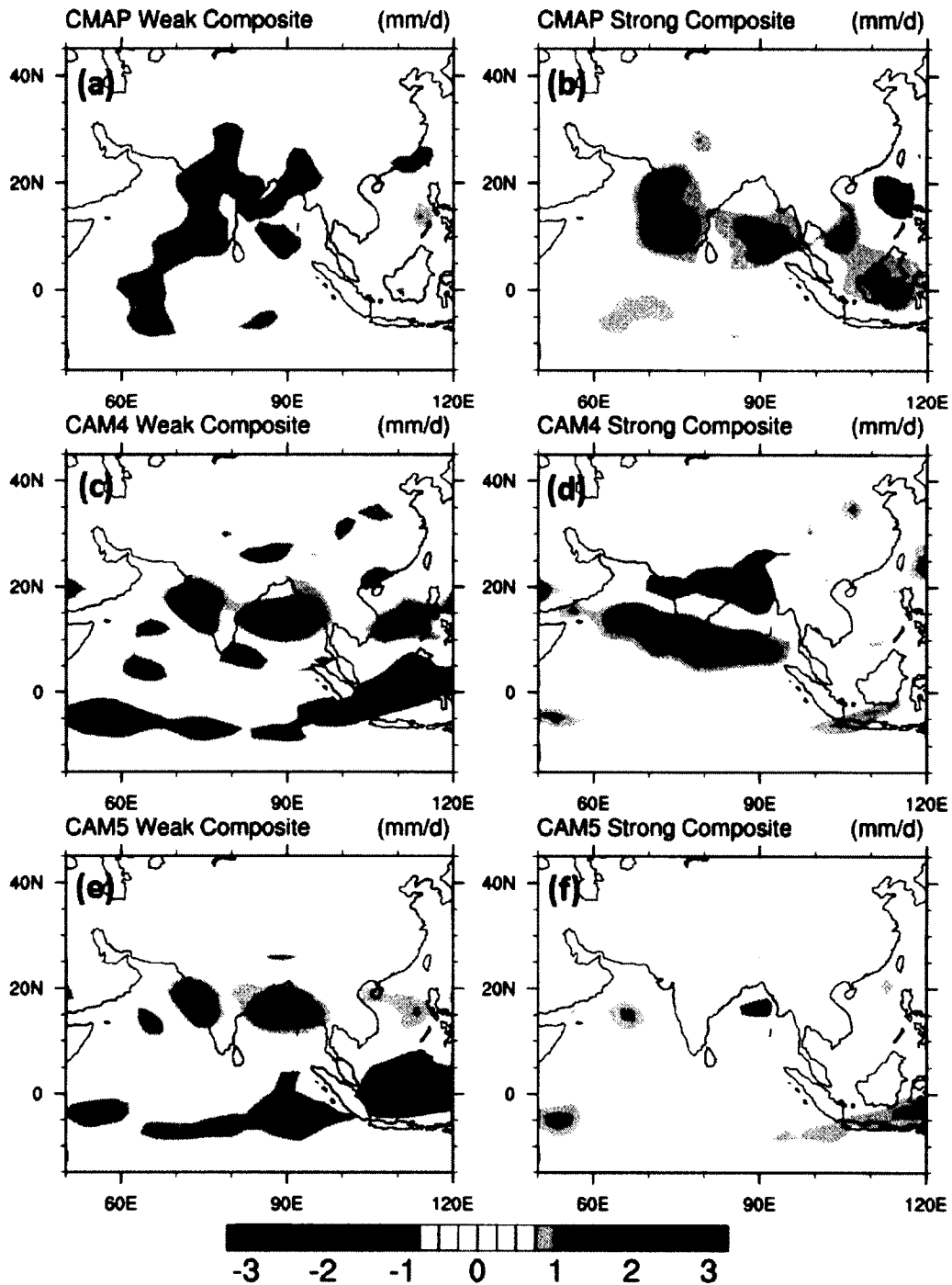


Figure 2.9: June–September (JJAS) anomaly precipitation composites of weak (1982, 1984, 1986, 1987, 1989 and 2002) and strong (1980, 1981, 1983, 1988, 1994, 1996, 1998 and 2007) monsoon years for (a, b) observation (CMAP), (c, d) CAM4 and (e, f) CAM5. Units are in mm/day.

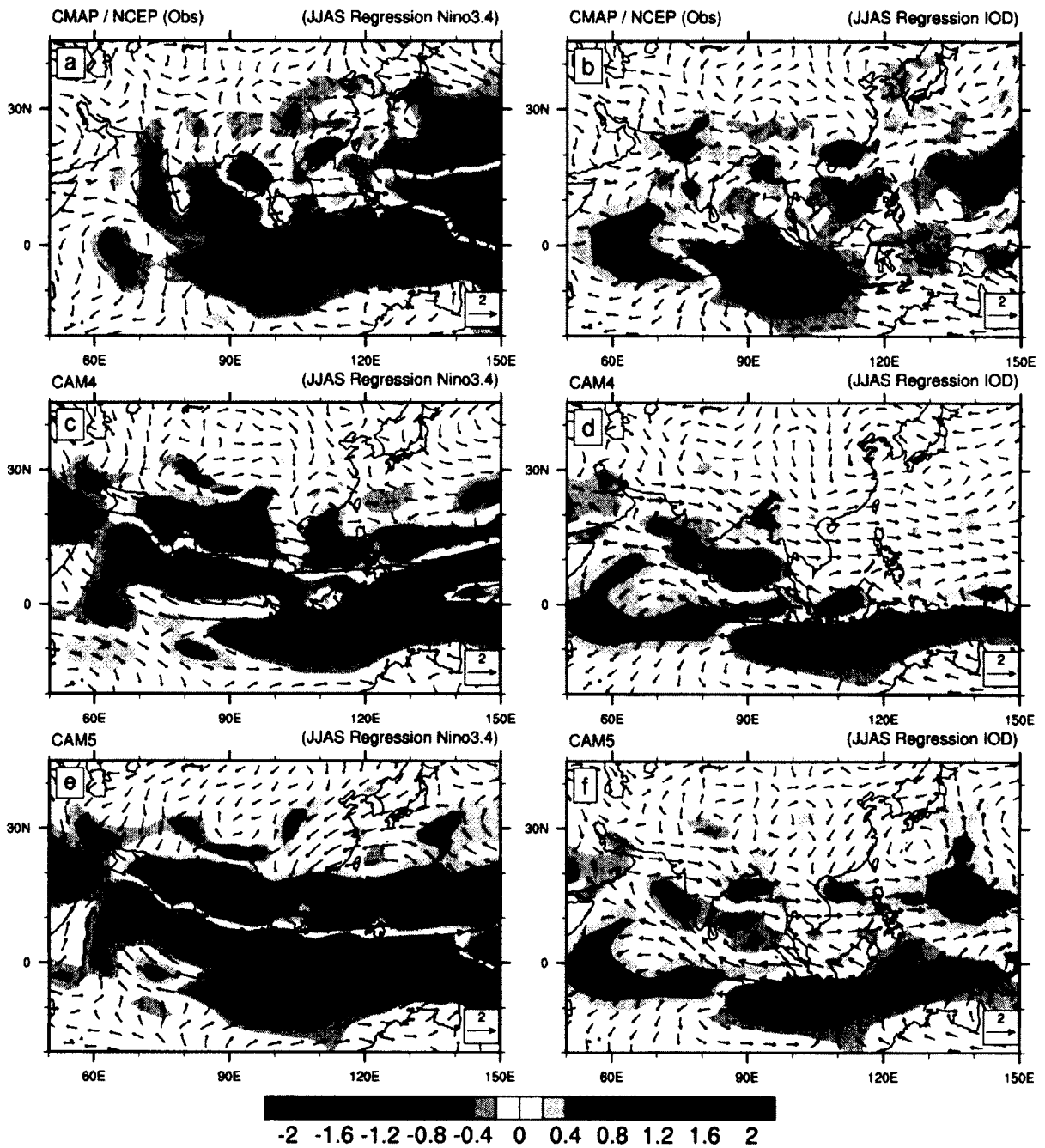


Figure 2.10: The linear regression of observed June–September (JJAS) Niño3.4 (-5°S – 5°N , 120° – 170°W) and IOD ($(-10^{\circ}\text{S}$ – 10°N , 50° – $70^{\circ}\text{E}) - (-10^{\circ}\text{S}$ – 0° , 90° – $110^{\circ}\text{E})$) SST indices with June–September (JJAS) observed and simulated precipitation and 850 mb winds. (a, b) observation (CMAP/NCEP), (c, d) CAM4 and (e, f) CAM5.

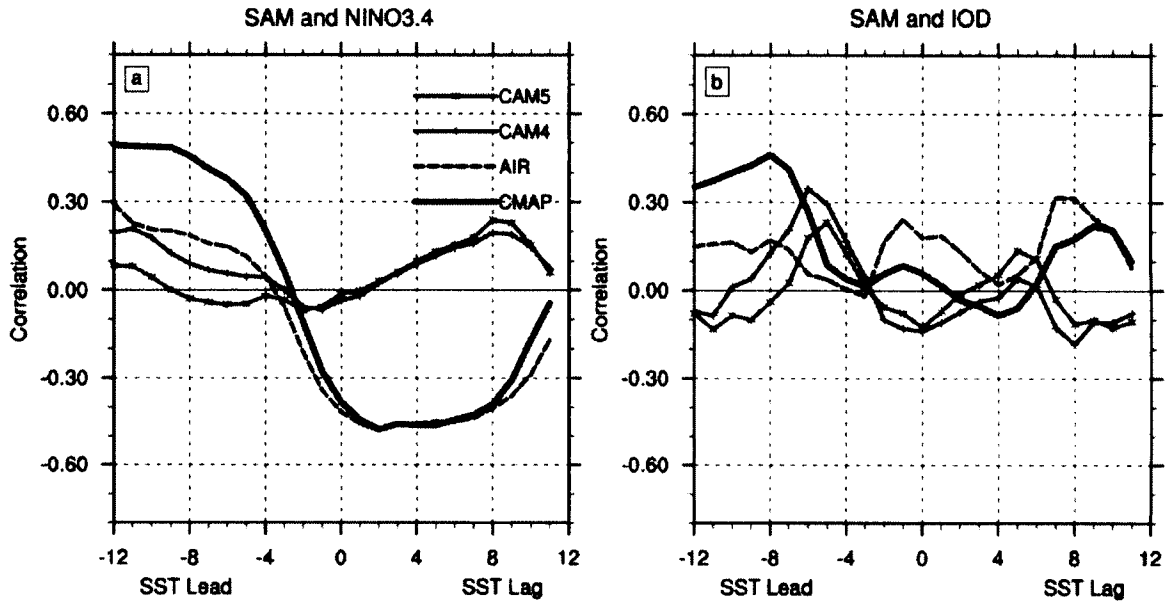


Figure 2.11: Lag-lead correlation of monthly mean precipitation with (a) Niño3.4 ($-5^{\circ}\text{S}-5^{\circ}\text{N}$, $120^{\circ}-170^{\circ}\text{W}$) and (b) IOD ($(-10^{\circ}\text{S}-10^{\circ}\text{N}, 50^{\circ}-70^{\circ}\text{E}) - (-10^{\circ}\text{S}-0, 90^{\circ}-110^{\circ}\text{E})$) indices. Area averaged ($0^{\circ}-40^{\circ}\text{N}$, $55^{\circ}-100^{\circ}\text{E}$) time series (ISR) of observed CMAP (solid black line) precipitation, observed All-India Precipitation (AIR - dashed black line) time series and simulated (CAM4, solid blue line and CAM5, solid red line) time series are correlated with observed Niño3.4 and IOD SST indices. The month with negative (positive) sign indicate that SST leads (lags) the ISR with maximum lead of 12 months (1 year). Month 0 and 12 indicates June whereas month 4 and 8 correspond to February and October (minus sign for previous month). Correlations are calculated using a 5 month sliding window.

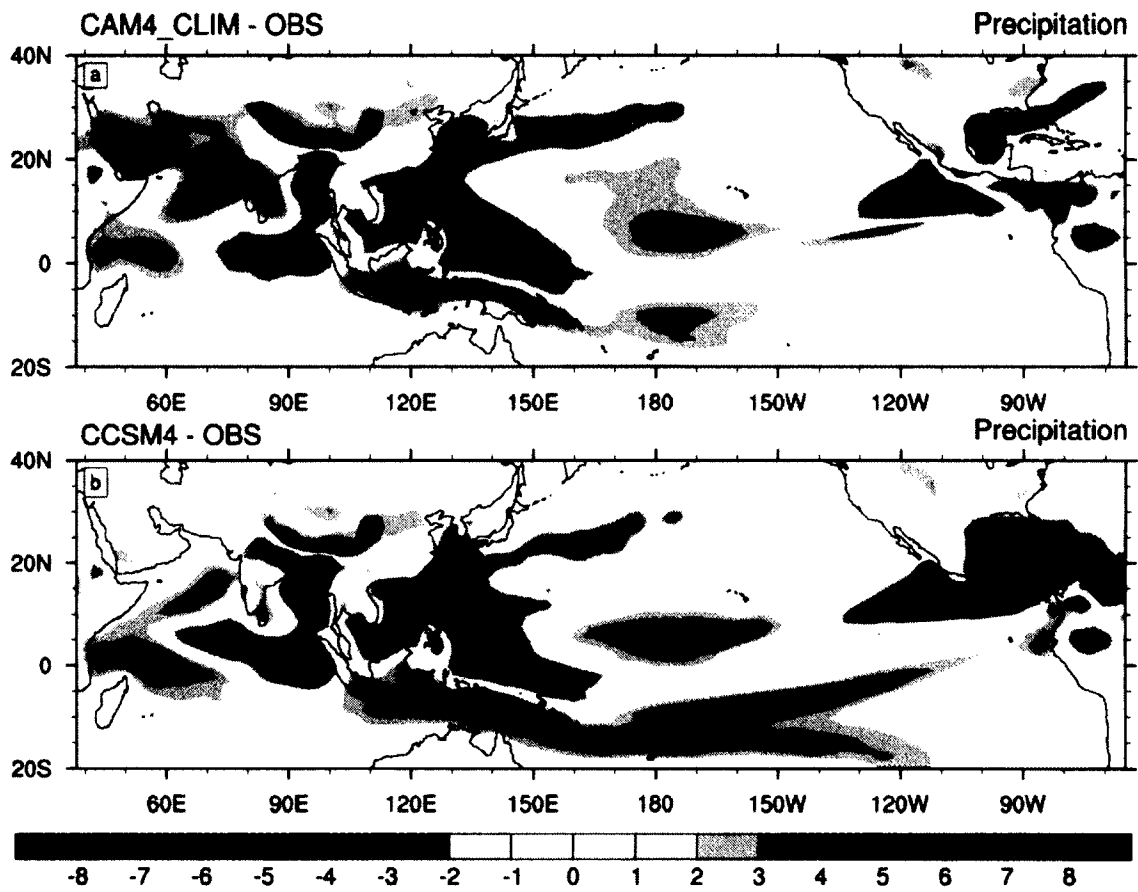


Figure 2.12: June–September (JJAS) mean differences between simulation and climatology (CMA) for: (a) CAM_CLIM (CAM4 climatology run) and (b) CCSM4. Shading corresponds to the precipitation difference in mm/day.

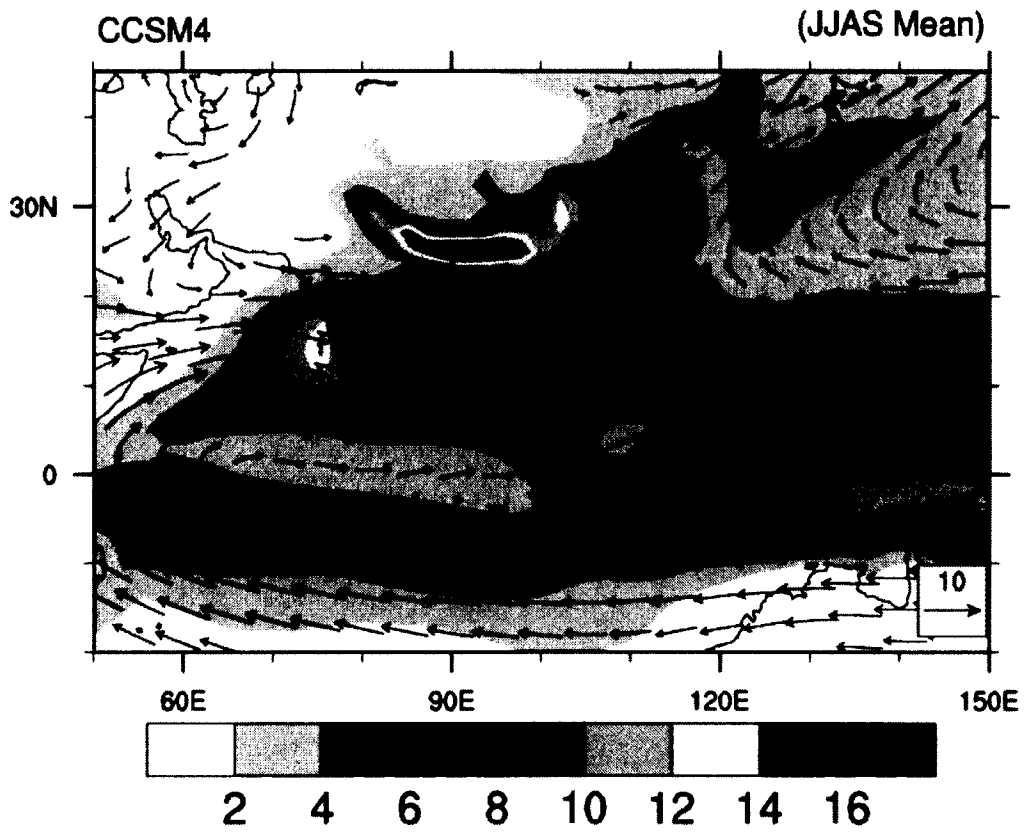


Figure 2.13: Same as Figure 2.3 but for CCSM4. Precipitation (shaded) in mm/day and 850 mb winds (vectors) in m/s.

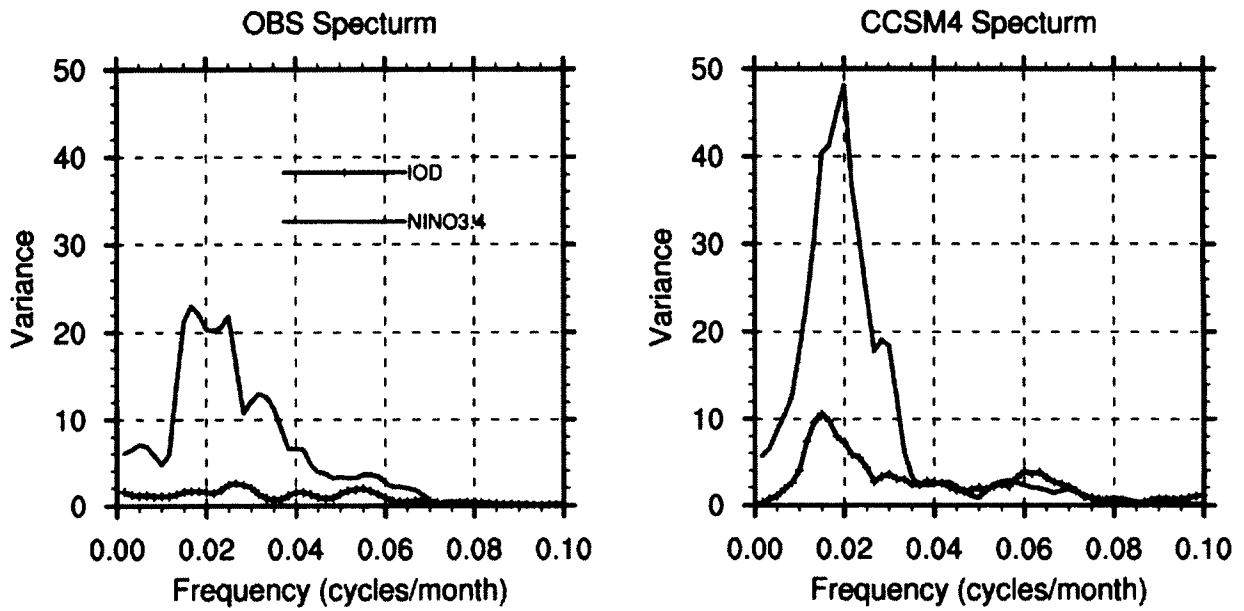


Figure 2.14: The variance power spectrum for (a) observed SST (HadSST) and (b) CCSM4. Niño3.4 (-5° – 5° N, 120° – 170° W) SST index is in a solid red line and IOD ($(-10^{\circ}$ S– 10° N, 50° – 70° E) - $(-10^{\circ}$ S– 0° , 90° – 110° E)) index is in a solid blue line.

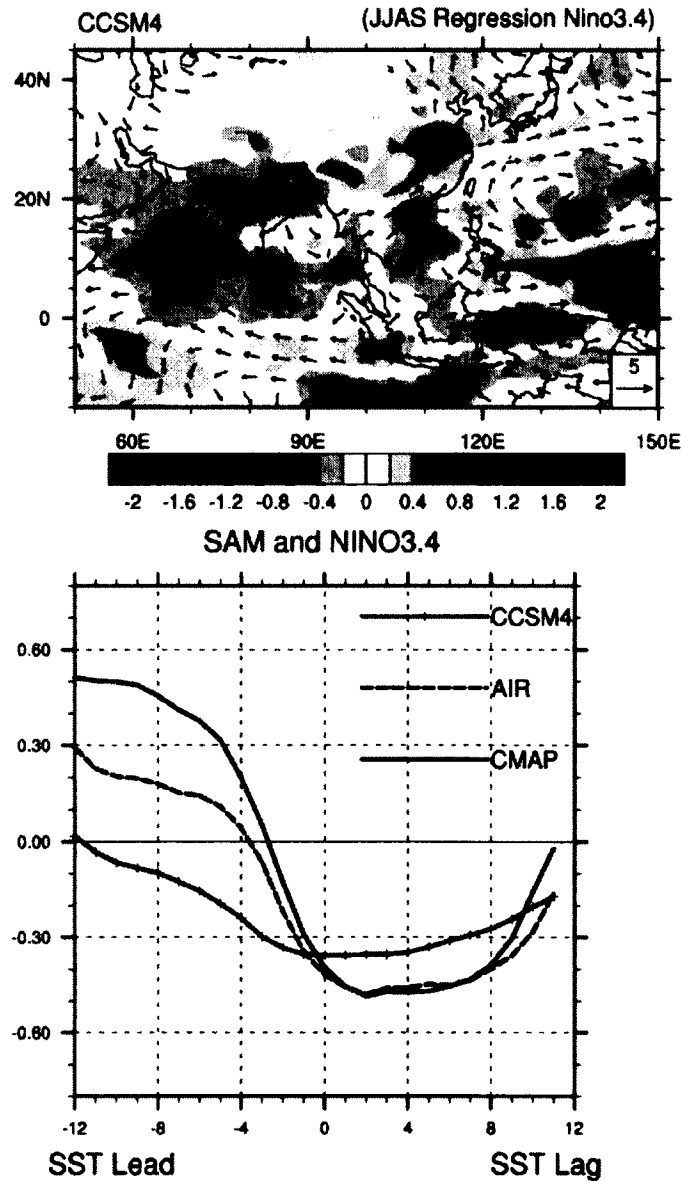


Figure 2.15: The linear regression (Top) of CCSM4 June–September (JJAS). Niño3.4 (-5°S – 5°N , 120° – 170°W) SST index with June–September (JJAS) simulated precipitation and 850 mb winds. Lag-lead correlation (Bottom) of CCSM4 monthly mean precipitation with CCSM4 Niño3.4 (-5°S – 5°N , 120° – 170°W) SST index. Area averaged (0° – 40°N , 55° – 100°E) time series (ISR) of observed CMAP (solid black line) precipitation and observed All-India Precipitation (AIR - dashed black line) time series are correlated with observed Niño3.4 SST index. Correlations are calculated using a 5 month sliding window.

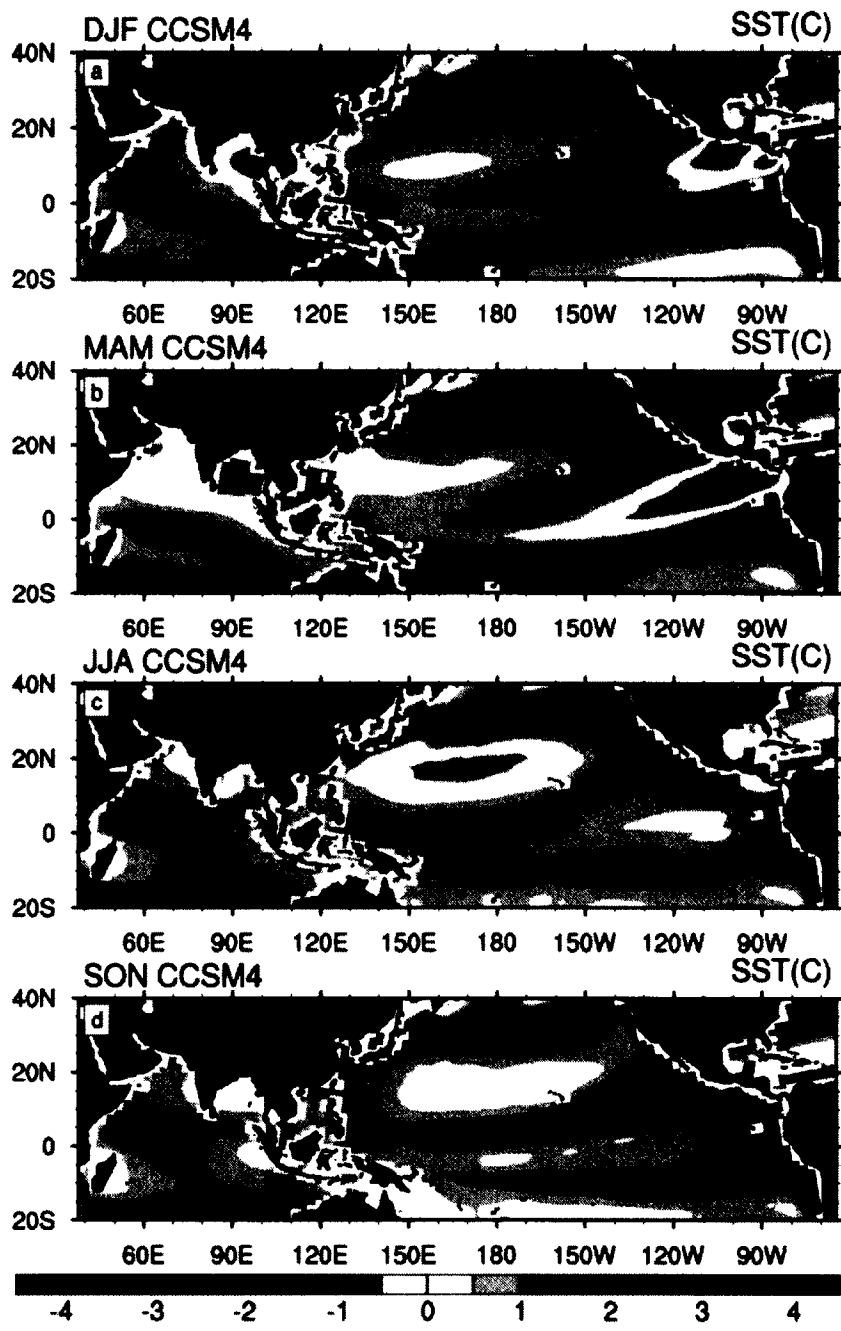


Figure 2.16: Seasonal SST differences between CCSM4 and observation (HadSST) for a thirty year mean climatology during: (a) December–February (DJF), (b) March–May (MAM), (c) June–August JJA and (d) September–November SON. The shading corresponds to model SST bias in °C (red for warm SST and blue for cold SST).

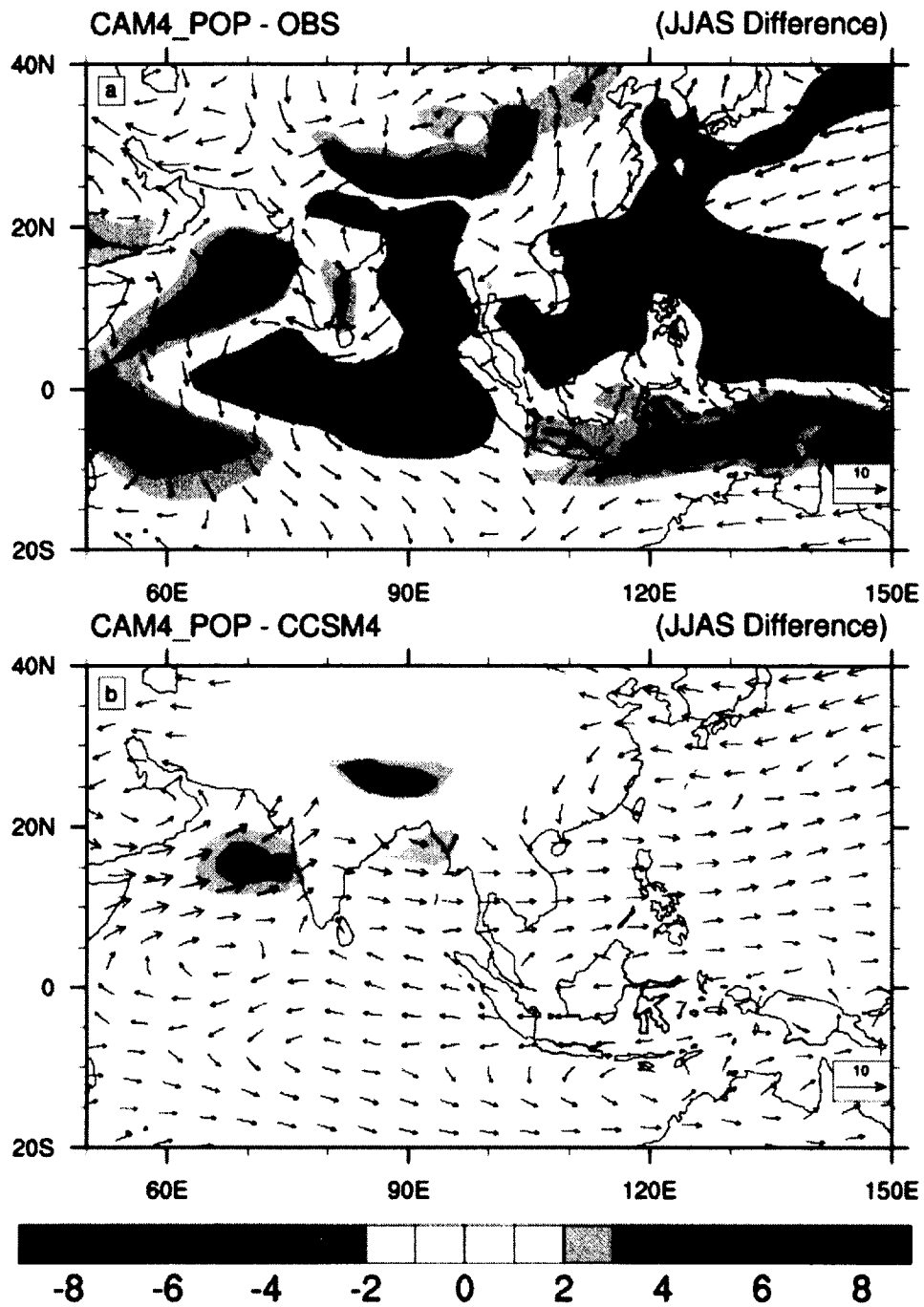


Figure 2.17: June–September (JJAS) differences of (a) CAM4_POP (simulation forced with the predicted SST of CCSM4) from observation (CMAP/NCEP) and (b) from CCSM4. Shading corresponds to the difference in mm/day whereas vector represents 850 mb winds in m/s.

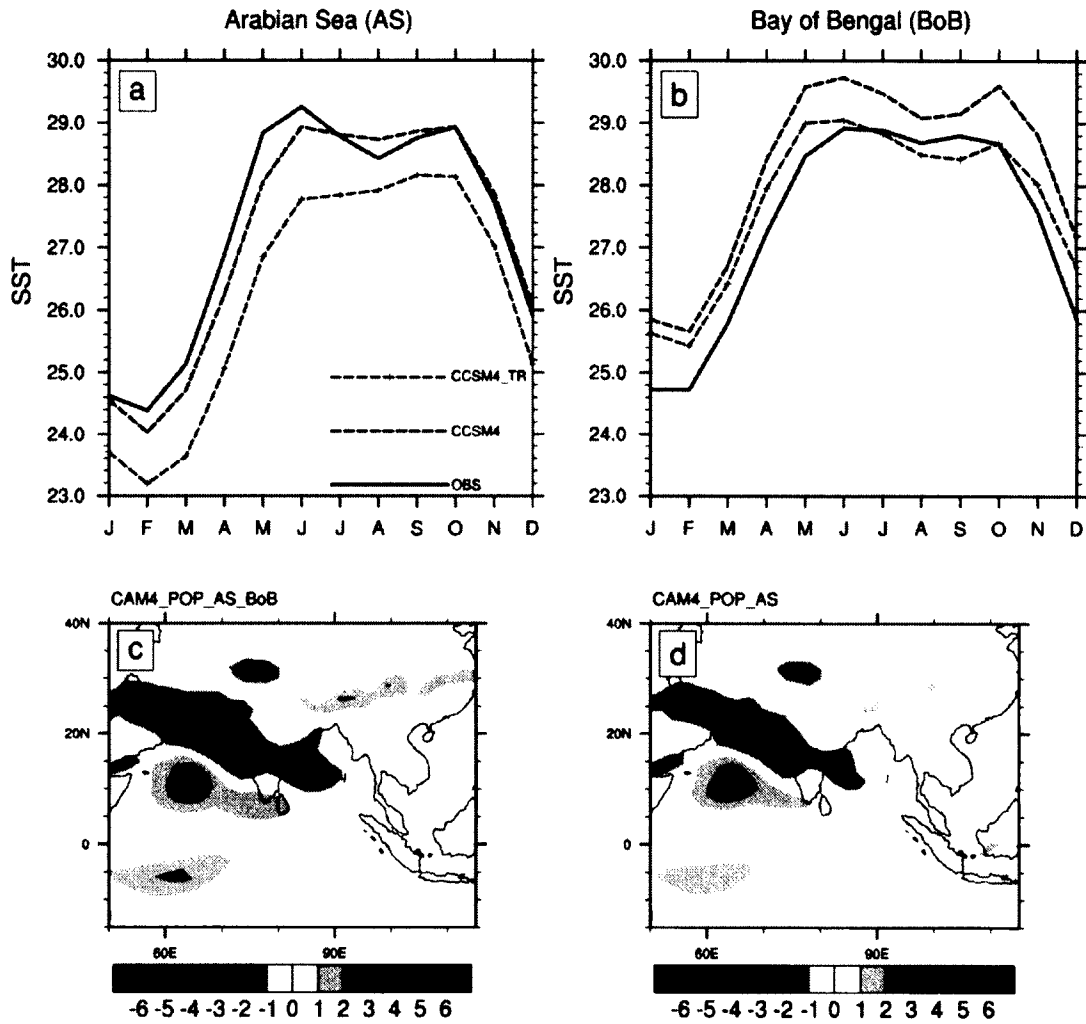


Figure 2.18: Annual cycle of observed SST (HadSST, solid black line) and simulated SST (CCSM4, blue dotted line and CCSM4_TR, red dotted line) over (a) Arabian Sea (40° – 80° E, 7° – 30° N) and (b) Bay of Bengal (80° – 100° E, 7° – 30° N). (c) June–September (JJAS) mean precipitation difference of CAM4_AS_BoB (CAM4 climatology SST run with SST modification in both Arabian Sea and Bay of Bengal) from CAM4_CLIM (CAM4 climatology SST run). (d) Same as (c) but for CAM4_AS run (with SST modification in Arabian Sea only). The shading corresponds to the difference in mm/day.

Chapter 3

Further Investigation of ENSO-Monsoon relationship in climate models: A new validation strategy

Islam S, Y Tang and P Jackson (2015), Further Investigation of ENSO-Monsoon relationship in climate models: A new validation strategy, in review process, to be submitted to Atmosphere-Ocean Journal

This manuscript is reformatted to serve as Chapter 3 in the thesis.

3.1 Introduction

The relation between ENSO and SAM summer precipitation is one of the earliest observed teleconnections in global climate studies (Walker 1924). As discussed in Chapter 2, SAM tends to experience a below (above) normal monsoon during an El Niño (La Niña) or the tropical eastern Pacific Ocean warm (cold) event (Sikka 1980; Ropelewski and Halpert 1987). In the last few decades, many efforts have been made to understand the ENSO-monsoon relationship including its physical mechanisms (Mooley and Parthasarathy 1984; Shukla and Paolino 1983; Webster and Yang 1992; Ju and Slingo 1995 and many others). The ENSO-SAM relationship can be explained by the variation of the Walker circulation (Shukla and Wallace 1983; Palmer et al. 1992; Soman and Slingo 1997). For example, during El Niño, the ascending branch of the Walker circulation moves eastward due to the abnormal warming in the central and eastern Pacific and accounts for below normal precipitation over the SAM region.

Apart from the remote impact of the Pacific Ocean, either through atmospheric circulation or oceanic currents, on the SAM, the Indian Ocean can also influence the SAM variability (Boschat et al. 2012). The Indian Ocean affects SAM variability in many different ways particularly through the IOD positive and negative modes. Its complex linkage with SST in Pacific Ocean can also modulate the SAM variability which can be seen in the frequent co-occurrence of IOD and ENSO events. Several studies have investigated the effect of Indian Ocean in modulating the ENSO-Indian monsoon teleconnection (Webster et al. 1999; Ashok et al. 2001) and have shown that the role of air-sea interaction in the Indian Ocean related to the monsoon dynamics is crucial for the ENSO-monsoon teleconnection.

Many studies have investigated the link and feedback between the Indian Ocean SST and ENSO in observation or in models (Saji et al. 1999; Webster et al. 1999). It has been found that both Indian and Pacific Oceans SST anomalies affect SAM in different ways depending on their phases, amplitudes and interactions. For example, Schott (2009) found that the impacts of both the Pacific and Indian Oceans on SAM are complicatedly linked due to the frequent co-occurrence of ENSO and IOD events. Krishnamurthy and Shukla (2008) have also shown that ENSO and the Indian Ocean variability may act together or against each other in certain years.

As ENSO is a key source of SAM variability, a realistic ENSO-Monsoon relationship is one of the prerequisites of a climate model for reliable monsoon simulations and predictions. Before using climate models for SAM prediction, the systematic errors in simulating the ENSO-Monsoon relationship must be addressed, since a poorly represented tele-connection consequently limits the prospects for seasonal monsoon prediction. Studies such as Sperber and Palmer (1996) and Wang et al. (2004) investigated many AGCMs, forced with prescribed SST, and showed that the poor interannual variations of SAM precipitation are mainly due to an incorrect SST-precipitation teleconnection. It is reported that the models with better representation of the ENSO-SAM teleconnection result in the best simulation of the mean climate, revealing the link between model climatology and interannual variability. Despite the fact that some coupled models can produce a realistic simulation for many variables, the monsoon variability and its teleconnections to ENSO is not properly simulated in model due to poor representation of the air-sea interactions and SST bias (Bollasina and Nigam 2009). Many coupled CGCMs, where the sea surface is not prescribed but evolves

naturally, feature systematic biases in their mean climate, particularly in the SST field and fail to realistically capture negative ENSO-SAM correlation (e.g. Achuthavarier et al. 2012).

In a recent study, Wu et al. (2012) (WU12 here after) used observations to identify three different types of ENSO influences on SAM precipitation variability, and to explore their possible physical mechanisms. They showed that the anomalous SAM precipitation can be induced by different influences of east equatorial Pacific SSTs, including the indirect influence of the SST anomalies of the preceding winter (DJF-only), the direct influence of the SST anomalies of the concurrent summer (JJAS-only) and the combined influence of both the preceding winter and concurrent summer SST anomalies (DJF&JJAS). The DJF-only type reflects the years with development of ENSO in the east equatorial Pacific region, the JJAS-only type are the years when ENSO decays from its mature phase and DJF&JJAS type are the years when ENSO changes its sign from positive (negative) to negative (positive). In all of these different SST influences, the SAM exhibits above or below normal rainfall, suggesting its strong response to changes in east equatorial Pacific.

Motivated by the WU12 analysis, which provides the basis for this study, we examine the three different ENSO-SAM relationships in atmospheric (CAM4) and coupled (CCSM4) model simulations using the WU12 methodology. In Chapter 2, both climate models are validated for their mean monsoon climatology and interannual variability including the brief analysis of their ENSO-SAM teleconnection. In this chapter, we extend the ENSO-SAM teleconnection analyses by characterizing the models' performance in the different ENSO-SAM types i.e. DJF-only, JJAS-only and DJF&JJAS.

The primary objective of this work is to investigate which type of ENSO-SAM teleconnection is better represented in simulations with and without air-sea coupling, and how these teleconnections are affected by SST bias (in the coupled model). We emphasize the processes connecting ENSO to the SAM in simulations of each ENSO-SAM type by highlighting each model's systematic biases. We also investigate the role of the Indian Ocean particularly the northern Indian Ocean to explore how it contributes toward anomalous SAM rainfall. This is explored by isolating northern Indian Ocean from ENSO by means of CAM4 idealized experiments by specifying prescribed SST anomalies in the tropical Pacific Ocean and climatology SST in the Indian Ocean. It is expected that this kind of models' validation will be helpful in their continuous evolutions toward better simulations which indirectly leads to a better model forecasting capability, particularly over the SAM region.

This chapter is organized into three sections. Section 3.2 describes the methodology used for making composites, the simulation data and the idealized experiments. Section 3.3 investigates the different ENSO-SAM relationships in CAM4 and CCSM4 simulations. Section 3.4 highlights the results of idealized experiments and concludes the discussion.

3.2 Models, Experiments and Methodology

The detailed description of CAM4 and CCSM4 models is already documented in Chapter 2, section 2.2. A brief description will be provided here.

The 32-year (1979 to 2009) CAM4 control ensemble simulations, forced with observed prescribed SST and sea ice data (HadSST, Reynolds et al. 2002), are conducted at $1.9^{\circ} \times 2.5^{\circ}$ horizontal resolution grid using the finite volume dynamical core with 26 vertical levels and a hybrid terrain-following coordinate system. To account for the uncertainty in simulations,

an ensemble strategy is used for the CAM4 experiments by using 6 hourly lagged initial conditions. This allows us to separate the “SST-forced” (or external) response. Ten ensemble members are constructed using the time lag ensemble strategy and the ensemble mean is used in all the analyses of CAM4 control simulations.

In CCSM4, the last 50 years from a 100-year simulation, forced with present day climatological boundary conditions, is used for coupled simulation composites. The first fifty years are discarded as the equilibration time for CCSM4 model. The horizontal resolution of $1.9^\circ \times 2.5^\circ$ and finite volume grids are used for CCSM4 atmospheric and land models, whereas the ocean and ice models share the same $1^\circ \times 1^\circ$ resolution with a displaced pole grid.

Two different 32-year (1979 to 2009) sensitivity experiments are performed by CAM4 for two ideal scenarios, namely CAM4_ENSO_IO and CAM4_ENSO. In the CAM4_ENSO_IO experiment, the observed SSTs (HadSST) are used to force the CAM4 in both the Indian and Pacific Oceans whereas the climatology SST is used elsewhere. In the CAM4_ENSO experiment, the observed SSTs are only used for the Pacific Ocean while keeping the climatological SST elsewhere. To reduce the uncertainties, ten ensemble simulations are performed for both idealized experiments using the same time lag ensemble strategy as used for the CAM4 control simulation.

Observed precipitation data from the Climate Prediction Center (CPC) Merged Analysis of Precipitation (CMAP; Xie and Arkin 1997) are used for comparison. National Centers for Environmental Prediction (NCEP; Kistler et al. 2001) reanalysis data are used to validate

winds. Observed SST (HadSST) data (Reynolds et al. 2002) are used for calculating observed SST indices and to validate coupled model SST.

Following the WU12 methodology, for constructing composites, the years exhibiting different types of ENSO-SAM impacts are selected based on the year-to-year variations of SAM and Niño3.4 SST indices in the preceding winter and concurrent summer. The SAM intensity is measured by its area averaged precipitation over 5° - 25° N and 60° - 100° E. The anomalous SAM is characterized based on the criteria that the magnitude of its rainfall anomalies exceeds 0.5 standard deviation above the mean in summer during an ENSO year. The area averaged anomalies of SST are calculated over -5° - 5° N and 120° - 170° W for Niño3.4 (ENSO) and 5° - 25° N and 60° - 100° E for northern Indian Ocean. The ENSO years are selected based on the criteria that five consecutive 3-month running mean SST anomalies in Niño3.4 region exceed 0.5° C.

Based on the anomalous SAM rainfall criteria discussed above, different years are selected in observation and simulation. The bimonthly composite of selected years are made for each type of ENSO-SAM teleconnection using the WU12 methodology, as outlined below. Throughout the text, DJF and JJAS months correspond to winter and summer season and MAM and SON reflects spring and fall. When required, the physical interpretation of the composites based on observation data is mostly adopted from WU12.

DJF-only: A positive (negative) preceding DJF Niño3.4 SST anomaly is followed by a positive (negative) SAM anomaly with the requirement that the concurrent JJAS Niño3.4 SST anomaly is not opposite of the SAM anomaly. This is to distinguish it from the DJF&JJAS type mentioned below. In this type, the Niño3.4 SST anomalies decrease or

remain unchanged from preceding DJF to concurrent JJAS, indicating that the ENSO either decays or persists.

JJAS-only: A positive (negative) concurrent JJAS Niño3.4 SST anomaly is accompanied by a negative (positive) SAM anomaly with the condition that the preceding DJF Niño3.4 SST anomaly is not of the same sign as the SAM anomaly. That results in Niño3.4 SST anomalies that increase or remain unchanged from preceding DJF to concurrent JJAS, indicating that the ENSO either develops or persists.

DJF&JJAS: The Niño3.4 SST anomaly switches from positive (negative) in preceding DJF to negative (positive) in concurrent JJAS and the SAM anomaly is positive (negative). In this type, the ENSO switches its phase during the half year period.

In this study, the anomalous SAM years in observations (CMAP) are the same as those in WU12 i.e. 1983, 1984, 1985, 1989, 1999 and 2001 for the DJF-only type, 1982, 1996, 2002 and 2004 for the JJAS-only type and 1988, 1998 and 2007 for the DJF&JJAS type. In CAM4 simulations, which are forced with monthly observed SST, we consider the same years as anomalous SAM years although the magnitude of the SAM index does not meet our criterion at least of 0.5 standard deviation in some years. For CCSM4 model simulation, both anomalous SAM and ENSO years are identified based on the criteria described above, since the coupled model does not include any observed information in its simulation. The investigation of SAM and Niño3.4 indices in coupled simulations revealed that there are 6 DJF-only type, 5 JJAS-only type and 5 DJF&JJAS type years in CCSM4.

3.3 Results and Discussion

We first focus our attention on the observed and simulated lag-lead correlation of the SAM index with Niño3.4 and northern Indian Ocean indices. Figure 3.1 shows the SAM relationships with ENSO and northern Indian Ocean in observation and simulations. Observed CMAP (solid black line) and CAM4 (solid blue line) SAM rainfall indices are correlated with observed Niño3.4 and northern Indian Ocean SST indices whereas CCSM4 (solid red line) SAM rainfall indices are correlated with the simulated Niño3.4 and northern Indian Ocean SST indices. As discussed in Chapter 2, the observations show that strong negative correlations can be found between the SAM summer rainfall and the SSTA from the concurrent summer to the following winter, representing a weak (strong) SAM in El Niño (La Niña) developing years. In the CAM4 model, the negative correlation relationship is quite weak reflecting the lack of correct teleconnection of SSTA to SAM summer rainfall. Actually the CAM4 simulations reflect an opposite relationship between ENSO and SAM during a boreal summer, with very small correlation coefficients. It also shows there is no relationship between SSTA in the late spring and the SAM summer rainfall, which is common in many models that have difficulties in capturing summer precipitation, due in part to monsoon “spring prediction barrier” (Webster and Yang 1992). In case of the CCSM4 model, the negative correlation is captured comparatively better than CAM4 but still is quite different from observations. No significant conclusion can be made regarding the spring predictability barrier in CCSM4.

In Figure 3.1b, the lag-lead correlation of SAM summer rainfall with northern Indian Ocean is computed using observed data. A weak positive correlation can be found between the SAM summer rainfall and the SSTA during late spring and summer whereas negative correlation

can be found between the SAM and SSTA from the concurrent summer to the following winter. The negative correlation of SAM summer rainfall to the SSTA of the following winter suggests a negative feedback of SAM on the northern Indian Ocean. The negative feedback features enhanced (reduced) surface winds and evaporation inducing negative (positive) SST anomalies (Wu and Kirtman, 2004). The negative feedback of SAM is not reproduced in CAM4 and CCSM4 as they only show positive correlation. The CAM4 shows more positive values of correlation as compared to CCSM4 due to lack of an air-sea interaction in the Indian Ocean. In the CAM4 model, such a negative feedback is suppressed because the SST cannot respond to atmospheric changes.

The lag-lead result suggests that neither model can represent the ENSO-SAM interaction correctly. However, this lag lead correlation is based on all the years of model simulations. How the model simulates different types of ENSO-SAM teleconnection (as mentioned in the introduction) and which type of relationship is better simulated by the model can lead to a more reliable validation of a model. We therefore further investigate the ENSO-SAM relationship based on its different types, and examine the performance of both models for each type separately based on the analysis of composites.

3.3.1 Composite Analysis

We follow the procedure discussed in WU12 in constructing the composite. For each ENSO-SAM4 type, composites are constructed by averaging the years mentioned in section 3.2. To simplify the analysis and spatial representation, the composite of each ENSO-SAM4 type is constructed to reflect positive anomalies of SAM summer rainfall i.e. SAM anomalies are reversed (by multiplication of -1) in the years when it is negative and grouped together with

the years when it is positive. Although WU12 discussed the physical mechanism of different types of ENSO-SAM relationships using observations, it is important to extend this analysis to model data and to explore the models ability in characterizing each type of ENSO-SAM relationship.

3.3.1.1 DJF-only Composite

Two month composite anomalies of observed SST for the DJF-only type are shown in Figure 3.2 (1st column) for Dec-Jan (DJ), Feb-Mar (FM), Apr-May (AM), Jun-Jul (JJ), and Aug-Sep (AS). This composite shows the yearly evaluation of SST from the preceding winter to the concurrent summer. The evolution of ENSO decay is characterized by a gradual decrease in SST from its mature phase in the preceding DJ to a weakened phase in the concurrent AS in the equatorial Pacific. Opposite to the ENSO decay phase, the positive SST anomalies in northern Indian Ocean are developed from the preceding DJ to concurrent JJ, and then decreased afterward.

The accompanying bimonthly rainfall variation can be seen in Figure 3.3 (column 1) depicting the decay of anomalous rainfall over the equatorial Pacific consistent with the decay of ENSO in east equatorial Pacific while the rainfall anomalies over the SAM region grow significantly in summer. Over the SAM region, rainfall anomalies behave in a dipolar form over the Indian Ocean with different signs between the east and west in the preceding DJ which change from north to south in FM to AM. Above normal rainfall develops over the Arabian Sea in JJ spreading over the Indian subcontinent and the Bay of Bengal in AS.

The composite bimonthly rainfall variation of CAM4 is shown in Figure 3.3 (column 2). CAM4 reproduces the rainfall transition over the east Pacific reasonably well whereas

significant disagreement can be seen over the western Pacific and Maritime continent particular in DJ to AM. The model response over the Maritime continent is quite weak. The overall simulation in DJF-only type is reliable as the large scale features are similar to the observed rainfall anomaly decay over the tropical Pacific and the increase of rainfall over the Indian subcontinent in late monsoon (AS).

CCSM4 bimonthly composites of rainfall are shown in Figure 3.3 (column 3) whereas its simulated SST composites are presented in Figure 3.6 (column 1). In comparison with observations and CAM4, the CCSM4 rainfall composite exhibits large disagreements over different regions. The double ITCZ is simulated over the tropical Pacific Ocean along with significant differences in rainfall anomalies over the Indian Ocean in the preceding winter to early spring. The double ITCZ issue was also seen in the analysis of Chapter 2 (Islam et al. 2013). The large differences in CCSM4 rainfall composites are mainly due to the systematic errors in CCSM4 SST simulation (Figure 3.6 (column 1)) degrading SST atmospheric response to rainfall. The ENSO response in CCSM4, to anomalous SAM, is quite strong during its mature phase in winter. CCSM4 exhibits poor skill in spring (FM-AM) which is probably due to the spring barrier which is seen in many coupled models. Over all the anomalous SAM in CCSM4 is quite weak in early summer and comparable to observation in late summer. The CAM4 and CCSM4 comparison for this type (in the ENSO decay phase) reveal that the CAM4 model is better than CCSM4 in reproducing the anomalous rainfall, although both have significant biases.

3.3.1.2 JJAS-only Composite

Figure 3.2 (column 2) represents the bimonthly SST composite for the JJAS only type. The

developing phase of ENSO can be seen as the negative SST anomalies increase in the east equatorial Pacific from AM to DJ. The SST anomalies in the northern Indian Ocean, being weak in spring, change to strongly negative in late summer (AS) and DJ. The corresponding observed rainfall anomalies are shown in Figure 3.4 (column 1), with negative anomalies over the equatorial Pacific typical of those in La Niña years. These negative equatorial anomalies propagate to the eastern Pacific from JJ to DJ whereas positive rainfall anomalies increase over the Maritime continent from JJ to ON. Positive rainfall anomalies spread over the Arabian Sea, the Indian subcontinent, and the Bay of Bengal in early summer (JJ). In early fall (ON), negative rainfall anomalies begins over the tropical Indian Ocean and mature in the DJ.

In CAM4, although the equatorial rainfall is well captured, significant disagreements in JJ rainfall anomalies over the northern Indian Ocean and western Indian subcontinent can be seen in Figure 3.4 (column 2). The CAM4 response is quite dry compared to observations over the SAM region. In the CCSM4 model, Figure 3.4 (column 3), significant difference in rainfall patterns mainly over whole tropical belt of Indian and Pacific Oceans are seen. These are mainly induced by the simulated SST bias. Over the northern Indian Ocean and Indian subcontinent, the CCSM4 rainfall anomalies are better captured compare to those in the CAM4 simulations.

3.3.1.3 DJF&JJAS Composite

In the DJF&JJAS composite, ENSO switches from positive in winter to negative in summer (Figure 3.2 (column 3)). In the whole year evolution, the tropical Indian Ocean shows consistent positive SST anomalies. The accompanying rainfall anomalies (Figure 3.5

(column 1)) over the tropical Pacific follow the switch of east equatorial Pacific SST anomalies by being positive in winter and negative in late summer (AS).

CAM4 and CCSM4 simulations for this type are presented in Figure 3.5 (columns 2 and 3 respectively). CAM4 better reproduces the above normal rainfall anomalies over the northern Indian Ocean and Maritime continent in JJ and AS, whereas the CCSM4 model reproduces quite poor rainfall response over the same region. This finding shows that this type of the ENSO-SAM relationship is not properly captured in the CCSM4 simulation as compared to the uncoupled CAM4 model.

The above analyses are based on bi-monthly composites that reveal the yearly evolution of SST and rainfall. To analyze the SAM average JJAS (summer) response, we investigate the average composite rainfall anomalies for June, July, August and September months in all the three types. A comparison of JJAS means is shown in Figure 3.7 for the DJF-only, JJAS-only and DJF&JJAS types based on CMAP, CAM4 and CCSM4 rainfall. This analysis can conclude our discussion by showing that in all three types, CAM4 simulations are better for DJF-only and DJF&JJAS type whereas CCSM4 shows good simulation only in JJAS-only type, particularly over the SAM region. This means that only the concurrent response of SST is well represented in CCSM4.

Comparison of the JJAS mean composites, of Figure 3.7 with Figures 3.2, 3.3 and 3.4 indicates that in observations, the late summer (AS) rainfall anomalies contribute more towards the total mean SAM summer rainfall in DJF-only and DJF&JJAS types, whereas in the JJAS-only type, early summer (JJ) anomalies largely contribute to total JJAS mean rainfall. In these models, such contributions are not clear and therefore cannot be

differentiated due to their systematic errors over the SAM region.

3.3.2 Temporal Evolution of SST and SAM Rainfall

We now explore the temporal evolution of the ENSO-SAM relationship using area averaged indices. The SST index is calculated over the Niño3.4 and northern Indian Ocean region while the SAM index is calculated by averaging the observed or simulated rainfall over the SAM region. Figure 3.8 shows the normalized 3-month running mean anomalies of Niño3.4 SST, northern Indian Ocean SST and SAM rainfall for all the types for both observed (CMAP and HadSST) and simulated (CAM4 and CCSM4) rainfalls and SST indices.

As discussed in WU12, in the observations (Figure 3.8a, left column), positive Niño3.4 SST anomalies in the preceding winter are followed by positive northern Indian Ocean SST anomalies during spring through early summer in the DJF-only type, indicating the effect of preceding east equatorial Pacific SST anomalies on SAM through northern Indian Ocean SST changes. The SAM rainfall anomalies begin increasing in June and reach a maximum in late August and September. The delay of the SAM rainfall anomaly to the northern Indian Ocean SST suggests the positive feedback of the northern Indian Ocean warming to the SAM region in the form of more evaporation. The warm SST anomalies in the northern Indian Ocean in summer lead to lower level convergence and anomalous rainfall in summer (Chang et al. 2011).

The CAM4 rainfall over the SAM region follows the observed pattern except smaller in magnitude in the summer. CCSM4 SST indices, shown in Figure 3.8a (right column) basically follow the observed SST variation, whereas its rainfall patterns are different. In CCSM4, the warming in northern Indian Ocean region is not strong, probably resulting in

less impact on the SAM rainfall.

In the JJAS-only type (Figure 3.8b, left column), the northern Indian Ocean SST anomalies are negative in summer, leading to less favorable conditions for the SAM rainfall. In this type, negative east equatorial Pacific SST anomalies may directly induce an anomalous SAM via atmospheric circulation changes (WU12). These circulations modulate and amplify the SAM rainfall by increasing the convergence over the SAM area (WU12). In the CAM4 simulations, due to the absence of local air-sea coupling over the Indian Ocean, the atmospheric circulation cannot induce changes in the northern Indian Ocean SST which could be the reason that the CAM4 model is not properly reproducing the anomalous rainfall in this type. Air-sea coupling is important for atmospheric circulations caused by the large-scale ocean temperature gradient. This can be seen in the CCSM4 (Figure 3.8b, right column), where anomalous rainfall over the SAM region is better simulated than in CAM4 in summer. Another reason for better CCSM4 simulation is that the northern Indian Ocean SST warm anomaly in summer significantly contributes toward increasing the SAM rainfall. This makes it difficult to decide if the better representation of JJAS-only type in CCSM4 is purely due to the air-sea coupling or if it is due to the warm anomaly in CCSM4 northern Indian Ocean SST.

In the DJF&JJAS type, shown in Figure 3.8c (left column), positive northern Indian Ocean SST anomalies persist from the preceding winter to summer. In this type, the ENSO switches from a warming phase in winter to a cooling phase in summer, suggesting that the persistence of positive northern Indian Ocean SSTA is mainly due to the preceding winter positive east equatorial Pacific SST anomalies that cause the anomalous SAM. As in the JJAS-only type, the concurrent negative east equatorial Pacific SST anomalies may contribute to an

anomalous SAM via a direct atmospheric circulation change (WU12). Thus, both the preceding (via northern Indian Ocean) and concurrent (via atmospheric circulation) east equatorial Pacific SST anomalies result in an anomalous SAM rainfall (WU12). The CAM4 simulation reproduces this type remarkably well as compared to the DJF-only and JJAS-only types. This could be due to the persistent warm northern Indian Ocean SST anomalies, which are reflected in CAM4 simulations. In CCSM4 simulations, although the Niño3.4 pattern is a partial match for the observations, the rainfall response is quite the opposite. The likely source of CCSM4 failure to simulate the anomalous SAM summer rainfall is probably due to a decrease of persistence positive SST anomalies in the northern Indian Ocean in spring (3.8c, right column), causing less moisture evaporation. Indeed the CCSM4 ocean response is not consistent from preceding winter to concurrent summer in this type.

3.3.3 Response of Atmospheric Circulations

As discussed above in the JJAS-only and DJF&JJAS types, the anomalous SAM rainfall strongly modulates via the atmospheric circulation changes over the SAM region. We explore this in Figure 3.9 by plotting the JJAS mean composite anomalies of velocity potential and divergent winds at 850 mb and 200 mb heights for the JJAS-only and DJF&JJAS type. Observed winds are from NCEP reanalysis data sets whereas simulated winds are from CAM4 and CCSM4.

In the JJAS-only type, the anomalous SAM rainfall is induced by a direct SST forcing in the Pacific Ocean through large scale circulation changes. This can be seen in the observations for the upper level convergence and lower level divergence over the equatorial central Pacific and upper level divergence and lower level convergence over the Maritime continent,

Australia and SAM regions (Figure 3.9, row 1). In CAM4, while the low level convergence is captured over the Maritime continent, the SAM convergence zone is not reproduced which causes the poor anomalous SAM rainfall simulation in the JJAS-only type. CCSM4 shows strong convergence over the SAM region and this intensifies the anomalous SAM.

In the DJF&JJAS type (Figure 3.9, row 2) as discussed in WU12, the preceding positive east equatorial Pacific SST anomalies induce positive northern Indian Ocean SST anomalies through atmospheric circulation changes. Negative SST anomalies in the east equatorial Pacific produce lower level divergence and upper level convergence over the tropical Pacific. This leads to upper level divergence and convergence at the surface causing moisture to intensify over the SAM region. CAM4 convergence and divergence zones are comparable to observations whereas CCSM4 circulations are weak in these types and cannot reproduce the observed circulation patterns.

3.3.4 Response of Humidity and Land-Sea Thermal Contrast

It has been shown that land-sea heating contrast is a fundamental mechanism powering the summer monsoon circulation (Webster 1987; Young 1987). The relationship between land-sea thermal contrast and SAM has been investigated in many studies (Fu and Fletcher 1985; Meehl 1994a; Li and Yanai, 1996) where they found that the intensity of the SAM is related to the strength of the temperature gradient due to the land-sea thermal contrast. Increasing the temperature gradient increases the intensity of the SAM and vice versa. In this section, we compare the surface moisture and thermal contrast from observation and models in each ENSO-SAM type. Following the methodology of WU12, the surface air humidity is averaged over the western Indian Ocean (0° – 10° N, 50° – 80° E), as the increased moisture in this region

may be transported to the SAM region by mean southwesterly winds and thus may contribute to a stronger SAM rainfall. The thermal contrast is represented using a 500–200-hPa thickness difference between the zones from 20°–40°N, 50°–100°E and from 0°–20°N, 50°–100°E.

In Figure 3.10 (left column), negative thickness difference anomalies persist from winter to summer for the DJF-only type. Positive anomalies of surface air humidity are present in early spring and summer in western Indian Ocean and cause an increase in the moisture availability for the SAM region. The air humidity increases due to the positive SST anomalies during late spring and early summer (as in Figure 3.9). Although the CAM4 atmospheric response to thickness difference is quite consistent with observations, its moisture content peaks in late winter instead of summer. This means that the anomalous SAM summer rainfall is underestimated in CAM4 while its thermal contrast is negative over the SAM region. The positive moisture availability is found to have a reliable performance for the DJF-only type. In CCSM4 (Figure 3.10, right column), the thermal contrast difference remains negative throughout the year similar to observations, but a significant underestimation can be seen in moisture availability in spring and early summer (as compared to 3.10, left column). This demonstrates the lack of its ability to simulate anomalous SAM (as seen in spatial patterns previously).

In the JJAS-only type, the small positive anomalies of thickness difference in summer lag the rainfall anomalies (similar to that seen in WU12), indicating that the enhanced monsoon rainfall is due to thermal contrast. Surface air humidity anomalies are small corresponding to Indian Ocean negative SST anomalies (Figure 3.1) and contribute less to anomalous SAM than the SSTA does. In CAM4, the thickness difference becomes positive in late summer

instead of early summer, as seen in observations. The moisture content anomaly is near zero in early summer and becomes negative afterward. This is a probable source for the poor simulation of anomalous SAM rainfall. In CCSM4, the thickness difference is negative in spring and the accompanying moisture peaks at the same time. In summer the thickness difference becomes positive with a reduction in moisture. As seen in the spatial patterns (Figure 3.4, last column), the CCSM4 shows strong anomalous rainfall over SAM region in summer. This means that the CCSM4 atmospheric circulations have a larger contribution in modulating the intensity of anomalous rainfall than the thermal contrast does.

In the DJF&JJAS type, negative thickness difference anomalies appear in winter and spring and become positive after midsummer. Air humidity anomalies are quite large and positive in western Indian Ocean from winter to early summer. Positive SST anomalies during late spring and early summer, as shown in Fig. 3.8, induced an increase in surface air humidity and thus favor a stronger SAM rainfall (WU12). The thermal contrast makes a limited contribution to the SAM late summer anomalies. In CAM4, the moisture content and thickness difference are in-phase with observation and produce good simulations. In the late summer and early fall, the moisture persists due to the lower values of thickness difference whereas the observed moisture decreases sharply at that time. In CCSM4, the thickness difference and moisture content are almost in out of phase with maximum and minimum amplitude appearing in the early spring and in the summer, respectively. This is very different from the observations and CAM4.

3.3.4 Idealized Experiments

We now explore how the Indian Ocean controls the ENSO-SAM relationship with the help of CAM4 idealized experiments. As the role of the Indian Ocean in amplifying the anomalous SAM rainfall is significant in DJF&JJAS years, we focus only on this particular type. In the analyses discussed above, we have seen that the CAM4 performance is much better in DJF&JJAS type as compared to the DJF-only and JJAS-only type. This is another reason to conduct the idealized experiments for the DJF&JJAS type.

We performed two different ensemble experiments, namely CAM4_ENSO_IO and CAM4_ENSO, for the period from 1979 to 2009. In CAM4_ENSO_IO experiments, observed monthly SSTs are specified in both the Indian and Pacific Oceans whereas in CAM4_ENSO experiments, the observed SSTs are only prescribed over the Pacific Ocean. The annually repeating climatology SSTs, blended with observed SST, are used elsewhere in both experiments. The two experiments are designed to explore the role that the different oceans, including the Indian, Pacific, or other play in the anomalous SAM rainfall.

In Figure 3.11, composites of JJAS rainfall anomalies and 850 mb winds for the DJF&JJAS type are presented for CAM4_ENSO_IO and CAM4_ENSO experiments. The results for CAM4_ENSO_IO are similar to the CAM4 control simulation, shown in Figure 3.7, with some small scale refinements. This implies that the anomalous SAM is mainly influenced by Indian and Pacific Oceans only. In the CAM4_ENSO case, the absence of the Indian Ocean influence can be characterized by a significant removal of rainfall over the tropical Indian Ocean and Indian subcontinent. The persistence of positive northern Indian Ocean SST anomalies induced by the preceding winter east equatorial Pacific SST anomalies is absent in

this experiment, resulting in reduced anomalous rainfall. The weak contribution from concurrent negative east equatorial Pacific SST anomalies, via direct atmospheric circulation changes, can be seen in Figure 3.12 (spatial plots). Although the negative SST anomalies in the east equatorial Pacific induce lower level divergence and upper level convergence over the tropical Pacific, their effect on the SAM region is unrealistically confined to the Maritime continent only, further reducing the surface moisture and rainfall there. This can be also seen in the temporal evolution (Figure 3.12 (bottom plot)) of rainfall for both experiments. The rainfall in the CAM4_ENSO experiment is suppressed during the summer as compared to the CAM4_ENSO_IO rainfall. These results support the physical mechanisms of the DJF&JJAS type discussed in WU12. Also the importance of the Indian Ocean in modulating (amplifying or suppressing) the rainfall in ENSO-SAM teleconnection can be seen in this analysis.

3.4 Summary and Conclusions

This chapter presented a detailed investigation of the ENSO-SAM relationships in the CAM4 and CCSM4 models simulations. This investigation seeks to identify the strengths and weaknesses of these models in preserving different types of ENSO-SAM relationships. This analysis was performed following the recent work by Wu et al. (2012) where they identified three different types of ENSO influences on the SAM from analysis of observations. We have extended their analysis to our simulation results, and further explored the physical understanding of particular types of ENSO influences on SAM using sensitivity experiments.

Composite analysis was performed for both model simulations and observations including spatial composite map and temporal variability of the area average. The CAM4 simulation in the DJF-only type is better than CCSM4, and can reproduce the realistic anomalous rainfall

reasonably well over the east Pacific along with some biases over the western Pacific and Maritime continent that are particularly significant in the preceding winter and the early summer. It can also capture the realistic evolution and propagation of rainfall anomalies from their decay over the tropical Pacific in the preceding winter to their development phase over the Indian subcontinent in the late monsoon season. In contrast, the CCSM4 shows large systematic errors including significant rainfall anomaly biases in the Indian Ocean from the preceding winter to the early spring, probably due to the errors in the SST simulation. The CAM4 model performed better than CCSM4 in DJF-only years.

For the JJAS-only type where the concurrent eastern Pacific SST anomalies directly induce anomalous SAM through atmospheric circulation, the CAM4 simulations show disagreement in SAM rainfall anomalies between the observations and the CCSM4 simulations. It is found that ENSO induced warming in northern Indian Ocean via atmospheric circulation is absent in CAM4 simulations in the JJAS-only type probably due to the lack of air-sea coupling. The CCSM4 shows strong convergence over the SAM region, intensifying the anomalous SAM. The CCSM4 results are more realistic than CAM4 in comparison with observations. It is found that the atmospheric circulations of velocity potential and the corresponding divergent winds at 850 mb and 200 mb heights in CCSM4 contribute more than the thermal contrast in modulating the intensity of anomalous rainfall.

For the third type of DJF&JJAS, the impact of ENSO on the SAM is characterized by a switch of the ENSO phase during the cycle from the warm phase in preceding winter to cold phase in the summer, amplifying the SAM rainfall. In this type, CAM4 better reproduces the realistic anomalous rainfall than the CCSM4 which has very weak simulated rainfall anomalies. The convergence and divergence zones in the CAM4 model are comparable to the

observations whereas the CCSM4 has very weak simulations in these circulations. In comparing the other two simulation types, the CAM4 better models the ENSO-SAM relationship in the DJF&JJAS type, including the realistic simulation in moisture content and thickness difference. In contrast, the CCSM4 simulates the moisture content and thickness difference out of phase with realistic evolution.

The CAM4 sensitivity experiment highlights the role of the Indian Ocean in controlling the DJF&JJAS type ENSO-SAM teleconnections. It is found that in the absence of Indian Ocean SST, the anomalous SAM summer rainfall is suppressed in the DJF&JJAS type, suggesting that the important modulation by the Indian Ocean SST probably occurs through the preceding winter east equatorial Pacific SST forcing and the atmospheric circulations.

The results presented in this chapter suggest that model biases can significantly affect the ENSO-SAM relationship. Although the air-sea coupling is important for better SAM simulation and its relationship with ENSO, the bias in the ocean modeling can significantly degrade the SAM relationship. The fidelity of the CCSM4 model is most likely not at a level where the local air-sea feedbacks could be clearly shown to be an important component of the forecast system that improves the seasonal predictability of SAM. This study also suggests that the atmospheric model could be used as an alternative tool for monsoon predictions until the coupling biases are better resolved.

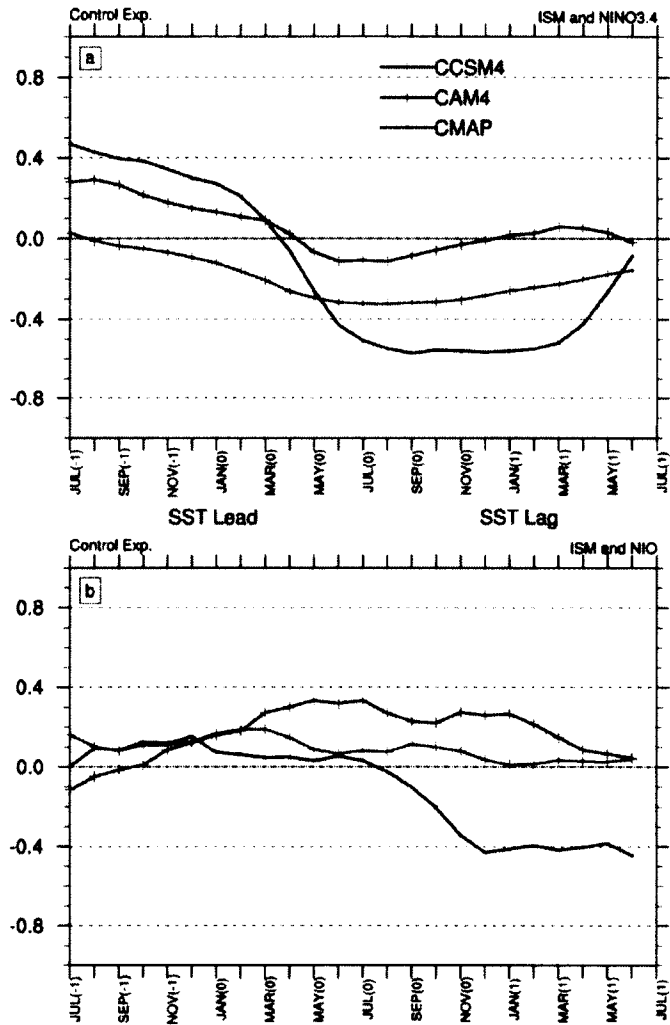


Figure 3.1: Lag lead correlation of monthly mean SAM precipitation with (a) Niño3.4 (-5°S - 5°N , 120° - 170°W) and (b) northern Indian Ocean (NIO, 5° - 25°N , 60° - 100°E) indices. Area averaged (5° - 25°N , 60° - 100°E) time series (ISM) of observed CMAP (solid black line) precipitation, CAM4 (solid blue line) and CCSM4 (solid red line) time series are correlated with observed Niño3.4 and northern Indian Ocean SST indices except for CCSM4 case where CCSM4 simulated SST are used. Month with a negative (positive) sign indicate that SST leads (lags) the ISR with maximum lead of 12 months (1 year). Month 0 and 12 indicates June whereas month 4 and 8 correspond to February and October (minus sign for previous month). Correlations are calculated using a 5 monthly sliding window.

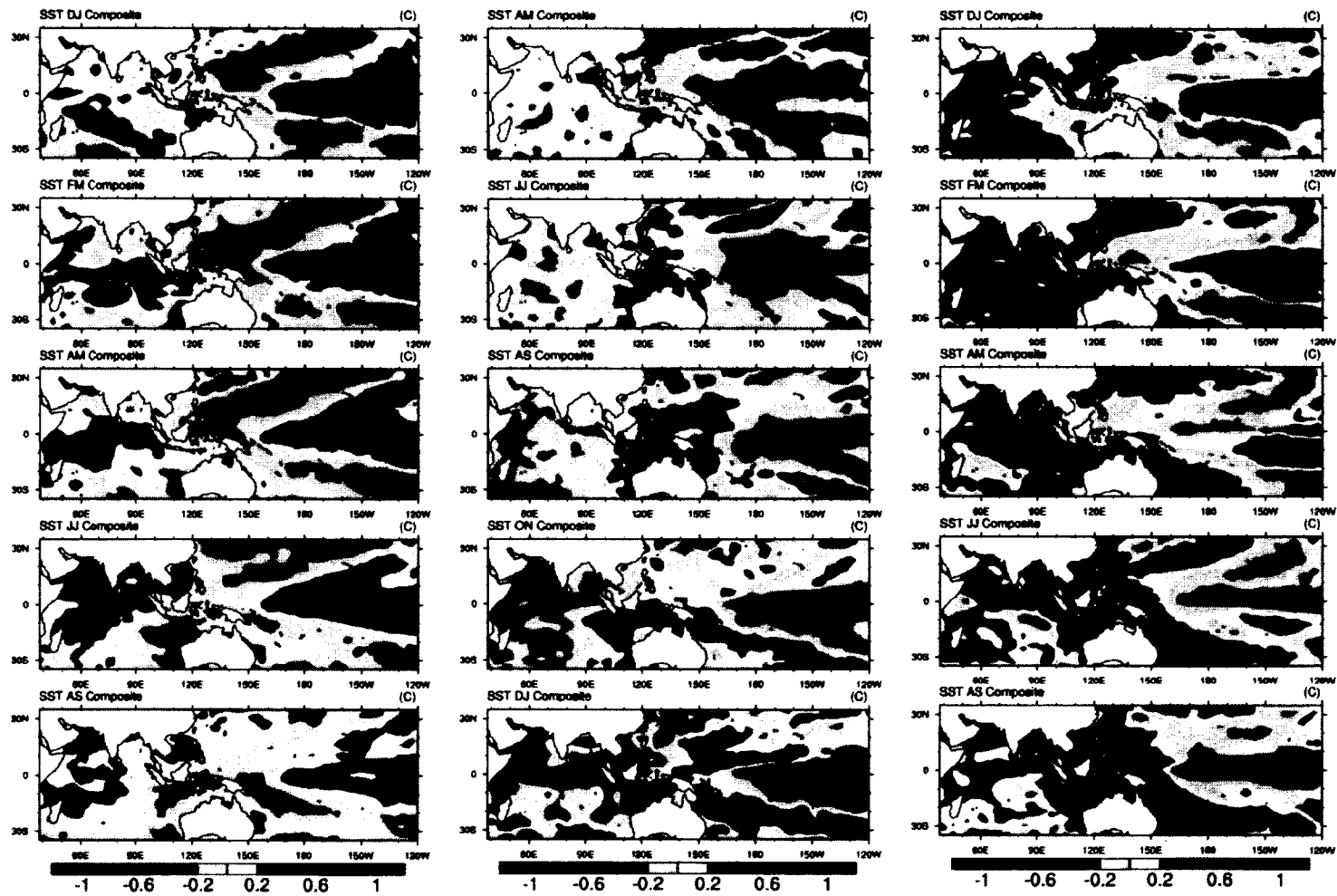


Figure 3.2: Bimonthly composite anomalies of observed SST (HadSST) for DJF, FM, AM, JJ, and AS (top to bottom). The 1st, 2nd and 3rd columns represent DJF-only, JJAS only and DJF&JJAS types respectively (see text for detail). Shading corresponds to the values in C.

S Islam: Ensemble Simulation and Forecasting of South Asian Monsoon

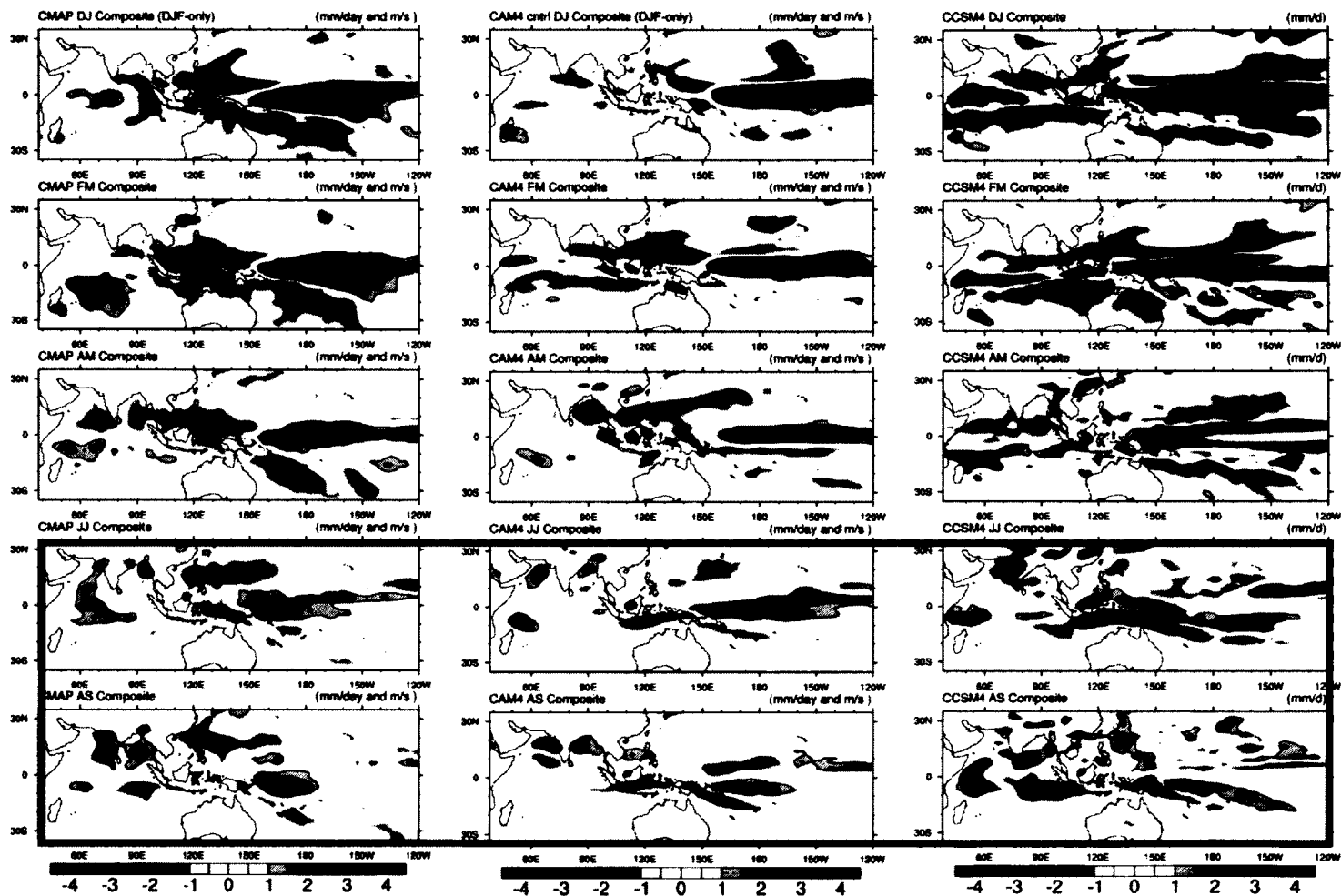


Figure 3.3: Bimonthly composite anomalies of precipitation for DJ, FM, AM, JJ, and AS in DJF-only type (top to bottom). The 1st, 2nd and 3rd columns represent observed (CMAP), CAM4 and CCSM4 respectively. Shading corresponds to the values in mm/day while the contour shows their significance.

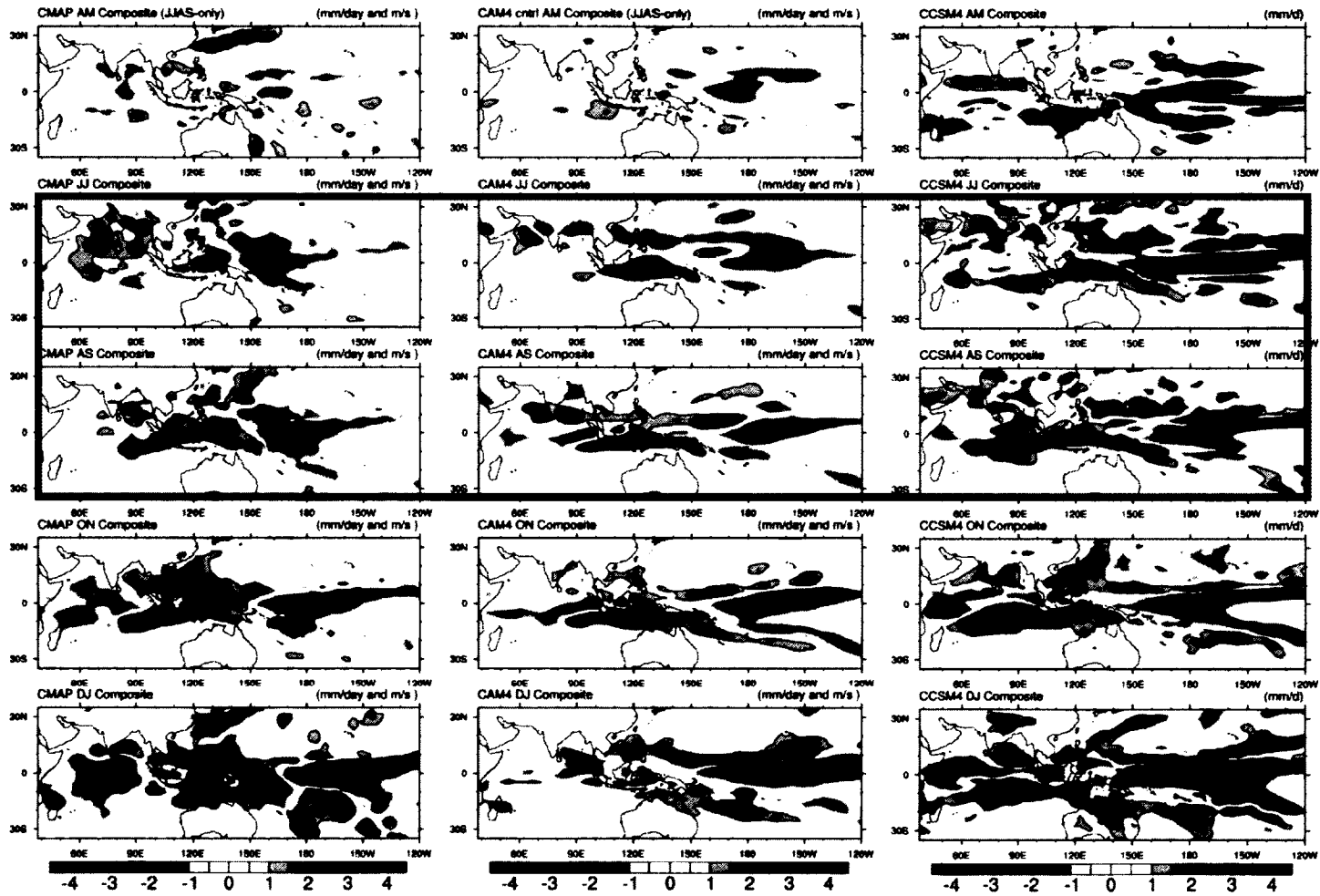


Figure 3.4: Same as Figure 3.3 but for the JJAS only type.

S Islam: Ensemble Simulation and Forecasting of South Asian Monsoon

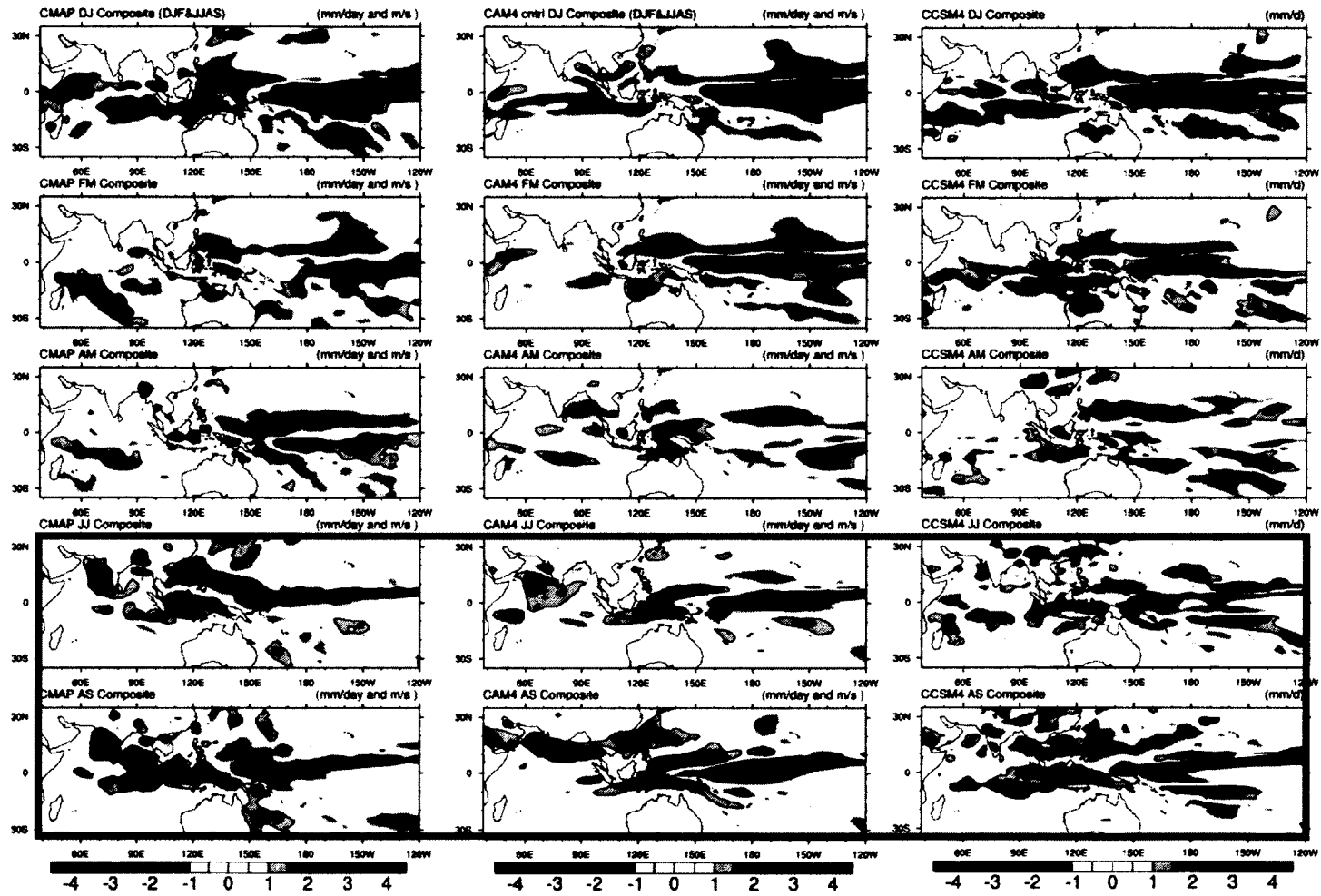


Figure 3.5: Same as Figure 3.3 but for the DJF&JJAS type.

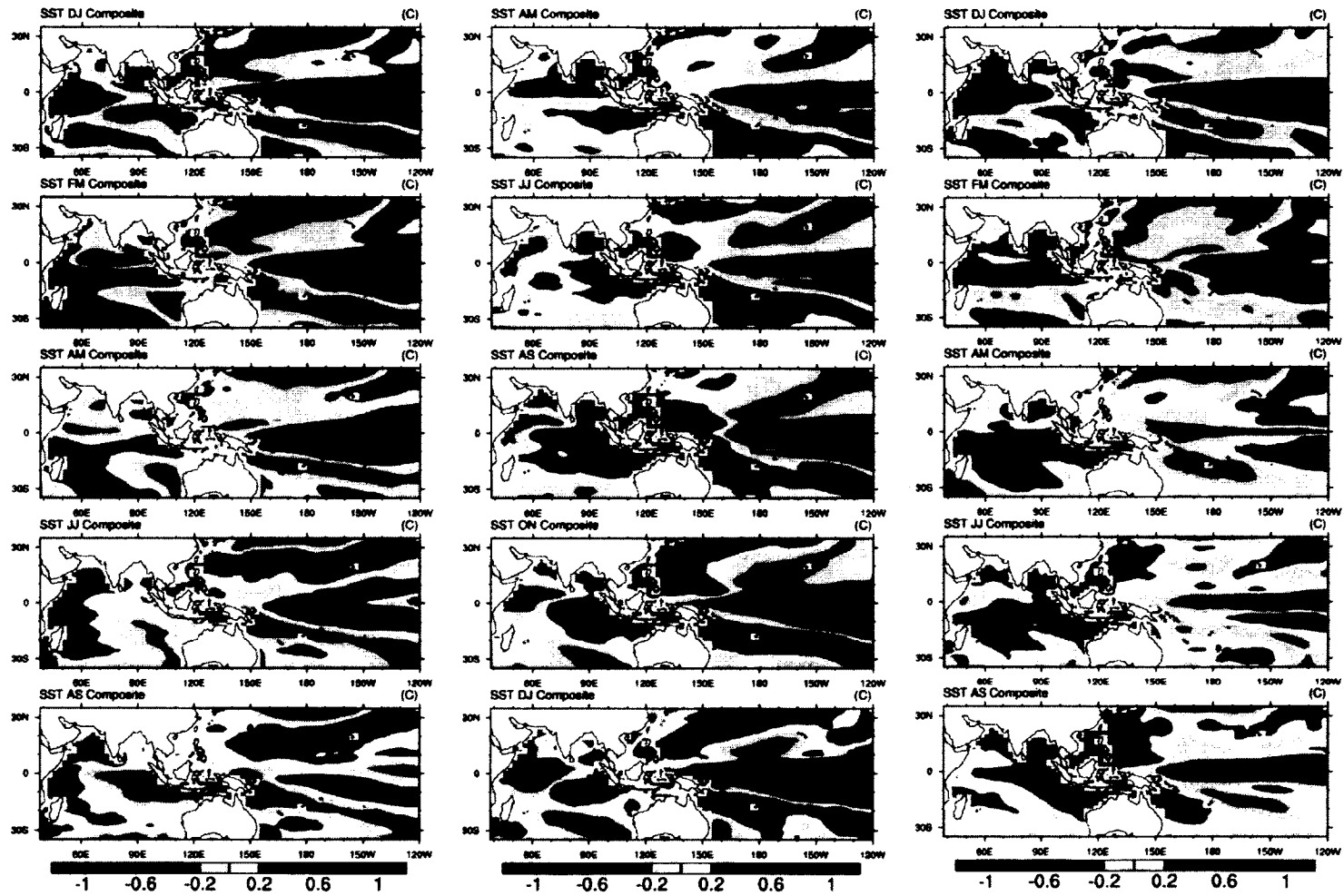


Figure 3.6: Same as Figure 3.2 but for CCSM4 simulated SST.

S Islam: Ensemble Simulation and Forecasting of South Asian Monsoon

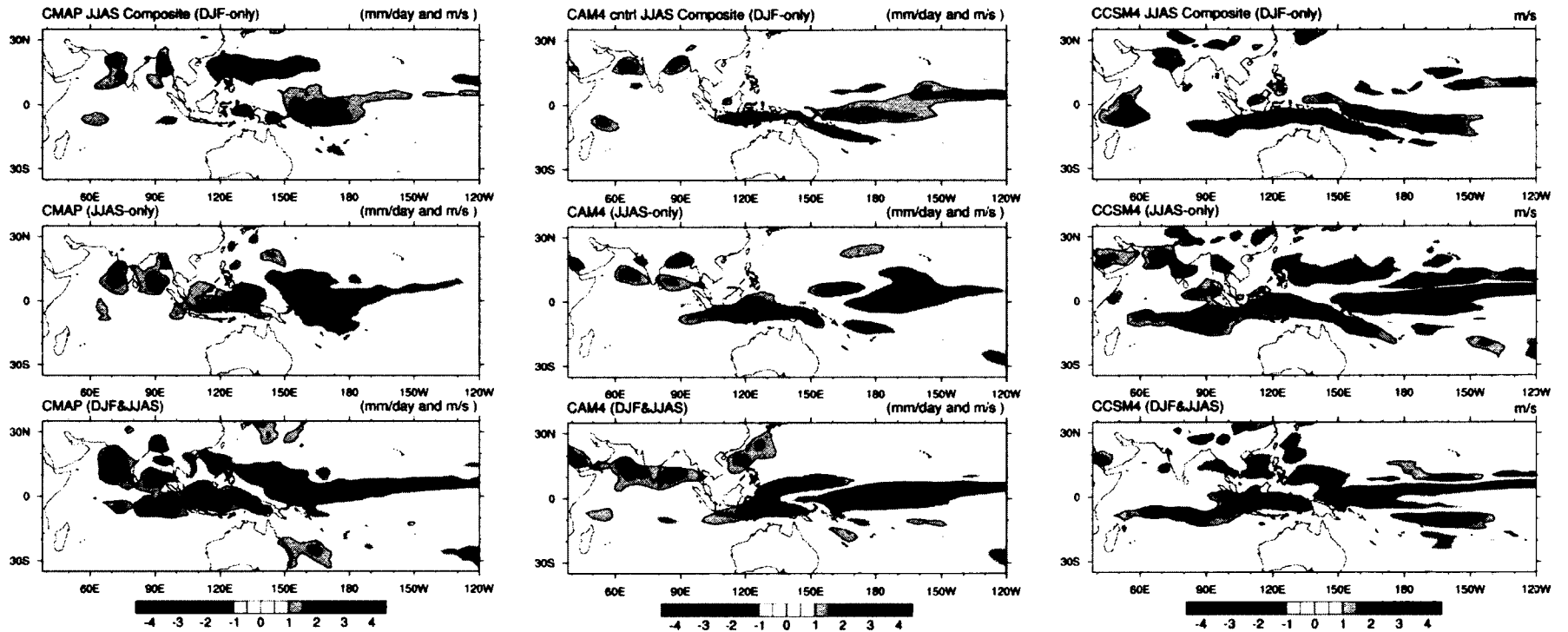


Figure 3.7: Composite JJAS rainfall anomalies (mm/day) for the DJF-only type, JJAS-only type and DJF&JJAS type based on observed (CMAP) and simulated (CAM4 and CCSM4) precipitation.

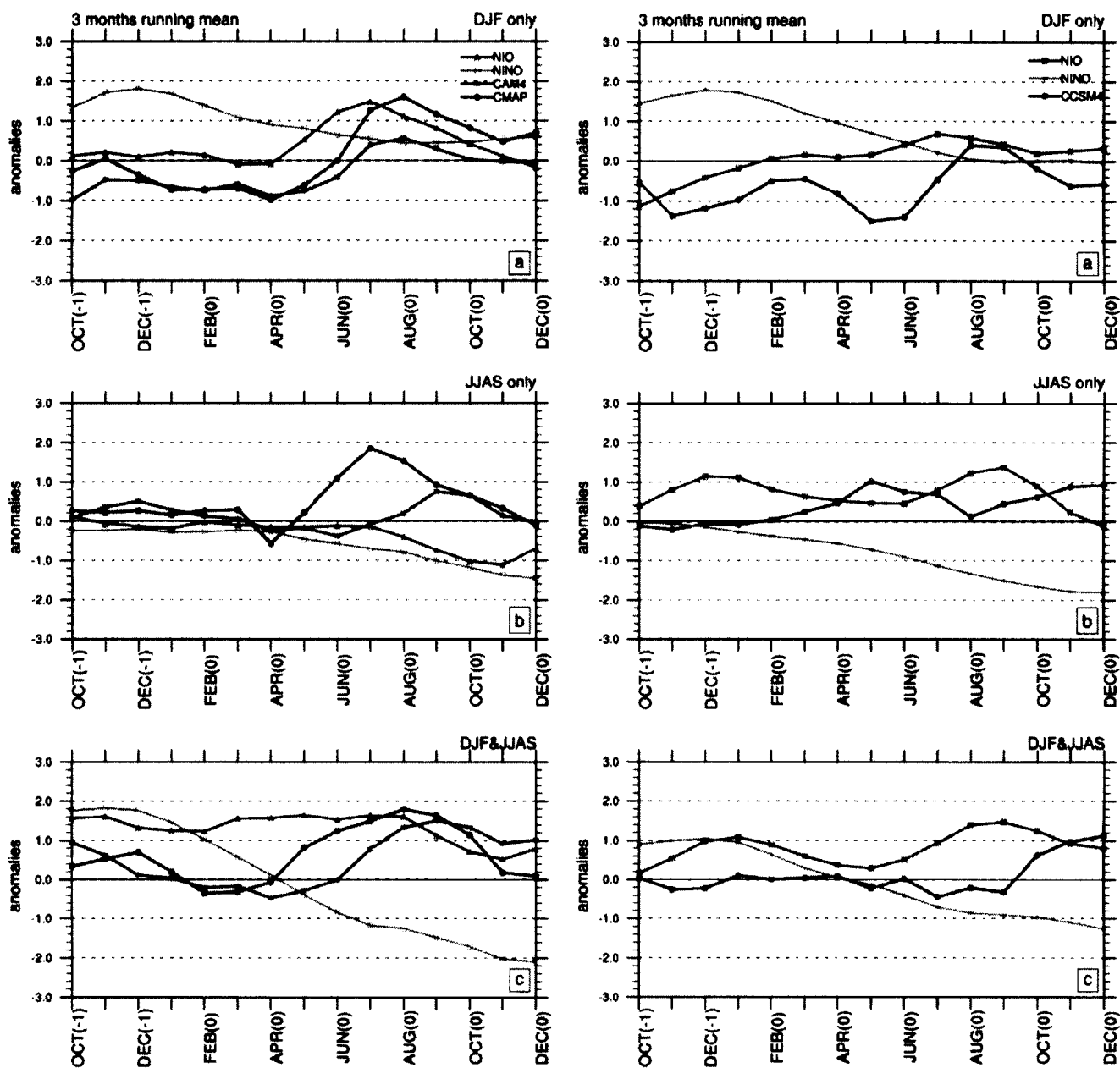


Figure 3.8: Area averaged composite of normalized 3-month running mean anomalies of Niño3.4 SST (green curves), northern Indian Ocean SST (NIO, red curves), CAM4 or CCSM4 precipitation (blue curves) and CMAP precipitation (IMR, black curves) in (a) DJF-only type, (b) JJAS-only type, and (c) DJF&JJAS type. SST curves in left column are from observation while right column SST curves are from CCSM4 simulation.

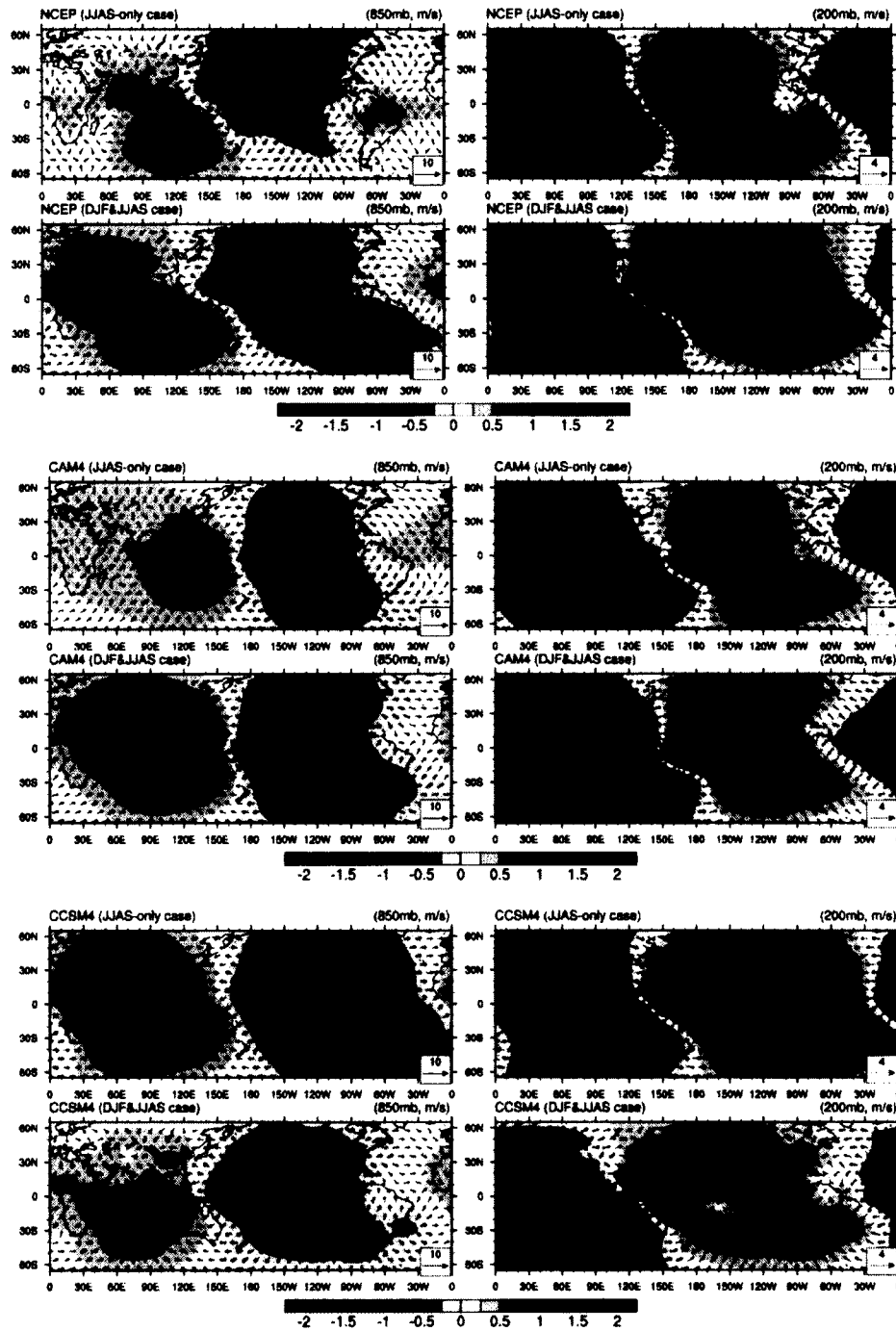


Figure 3.9: Observed (top), CAM4 (center) and CCSM4 (bottom) JJAS mean composite anomalies of velocity potential and the corresponding divergent winds at 850 mb height (left column) and at 200 mb height (right column) for the JJAS-only and DJF&JJAS types. Shading corresponds to the velocity potential in 10^6 s^{-1} and vectors in m/s.

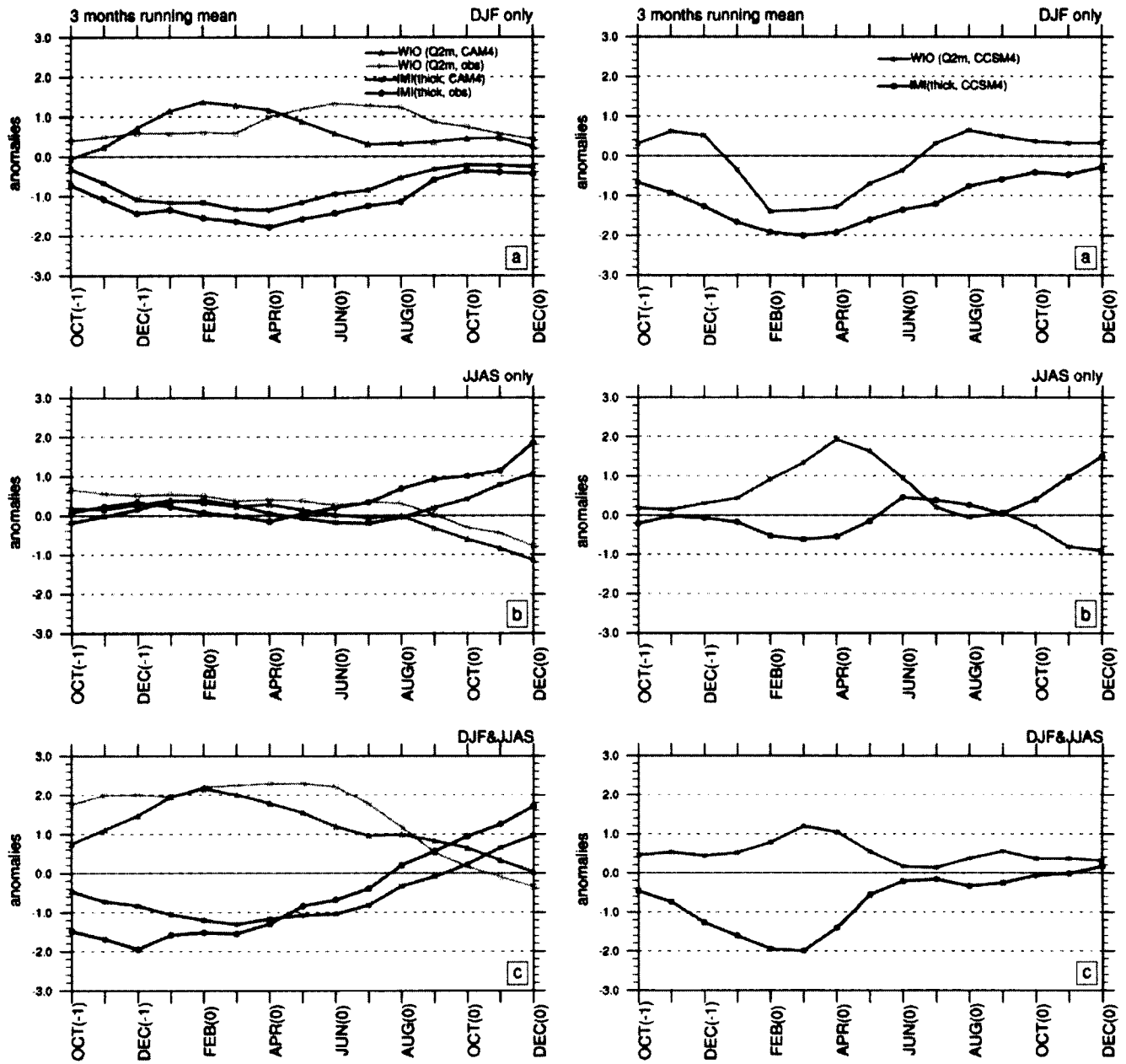


Figure 3.10: Composites of normalized 3-month running mean anomalies of surface (2 m) air humidity over the region of 0°–10°N and 50°–80°E (solid curves) and 500–200-hPa thickness difference (10 m) between area 20°–40°N, 50°–100°E and 08°–20°N, 50°–100°E in (a) DJF-only type, (b) JJAS-only type, and (c) DJF&JJAS type. Left column is for CAM4 and observation while right column shows CCSM4 simulated curves.

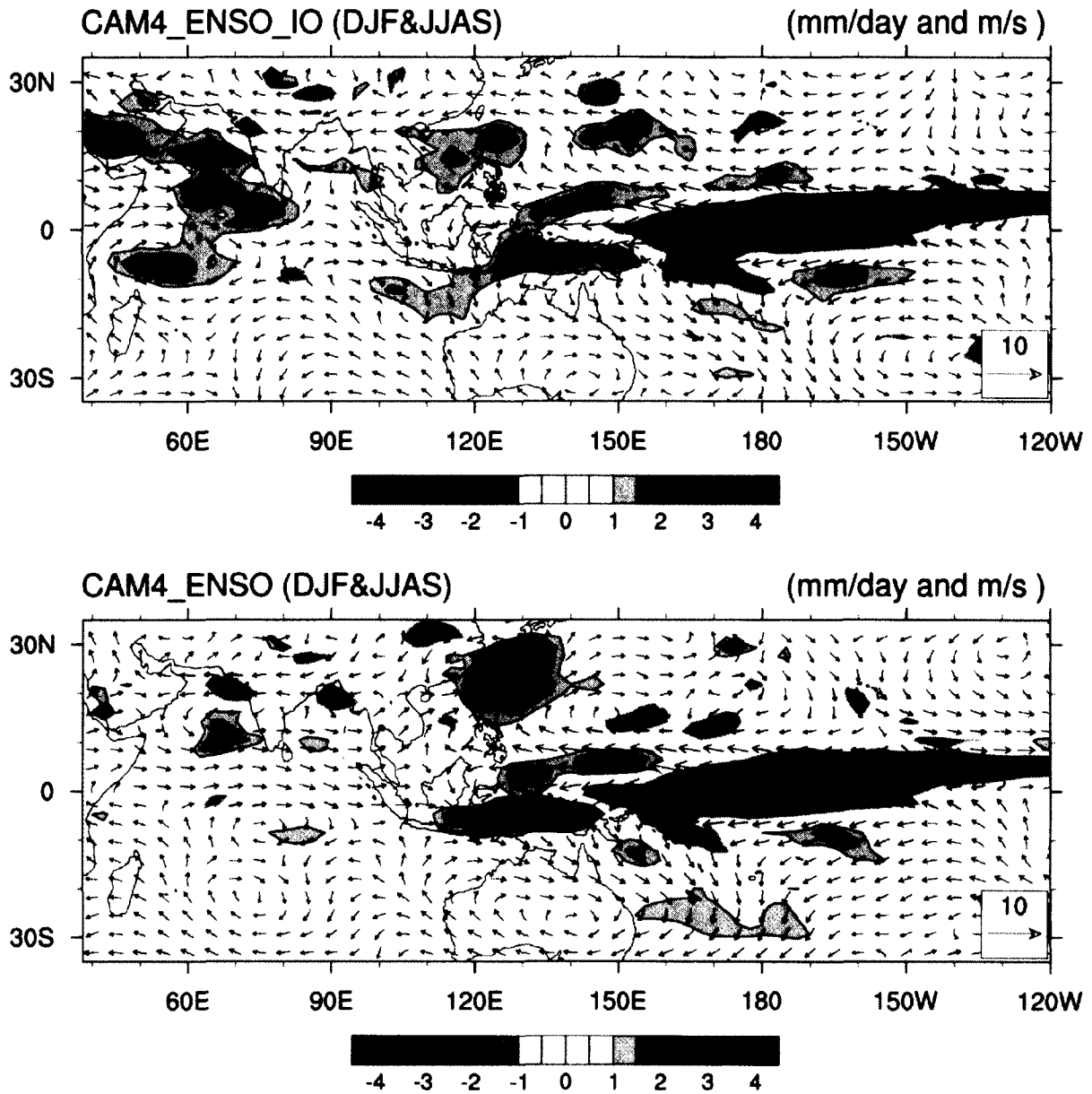


Figure 3.11: Composite JJAS rainfall anomalies (mm/day) and 850 mb winds for the DJF&JJAS type based on CAM4_ENSO_IO and CAM4_ENSO experiments. See text for detail of the experiments.

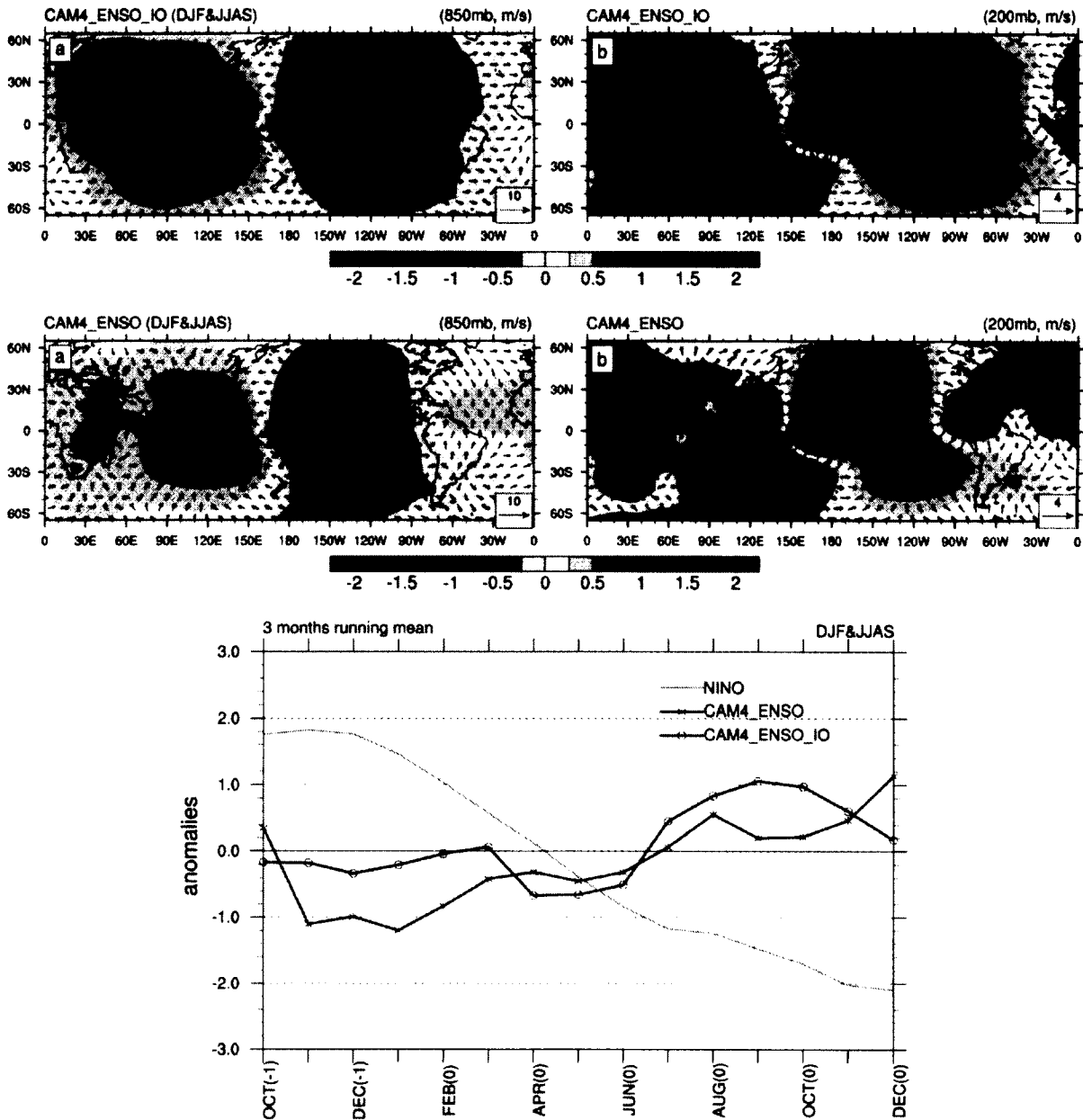


Figure 3.12: JJAS mean composite anomalies of velocity potential and the corresponding divergent winds at 850 mb height (top left) and at 200 mb (top right) for DJF&JJAS type based on CAM4_ENSO_IO and CAM4_ENSO experiments. (bottom) Composite of normalized 3-month running mean anomalies for CAM4_ENSO_IO and CAM4_ENSO experiments for DJF&JJAS type.

Chapter 4

Optimal error growth of South Asian Monsoon Forecast Associated with the uncertainties in the Sea Surface Temperature

Islam S, Y Tang and P Jackson (2015), Optimal error growth of South Asian Monsoon Forecast Associated with the uncertainties in the Sea Surface Temperature, submitted to Climate Dynamics Journal

This paper is reformatted to serve as Chapter 4 in the thesis.

4.1 Introduction

The chaotic nature of the atmospheric circulation imposes a deterministic limit on long-term weather forecasts (Lorenz 1963) but some large-scale atmospheric features such as ENSO are potentially predictable beyond this limit (Shukla 1981). This was initially indicated by GCM results which showed that a large part of the tropical variability is determined by slowly varying boundary conditions of SST, soil moisture and snow cover (Charney and Shukla 1981; Shukla 1998). Based on these indications, significant progress has been made over the past decades in understanding and predicting ENSO and large-scale tropical features associated with its variation. Although the correlation skill of ENSO forecasts have improved remarkably (Wang et al. 2009; Jin et al. 2008), seasonal prediction of other climatic features such as the Asian monsoon still needs substantial improvement.

Several attempts have been made for the forecast of the Asian monsoon particularly the South Asian Monsoon (SAM or Indian Monsoon hereafter). Many studies have shown that the current skill of Asian monsoon forecasts using dynamical models, is poor on the seasonal time scale (Wang et al. 2007, 2008; Drbohlav and Krishnamurthy, 2010; Chowdary et al. 2010; Sohn et al. 2012) as well as on the sub-seasonal time scale (Fu et al. 2009, 2011). Recent studies such as Acharya et al. (2011) and Kulkarni et al. (2012b) have also highlighted that the GCMs have limited skill in predicting SAM rainfall. Singh et al. 2012a has reported that GCMs have large biases in simulating the observed teleconnection pattern, which lower the skill of dynamical seasonal prediction. Beside dynamical models, many statistical models have shown inconsistent skill in predicting SAM rainfall (Gadgil et al. 2005).

In general, the lower SAM forecast skill is mainly due to our incomplete understanding of monsoon dynamics which lead to a poor formulation of model physics, large model biases (Islam et al. 2013) and the uncertainties involved in specifying the forecast initial states. This means that there is potential to increase SAM forecast skill with (i) better climate models having more accurate representation of intraseasonal variability and better parameterizations schemes and (ii) improved ensemble methodologies used in forecast initialization. Together (i) and (ii) can ensure improved SAM forecast skill.

Although climate models are continuously developing with time, improving forecast ensemble strategies remains a long-term challenge to advance SAM forecast. To make a reliable ensemble, it is important to explore the impact of uncertainties in initial conditions on SAM seasonal predictions. Among many initial uncertainties involved in monsoon forecast, the uncertainties in SST can greatly impact its forecast skill. It has been discussed in previous chapters that the essential source of SAM predictability at seasonal time scales mainly comes through the tropical SST forcings, especially ENSO (Sikka 1980; Shukla and Paolino 1983; Nigam 1994; Slingo and Annamalai 2000; Meehl and Arblaster 2002; Annamalai and Liu 2005). Along with its teleconnection with ENSO forcing, SAM has close interaction with SST in the tropical Indian Ocean (Wang et al. 2009; Chowdary et al. 2010; Kosaka et al. 2012). It is interesting to investigate how SST uncertainties impact SAM forecast error growth. This is important in its own right from the point of view of error dynamics. Additionally, a direct application of the uncertainties study is to construct the optimal ensemble.

It is well known that the ensemble mean has usually more reliable and greater skill than a single deterministic forecast (Leith 1974). The importance of ensemble forecast has been greatly acknowledged, with many approaches proposed and used to construct optimal

ensembles. These methods include Time Lag Ensemble, Bred Vectors, Singular Vectors and Ensemble Kalman filter etc. (e.g. Toth and Kalnay 1993, 1997; Molteni and Palmer 1993; Moore et al. 1996; Chen et al. 2004; Tang et al. 2006). However, these studies mainly focus on weather and medium range seasonal forecast on a global domain or ENSO relevant climate prediction. There is little research on how to construct the optimal ensemble for SAM seasonal prediction in the literature.

In this chapter, we use Singular Vector (hereafter named as SV) to explore the impact of initial SST uncertainty on SAM seasonal prediction and to construct the optimal ensemble. The SV is a widely used method in studying the optimal growth of initial perturbations. The aim of using SV is to find those perturbations, superimposed on a given initial state, which grow most rapidly under the assumption that the perturbations grow linearly in time. As the fast-growing mode of prediction error is often dominated by weather-scale instabilities in a full GCM, it is problematic to use the traditional SV method to characterize the fast-growing modes associated with long-term timescale variability i.e. at longer lead time. Therefore, when applying the SV method in GCMs to study climatologically relevant problems, particular care needs to be taken to filter out the fast-growing modes of weather instabilities (Kleeman et al. 2003).

This chapter focuses on the implementation of the climatically-relevant SV (hereafter named as CSV) method for SAM seasonal forecasts. The CSV method was introduced by Kleeman et al. 2003 which was later applied to realistic coupled models (Tang et al. 2006). It addresses the fast error growth due to climatically relevant instabilities by running an ensemble to average out the weather noise, thereby, filtering out the atmospheric noise but retaining the climatic response. This is especially important for seasonal climate forecasts. In addition, the

CSV is cost-efficient since it does not require tangent linear and adjoint models, which are expensive in computation and complicated in technique for a GCM (Tang et al. 2005). Previous studies have applied the CSV method to estimate CSVs for seasonal forecasting of SST in the Pacific Ocean such as ENSO or decadal forecasting of the North Atlantic Ocean (Hawkins and Sutton, 2010). It has not been used for SAM seasonal forecasts. This study is therefore the attempt to apply CSV to investigate the optimal error growth of SAM seasonal prediction due to uncertainties in SST, using a general circulation model. The overall motivation is to use CSV to explore the error dynamics of SAM forecast, and the optimal construction of SAM ensemble forecast.

The chapter is structured as follows. Section 4.2 discusses the CSV method and its implementation, the estimation of the linear operator R , model description and experimental setup and choice of variables. Section 4.3 highlights characteristic of leading CSVs and corresponding final patterns for the Indian and Pacific Oceans. Section 4.4 discusses validity of CSVs and its sensitivity to varying number of EOFs and ensemble members. Ensemble SAM forecasts, constructed using CSVs, are discussed in section 4.5. Section 4.6 is a brief summary and conclusion.

4.2 Method and Models

4.2.1 Estimation of Singular Vectors

As discussed in the previous section, this study utilizes the CSV method for extracting optimum perturbation patterns. The mathematical formulation of the CSV method, based on Kleeman et al. (2003) and Tang et al. (2006), is as follows:

A general dynamical system may be written compactly as

$$X(t) = F[X(t')] \quad (1)$$

where $X(t)$ is a vector representing the system state and F is a nonlinear operator. For a small perturbation Φ , Eq. (1) can be written as

$$X(t) + \Delta X(t) = F[X(t') + \Phi] \quad (2)$$

Subtracting Eq. (1) from Eq. (2), we have

$$\Delta X(t) = R\Phi \quad (3)$$

where the linear operator R in Eq. (3) is the first-order derivative of F with respect to X (at the time of t'). It is often called the propagator of Eq. (1) and gives the time evolution of the dynamical system by representing perturbation growth matrices.

The singular vectors of the system, which are the perturbations that amplify maximally over the time period $(t - t')$, are the eigenvectors (E) of $R^T R$ with the largest real part (e.g. Buizza and Palmer 1995), where R^T is the transpose of R . Thus the SV can be obtained by two methods: the eigenvector analysis of the $R^T R$ matrix or singular value decomposition (SVD) analysis of R . Mathematically it can be shown that:

$$R(t, t')E_1 = \lambda_1 S_1 \quad (4)$$

Where λ_1 represents first singular value and S_1 is first SV. Hence $\lambda_1 S_1$ can be derived by applying the propagator $R(t, t')$ to the initial pattern E_1 as shown by (4). $\lambda_1 S_1$ is called the final pattern. Here S_1 is the left vector of SVD of R . The calculation of R is discussed below.

4.2.2 Calculation of R and Application to the SAM Forecast System

For calculating R of the dynamical system (1), a perturbation variable (denoted by T_p) at the initial time and the target variable (denoted by A) used to measure forecast errors, are selected. By definition, the leading SV of A indicates what kind of uncertainty in T_p can lead to the fastest error growth for predicting A . The detailed procedure for obtaining R is similar to that described in Kleeman et al. (2003) and is summarized as:

1. An ensemble of 10 forecasts with lead time of 4 months (June, July, August and September, named as JJAS) is constructed by randomly perturbing the initial T_p field with 10 “very small” random patterns. The ensemble mean of A is denoted by $\overline{\Psi_0(t)}$.
2. Each of the leading three correlation EOF modes e_i of T_p ($i=1,2,3$) is added (with a multiplication factor of 0.1 to ensure linearity) to the initial condition described in step (1) and a new ensemble of 10 forecasts is produced. The corresponding ensemble mean of A is denoted by $\overline{\Psi_i(t)}$.
3. A reduced-state space matrix version r_{ij} of the propagator R is then obtained taking the difference of both the ensembles. Mathematically it can be represented as

$$Re_i = \overline{\Delta\Psi(t)} = \overline{\Psi_i(t)} - \overline{\Psi_0(t)} = \sum_{j=1}^3 r_{ij} e_j + residual \quad (5)$$

The residual in equation (5) is generally very small and can be ignored (Kleeman et al. 2003). The climatically relevant singular vectors are thus obtained by SVD analysis of R as aforementioned. These singular vectors are then projected back to real T_p space using the EOF basis vector expansion.

In implementing this method, it is important to note that ensemble experiments are carried out to filter the weather noise by averaging in order to extract fast error growth due to climatically relevant instabilities. Another advantage of the CSV method is that the choice of the analysis domain and optimization lead time can be made after the ensembles have been completed which allows one to explore the sensitivity to different choices without further model experiments.

4.2.3 Experimental Setups

The models used in our seasonal forecast system are CAM4 and CCSM4. The ability of CAM4 and CCSM4 to simulate the summer monsoon has been explored in Chapter 2 and 3. It is found that CAM4 overestimates the monsoon rainfall over most of the SAM region when compared to observation and CCSM4. The overall simulations of CAM4 reasonably captured the monsoon mean climatology (Islam et al. 2013), allowing its use to study predictability.

As discussed above, to implement the CSV method, three leading modes of the correlation EOF are used to perturb the initial conditions. Figure 4.1a and 4.1b show the first three correlation EOF modes for SST over the Indian and Pacific Oceans. The major reason for SV analysis over the two Ocean domains is to explore the individual effect of the Indian and

Pacific Ocean on the error growth of SAM, respectively. As reported in many studies, both of these Oceans can significantly affect SAM and play a key role in SAM variability (e.g. Meehl and Arblaster 2002; Annamalai and Liu 2005; Wang et al. 2009; Chowdary et al. 2010; Kosaka et al. 2012). Leading EOFs are calculated for the month of June using the observed SST data (Hadley Centre SST, Rayner et al. 2003) for the period 1980-2009. In case of the Indian Ocean (Figure 4.1a), 1st and 2nd leading EOF mode account for 39% and 12% of the total variance. EOF1 shows the Indian Ocean Basin (IOB) Mode and EOF2 depicts the east-west Indian Ocean dipole (Saji et al. 1999, IOD) mode. The former is closely linked to ENSO, whereas the latter occurs with and without ENSO (Pokhrel et al. 2012). The two modes differ not only in spatial structure, but also in their seasonal dependency. In Figure 4.1b, the 1st leading EOF over the Pacific domain represents the ENSO mode. The leading mode shows 30.7% explained variance over the Pacific Ocean. The spatial pattern associated with the warm phase of ENSO consists of positive SST anomalies across the eastern equatorial Pacific Ocean and weaker negative anomalies over the western tropical Pacific. In our CSV implementation, each of these EOFs is used as a perturbation added to the initial SST state.

Using the procedure mentioned in section 4.2.2, for each initial condition, eq. (5) can be evaluated by averaging 10 different ensemble members. The initial conditions used in experiments are from NCAR's Data Assimilation Research Tool (DART) system (Anderson et al. 2009). DART employs an Ensemble Kalman Filter (Houtekamer et al. 2005) which nudges the underlying models toward a state that is more consistent with information from a set of observations. Overall, these initial conditions are quite close to the National Center for Environmental Prediction (NCEP) reanalysis data sets, but are more consistent with the

CAM4 model. In coupled model experiments (i.e. CCSM4), the atmospheric (CAM4) and land (CLM4) counterparts are initialized using the same initial conditions as used in CAM4 initialization. To generate initial condition for ocean (POP2.2) and sea ice (CICE4) models, a multi years ocean control hindcast experiment is performed using the CORE II (Coordinated Ocean-ice Reference Experiments - Phase II, Griffies et al. 2012) input data set as boundary conditions. The CSV implementation for CCSM4 model is the same as discussed for the CAM4 model. The three leading EOF patterns in this case are calculated using the CCSM4 simulated SST instead of observations. In most of our analysis, we mainly focus on CAM4 simulations (uncoupled) and its analysis. The results from the coupled model are only used for the purpose of comparison between uncoupled and coupled CSVs.

The experiments are performed for the time period of 2000 to 2009 using DART initial conditions. Starting on June 1st of each year, 4-month (lead time) integration is made by initializing both atmospheric and land models (embedded in CAM4) at the same time. In the CAM4 forecast, boundary forcing such as SST (Hadley Centre SST, Rayner et al. 2003) and the May sea ice anomaly (one month prior to the forecast initialization time) is kept persistent over the entire forecast period, i.e. June, July, August and September. Figure 4.2 displays May SST anomalies from 2000 to 2009. It can be seen that they vary each year, which can influence the growth of forecast error when perturbations are applied.

To get a more robust statistical analysis, another set of ensemble forecasts is performed for the 1980 to 2009 time period using persistent SST anomalies as boundary forcing. The initial conditions in this case are from CAM4 control run forced with observed SST. The CSV method is implemented in the same way as in the simulations using DART initial conditions.

A summary of all the experiments using different domains, models, time periods, number of EOFs and ensemble size is given in Table 1.

4.2.4 Target Variable

In this study, the forecast variable is chosen to be Outgoing Longwave Radiation (OLR) and optimum interval (i.e. lead time) is 4 months. The use of OLR, instead of precipitation, is because it is comparatively better predicted than actual precipitation. On the other hand, it has been widely used to estimate SAM precipitation often as an index related to convective activity as lower OLR values are associated with higher cloud top heights in well-developed clouds (Schmetz; Liu, 1988 Kousky and Kayano, 1994; Moron, 1995).

In summary, we use SST as perturbation variable (T_p) at the time $t = 0$ and investigate OLR as target variable (A) at $t = t'$. As discussed before, the main reason to select SST as perturbation variable, over the Indian and Pacific Oceans, is due to the fact that SAM variability, at the seasonal time scale, is strongly influenced by the SST in central Pacific and Indian Ocean.

4.3 The Optimal Error due to the SST Uncertainties in Indian and Pacific Oceans

The precipitation over the SAM region in CAM4 simulation is validated in Islam et al. (2013) and it is found that CAM4 can capture the main climatological features of the SAM summer precipitation. Figure 4.3 shows the 30-year (1980-2009) mean OLR climatology from NCEP reanalysis data (left column) and CAM4 control simulation (right column).

Generally, negative (positive) values of OLR indicate more (less) convection and hence more (less) cloud coverage. In observations, for all four monsoon months, there is a widespread area of heavy convection around the northern Indian Ocean and Indian subcontinent reflecting heavier rainfall. In contrast, most of the equatorial Indian Ocean has higher OLR values showing less convection. In CAM4, these observed OLR features are well captured except in some regions such as suppressed rainfall over the Southern China Sea and excessive rainfall over the western Arabian Sea. Overall, the OLR simulated by CAM4 compares well with the observed OLR climatology.

4.3.1 Results during the 2000 – 2009 Period

We now examine how error growth varies with different initial conditions and lead time under different scenarios. In our CSV analysis, the first singular value is significantly larger than the remaining singular values. We therefore only discuss the leading CSV and its optimum growth i.e. the final pattern (FP hereafter) throughout the text. Over the Indian Ocean, the leading CSVs and corresponding FPs, optimized for time interval of 4 months (lead of 3 months), are shown in Figure 4.4 for each individual forecast during 2000 to 2009. In case of leading optimized perturbation (i.e. CSV), a distinct north-south dipole pattern can be identified in most of the years (while ignoring the arbitrary sign of CSVs). In the years having the dipole-like CSV pattern, the corresponding FP shows error growth mainly over most of the Indian Ocean particularly over the north Indian Ocean and the central Indian subcontinent. Although most of the CSVs in individual years are similar, the FPs are quite different in each year. Large variation of OLR FPs within different years could be due to the low-frequency processes causing asymmetry between the responses of OLR to the SST. This could be also due to the different initial SST state anomalies which may significantly change

the CSV growth. Indeed these SST anomalies, as the background state, play a crucial role in modifying the OLR spatial variation. This can be seen in some observed summer OLR anomalies over the SAM region for different years. For example, Charabi and Abdul-Wahab (2009) found that the July anomaly of OLR in ENSO years such as 2000 and 2002 are significantly different compared to other years. They have seen that the geographical variations of OLR anomalies are positive in the west Indian Ocean and negative in the East Indian Ocean in 2000 and 2002 whereas the patterns for years such as 1997 (strong El Niño year) and 1994 (strong IOD year) are the opposite.

To extract the general characteristic of these CSVs and FPs, we perform the EOF analysis for the 10 individual years for each lead time. The first leading EOF mode of CSVs (left column) and FPs (right column) is shown for all lead times in Figure 4.5. As can be seen, the CSV patterns now more prominently resemble the dipole structure, which is not dependent on the lead time if the arbitrary sign is ignored. The FP has differences for different lead times, due to the impact of initial stated on perturbation growth as discussed before. During the 4-month optimization interval, the error growth gets concentrated over the northern Indian Ocean and Indian subcontinent. Therefore the maximum perturbation growth is over those areas which are usually used to measure SAM intensity and variability i.e. the northern Indian Ocean and Indian subcontinent.

We now discuss the Pacific Ocean case, where CSVs are extracted over the ENSO region and the prediction target is still the OLR of SAM region. The results show that the CSVs are not sensitive to the initial conditions as in the Indian Ocean case, although the FPs vary significantly (not shown here). Figure 4.6 shows the leading EOFs of CSVs and FPs for all initial conditions at different lead times. A prominent structure in CSVs is the equatorial

ENSO-like mode, representing a large-scale structure with major weighting in the equatorial eastern Pacific and less weighting in the western Pacific. The CSVs in this case are similar to SVs analyzed in many intermediate models when targeting ENSO forecasts (e.g. Chen et al. 1997). This resemblance indicates the link between the error growth of ENSO prediction and that of SAM, suggesting ENSO as a major source of SAM predictability. The FPs (Figure 4.6) in the Pacific Ocean case have close similarities to the FPs calculated in the Indian Ocean case (Figure 4.5) except in some regions.

The above CSV analysis considers the individual impact of the Indian and Pacific Oceans on the error growth of SAM prediction where the Indian and Pacific Oceans are perturbed separately. We will next explore the total impact of the two Oceans on the error growth of SAM prediction. For this purpose, we analyze CSVs for the Indian-Pacific Ocean. In this case, the spatial structure of CSVs over the Indian and Pacific Oceans are the same as seen in the individual oceans case (not shown here). Figure 4.7 shows the leading EOF computed using 10 individual FPs from all years for each lead time. The interesting outcome from the joint analysis of the two oceans is the damped error growth over most of the Indian subcontinent and the Indian Ocean. The SST uncertainties from two different oceans partially cancel their growth with increasing lead time. This means that domain size choice is crucial, as uncertainties over a large region can suppress its growth and contribute less in error optimization. This was also confirmed by running an ensemble forecast using the CSVs over the whole Indian and Pacific Oceans which shows lower skill compared to the forecast perturbed with CSVs over Indian Ocean only. We will discuss the SAM ensemble forecast later.

The above discussion of error growth can be further investigated by analyzing singular values of CSVs over the Indian Ocean and over the Pacific Ocean. These values measure the fastest growth rate of perturbation during an optimum interval. The annual variation of singular values is shown in Figure 4.8 for the Indian (Figure 4.8a) and Pacific (Figure 4.8b) Oceans. The singular values of all the lead times are averaged each year to show an overall error growth. In case of the Indian Ocean only, the average singular values are higher than those of the Pacific Ocean. In Figure 4.8d, the lead time dependence of singular values is shown by averaging all the individual years. The gradual increase of singular values from lead times of 0 to lead times of 3 months is more prominent in the Indian Ocean case (black line) compared to the Pacific Ocean case (red line).

4.3.2 Results during the 1980 – 2009 Period

Due to the availability of DART initial conditions, based on real observation, we only used 10 years (2000-2009) of independent experiments in section 4.3.1. For more rigorous statistics, in this section we extend the CSV experiment to the period 1980 to 2009 (30 individual SAM summer forecasts, IO30 hereafter), however the initial conditions in this case are not from real observation. All settings in this experiment are the same as those of 10-yr previous analyses except the initial conditions, which were produced from the control simulation of CAM4 forced by observed SST. As mentioned in the singular values discussion in section 4.3.1, the Indian Ocean has a more significant impact on the SAM seasonal prediction than the Pacific Ocean. We therefore emphasize results only over the Indian Ocean in further analyses. For simplicity, we only focus on analysis at the seasonal time scale (i.e. 3-month lead time).

The leading EOF mode obtained using the 30 individual CSVs and FPs is shown in Figure 4.9 at a lead time of 3 months. The spatial structures of CSV found in IO30 experiment are very similar to CSVs found in the 10-year analysis (Figure 4.5) confirming the robustness of CSVs obtained in the analysis of section 4.3.1. The FP has some regional differences along with significant year to year variation (not shown here) mainly due to the impact of initial state superimposed by CSV as discussed in section 4.3.1. The annual variation of IO30 singular values (Figure 4.8c) and its lead time variation (Figure 4.8d, blue line) are quite consistent in magnitude with the 10-year CSV values.

It has also been found in previous studies that the SVs are insensitive to initial conditions in many models (e.g. Chen et al. 1997; Xue et al. 1997a; Zhou et al. 2007; Cheng et al. 2009). To explore the sensitivity of CSVs to initial conditions, we computed the spatial correlation between the EOF_c and each individual CSV pattern, as in Tang and Deng (2011), where the EOF_c is the first EOF mode obtained by all CSVs.

If the EOF_c and the CSV_i are denoted by the normalized one-dimensional vectors eof_c and csv_i , respectively, the spatial correlation R_{sp} is calculated as below,

$$R'_{sp} = \frac{1}{NG-1} \sum_{G=1}^{NG} eof_c(G) * csv_i(G) \quad (6)$$

where NG is the number of total model grids over the model domain and $i = 1, 2, \dots, 10$. The spatial correlation values are calculated for Indian Ocean and Pacific Ocean cases for each individual year and are shown in Figure 4.10 (a and b). For most years, the value of the spatial correlation coefficient is quite high, for both Indian Ocean (Figure 4.10a) and Pacific

Ocean (Figure 4.10b) cases. As mentioned in Cai et al. 2003, the positive phase of the same pattern should be regarded as equivalent to the negative phase, at least from a linear system perspective. In addition, the pattern sign can be arbitrary from the view of EOF analysis. Thus, the preliminary features of CSVs, as represented by the first EOF mode (equivalent to the average), are insensitive to initial conditions. This conclusion is further confirmed by using CSVs from the IO30 experiment by increasing the individual years to 30 i.e. $i = 1, 2, \dots, 30$ as shown in Figure 4.10c. Higher values of individual correlations indicate independence of the CSVs from initial conditions.

4.3.3 The Results from the Coupled Model CCSM4

The CSVs and FPs discussed above are based on atmospheric model simulation with persistent SST boundary conditions. How do the CSVs change in a coupled model? As argued in the introduction, the air-sea interaction plays a crucial role in SAM simulation and prediction. To explore this issue, we calculate the CSVs for CCSM4. The leading CSVs and FPs of CCSM4 over the Indian Ocean for all lead times are shown in Figure 4.11. We only show one particular year here, i.e. 2000, as the CSVs for other years are similar. Interestingly, the spatial structure of the CCSM4 CSVs is similar to CAM4 CSVs, but the growth rate shown in Figure 4.11 has differences with the CAM4 counterpart in Figure 4.8. The growth rate of CCSM4 varies more significantly with lead times than that of CAM4, so that the former is larger than the latter for longer lead time beyond 2 months. This suggests that the air-sea coupling could act as an amplifier by positive feedbacks to strengthen the perturbation growth for a long lead time. Due to the difference in the growth rate, the CCSM4 show stronger anomalies than CAM4 in their FPs, as evidenced in Figure 4.11 and Figure 4.8.

The similarities of CSVs between CAM4 and CCSM4 suggest that one may be able to use the CAM4 to construct an ensemble prediction for the CCSM4, which is more computationally efficient and has potential in operational forecast.

4.4 Sensitivity Experiments of CSV to some Parameters

Before using CSVs to construct ensemble forecasts, it is necessary to evaluate CSV robustness to the various choices made in the implementation of the methodology. In this section we therefore discuss the robustness of CSVs to the number of EOFs used as initial perturbations, and the number of ensemble members used in calculating means over the Indian Ocean with help of sensitivity experiments.

4.4.1 Convergence of CSV with Number of EOFs

As discussed in previous sections, the first three EOF modes are used to generate the CSVs. In the sensitivity experiment, we explore the CSVs with the number of EOFs used for initial perturbations. For simplicity, we randomly choose an initial condition of an individual year for the sensitivity analysis. Figure 4.12 shows CSVs computed using different numbers of EOFs. The lead time for CSV is 4 months. As we increase the number of EOF perturbations from 3 to 10 EOFs, the CSV structure does not change significantly. The corresponding FP gets optimized even with a relatively small number of EOFs i.e. 3 to 5 EOFs. This suggests that the dominant features of the CSVs can be captured by the leading 3 EOF modes. Indeed, increasing the number of EOF perturbations means including more noise in the initial conditions which can, beyond a certain limit, start degrading the optimization of perturbation. This analysis suggests that our choice of using the three leading SST EOFs in construction of CSVs is appropriate. We repeated the same procedure for other years with similar results.

4.4.2 Convergence of CSV with Number of Ensemble Members

Figure 4.13 shows how the first singular value changes for different numbers of ensemble members, when using three EOFs as perturbations. If only 10 ensemble members are used, singular values converge to its minimum values for lead time 3 months and for all individual years (colored lines). Beyond 10 to 15 ensemble members, the singular values remain quite similar. This means that the true mean can be estimated with the use of only 10 ensemble members. A similar convergence is seen for CSV spatial patterns suggesting the use of 10 ensemble members being reliable for their calculation (not shown here).

4.4.3 Validity of CSV

The CSVs and FPs, shown in Figure 4.4, are obtained by a linear approximation approach for the nonlinear model CAM4. It is therefore important to inspect whether the CSVs can resembled results that are directly obtained by the nonlinear model. This validation can be conducted by integrating the CAM4 twice, one from the initial condition superimposed by the CSVs (scaled by using a multiplication factor of 0.1), and the other from the initial condition only. The difference between two integrations, denoted as D_{non} , indicates the perturbation growth of the CSVs obtained directly by the nonlinear model, which can be compared with the FPs and serves as the purpose of the validation. We conduct this experiment for each year during the period from 2000 to 2009. Figure 4.14a shows the leading EOF of D_{non} over the entire period at 3 months lead time. The leading EOF pattern of the FP directly from the CSV method, i.e. applying the propagator R to the CSVs, is also shown in Figure 4.14b for comparison. It can be seen that the leading EOF of D_{non} (Figure 4.14a) is very similar to the FP from the linear approximation (Figure 4.14b) although there

are some discrepancies. Despite these discrepancies, the overall features very resemble each other, indicating that the estimates of the CSVs are robust and correct.

4.5 SAM Ensemble Forecast using CSVs

In the previous sections, we mainly focused on the general characteristics and validation of CSV and the FP. We now apply the CSVs to generate ensemble predictions. It is expected that such an ensemble prediction should be optimal and more skillful than single predictions and non-optimal ensemble predictions. For comparison, we also use the Time Lag Ensemble (TLE) method to construct ensemble predictions. The TLE is achieved using different initial conditions with the lag of six hours to initialize six forecasts, starting at 1st June of each year.

We construct ensemble predictions by the CSVs extracted over the Indian Oceans. Each individual CSV is multiplied by random noise and is superimposed onto the initial conditions to generate an ensemble forecast. The ensemble size is 20, by using different random numbers. In practice, we use 10 random numbers multiplied by a positive CSV and 10 random number multiplied by a negative CSV, since the sign of CSVs are arbitrary. The ensemble mean of positive and negative ensembles is labeled as CSV_p and CSV_n in discussions below, respectively.

The ensemble prediction is run for the period from 2000 to 2009 and from 1980 to 2009, respectively. The RMSE values from the period from 2000 to 2009 are shown in Figure 4.15a, for a single control run prediction without perturbation (black line), the ensemble of CSV_p and CSV_n (blue and red line), and ensemble of TLE (green line). For each forecast, an error bar is drawn using the bootstrap method (Efron et al. 1993) for its significance. The bootstrap

method is obtained as follows. i) At a given forecast lead month, the observation and forecast are paired together, based on same target month. In this way, the forecast and observation sampled are paired together for the whole period (2000-2009). ii) The 95% of the paired sample is then chosen randomly and used for RMSE calculation. iii) The step (ii) is repeated 1000 times to obtain 1000 RMSE. iv) The standard deviation of these 1000 correlation coefficients at each lead month is drawn as an error bar.

As shown in Figure 4.15a, the ensemble mean RMSE of CSV_p and CSV_n forecasts are significantly better than the Control and TLE forecasts at lead times beyond 2 months. The probable reason for the significant difference in the last two months is that the CSV used to construct ensemble prediction is based on the analysis of an optimal interval of 4 months. In other words, it is due to the fact that the CSVs used for perturbation are optimized for a four month period (i.e. from June to September each year).

To investigate the significance on a larger sample size, we also perform 30-year forecasts (CSV_{30p}) from 1980 to 2009 using the CSVs extracted from the IO30 experiment. This forecast is compared against IO30 control forecast and RMSE is shown in Figure 4.15b. The bootstrap methodology is repeated for IO30 forecasts, the same as for the 10-year forecasts. The improvement in RMSE for lead time 3 and 4 is significant in this case which increase our confidence in the reliability of RMSE results found for 10-year forecasts (Figure 4.15a).

4.6 Summary and Conclusion

In this chapter we applied a recently developed technique of climatologically relevant Singular Vector (CSV) to examine the error growth of OLR prediction over South Asian Monsoon (SAM) region, at monthly time scales using both CAM4 and the CCSM4 model. Different perturbation domains and optimal growth intervals are chosen to identify the perturbation structures most favorable for the error growth of SAM prediction. The CSVs are computed using both uncoupled and coupled models to investigate the role of coupling in the error growth of SAM prediction. The robustness of CSVs is demonstrated through the analysis of sensitivity experiments. The CSVs over Indian Ocean are extracted to generate SAM ensemble forecasts.

It is seen that the CSV resembles a dipole-like structure over the Indian Oceans and the ENSO-like pattern over the Pacific Ocean. The magnitude of error growth (singular value) is different over the Indian Ocean and over the Pacific Ocean. When the CSVs are extracted over the Indian Ocean, their growth rates are found to be more consistent with the increase of lead time and generally larger than the counterparts over the Pacific Ocean. Different parameters such as the number of the EOF modes used for initial perturbation and the number of ensemble members are tested to evaluate CSV robustness over the Indian Ocean.

Ensemble forecasts constructed using negative and positive CSVs over the Indian Ocean are compared with forecasts using the Time Lag Ensemble (TLE) method and the single control forecast for the period of 10 years from 2000 to 2009. It is seen that the ensemble forecast generated by CSV perturbations has a more reliable ensemble mean compared to both the TLE mean and the control forecast, and its RMSE is found significantly better than TLE and

control forecast at lead times beyond 2 months. To explore the consistency and robustness of the hindcast results, we also extended the hindcast to the period of 30 years from 1980-2009, and obtained similar conclusions, namely that, the ensemble prediction by the CSV is better than that by TLE and the control forecast, further confirming the merits of the CSV method for SAM prediction.

While this study facilitates the investigation of the SAM optimal error growth by using the CSV method, some cautions should be mentioned. First, the main model used in this study is an atmospheric general model (CAM4), which lacks some key dynamics related to the air-sea coupling. Limited validation is conducted using the coupled model (CCSM4) to conduct the analysis of error dynamics using the CSV method. Nevertheless this work seems to be the first to explore the optimal error growth of SAM seasonal prediction, and the results reported here offer valuable insight to SAM predictability and have practical significance for ensemble prediction. These findings have implications for the SAM seasonal forecast in both the construction of the ensemble forecast system and the detection of key oceanic areas that impact SAM forecast, where the uncertainties can be reduced by adaptive observations and data assimilation.

Table 4.1: List of experiments used for CSV analysis including detail of perturbation domain, number of perturbation EOFs, number of ensembles and forecast years.

Exp. Name	Description	Perturbation Domain	Time Span	Initial Conditions (IC)	No of EOFs used	Ensemble Members for each EOF
IO30	30 years perturb run using EOFs as perturbations	Indian Ocean	1980-2009	Control run IC created with prescribed SST	3	10
IO10	10 years perturb run using EOFs as perturbations	Indian Ocean	2000-2009	Observed IC from NCAR's DART system	3 and 10	10 and 20
PO10	10 years perturb run using EOFs as perturbations	Pacific Ocean	2000-2009	Observed IC from NCAR's DART system	3	10
IO_CCSM4	4 years coupled run using EOFs as perturbations	Indian Ocean	2000, 2004, 2008 and 2009	Observed IC from NCAR's DART system + 100 Year control run SST	3	10
TLE	Time Lag Ensemble forecast	-	2000-2009	6 hours lag observed IC from NCAR's DART system	-	6
CSVp	Ensemble forecast using +ve CSV as perturbations	Indian Ocean	2000-2009	Observed IC from NCAR's DART system	-	10
CSVn	Ensemble forecast using -ve CSV as perturbations	Indian Ocean	2000-2009	Observed IC from NCAR's DART system	-	10
CSV30p	Ensemble forecast using +ve CSV as perturbations	Indian Ocean	1980-2009	Control run IC created with prescribed SST	-	10
Control Forecast	Ensemble forecast without CSV perturbation	-	2000-2009 and 1980-2009	Observed IC from NCAR's DART system	-	10

All experiments start from Jun 1st of every year with lead time of 4 months (June, July, August and September, JJAS). In CAM4 experiments, persistence SST is used as boundary conditions (BC) whereas in CCSM4, SST is used from the multiyear year control run of ocean model.

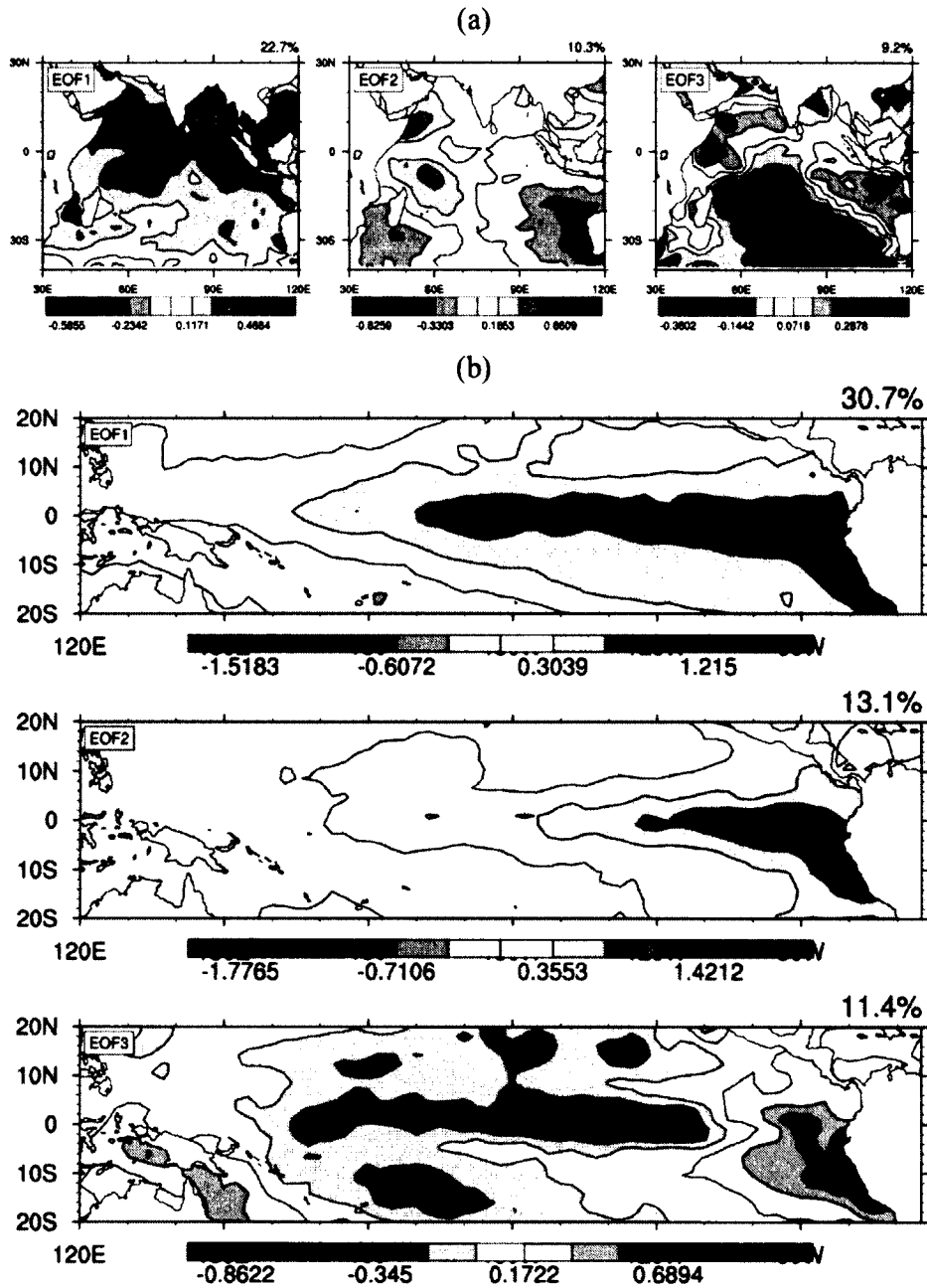


Figure 4.1: First three leading correlation EOFs patterns of the June SST over (a) Indian Ocean and (b) Pacific Ocean. These patterns are calculated from monthly observed SST for time period 1980 to 2009, and are added as perturbation in the instantaneous initial states of persistent SST.

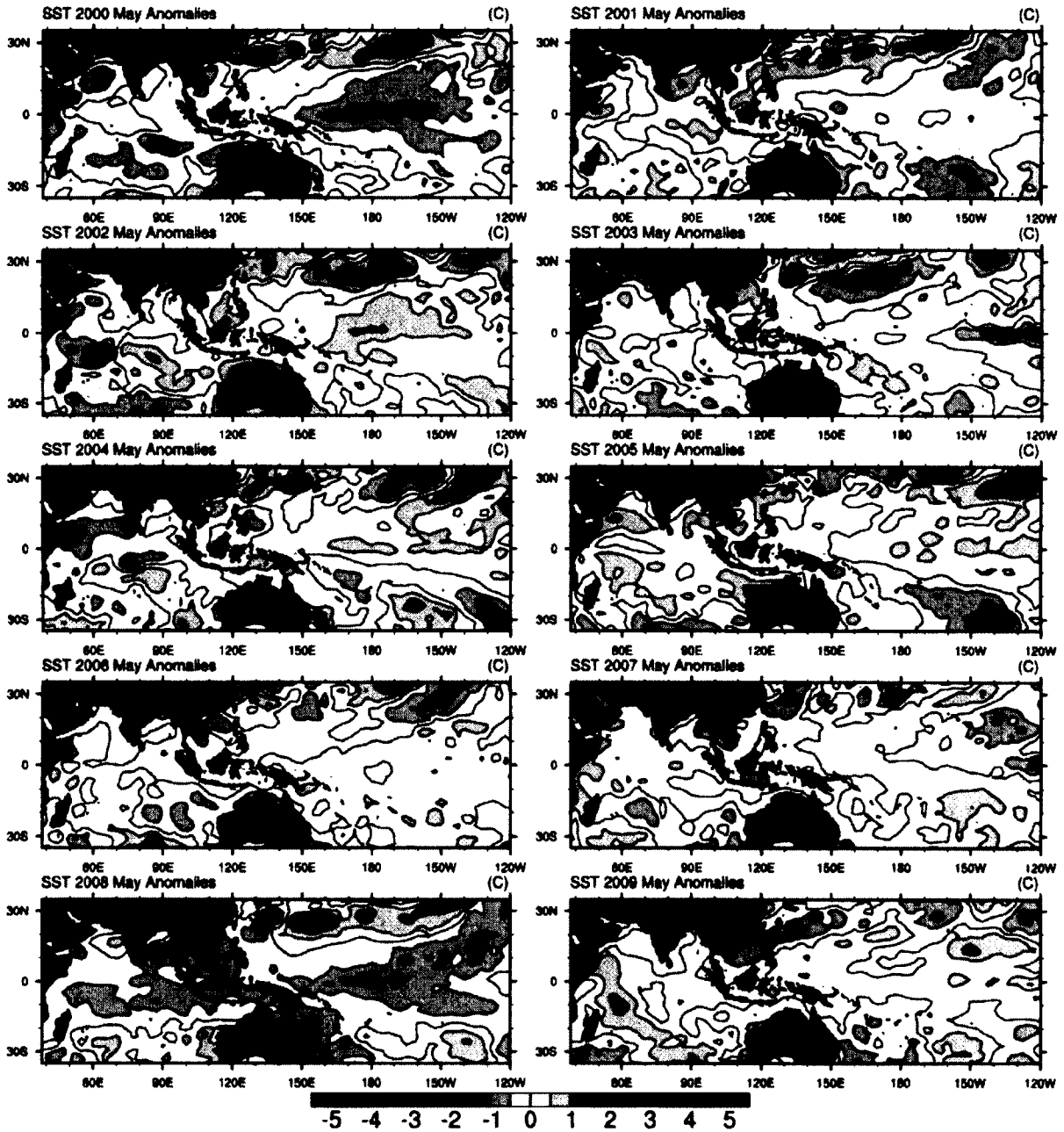


Figure 4.2: SST anomalies for May of each forecast year. Each anomaly pattern is calculated based on the mean SST climatology of 1980-2009 and is kept persistent throughout the forecast. Units are in °C.

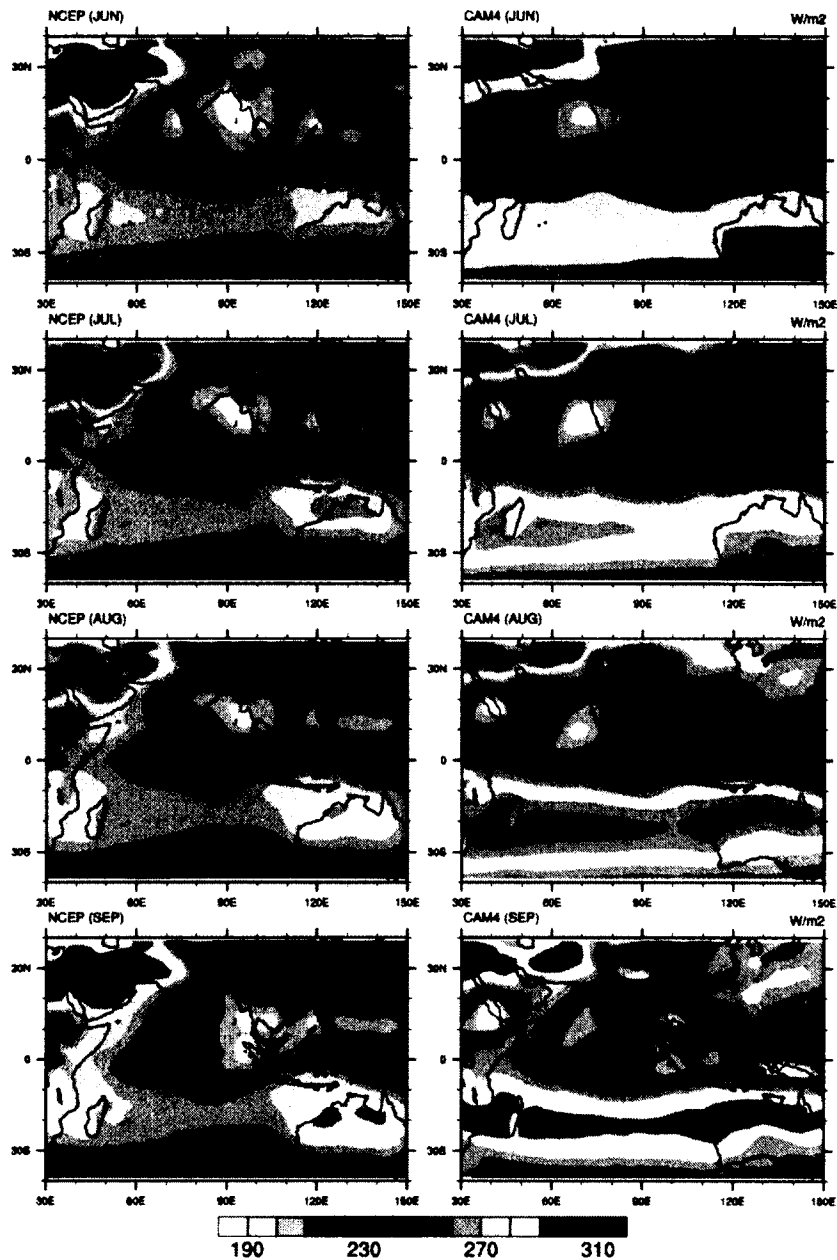


Figure 4.3: Mean climatology of June, July, August and September for Outgoing Longwave Radiation (OLR). NCEP OLR is shown in left column and CAM4 control run is in right column. Mean is calculated over the period 1980 to 2009. The shading corresponds to OLR values in W/m^2 .

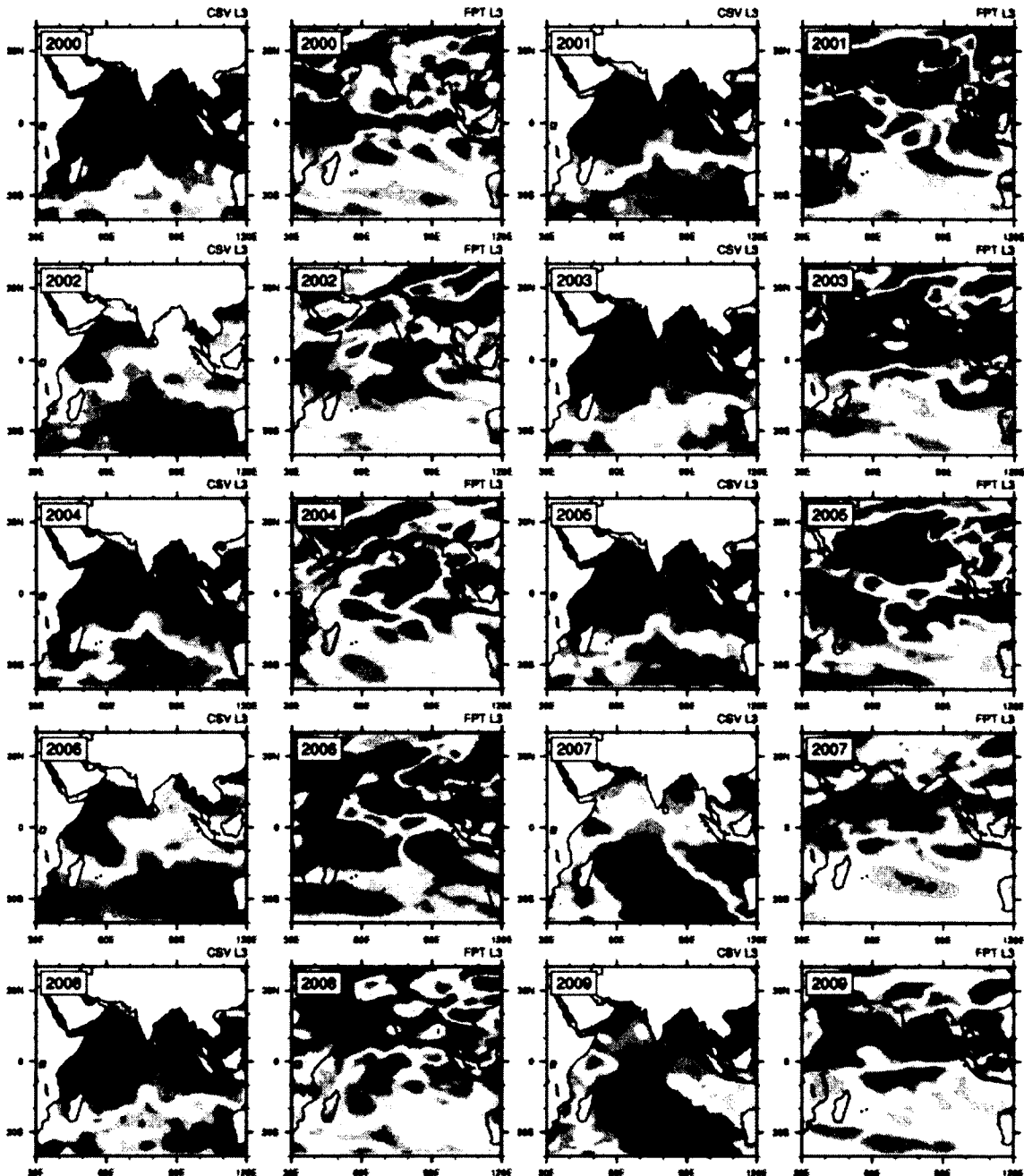


Figure 4.4: The optimal leading Climatology relevant Singular Vectors (CSVs) of SST and corresponding OLR final patterns (FPs) of, optimized for 4 months (lead time 3) over the Indian Ocean domain. Each individual CSV and FP is shown starting from year 2000 to 2009. The SST units are $^{\circ}\text{C}$ and OLR is in W/m^2

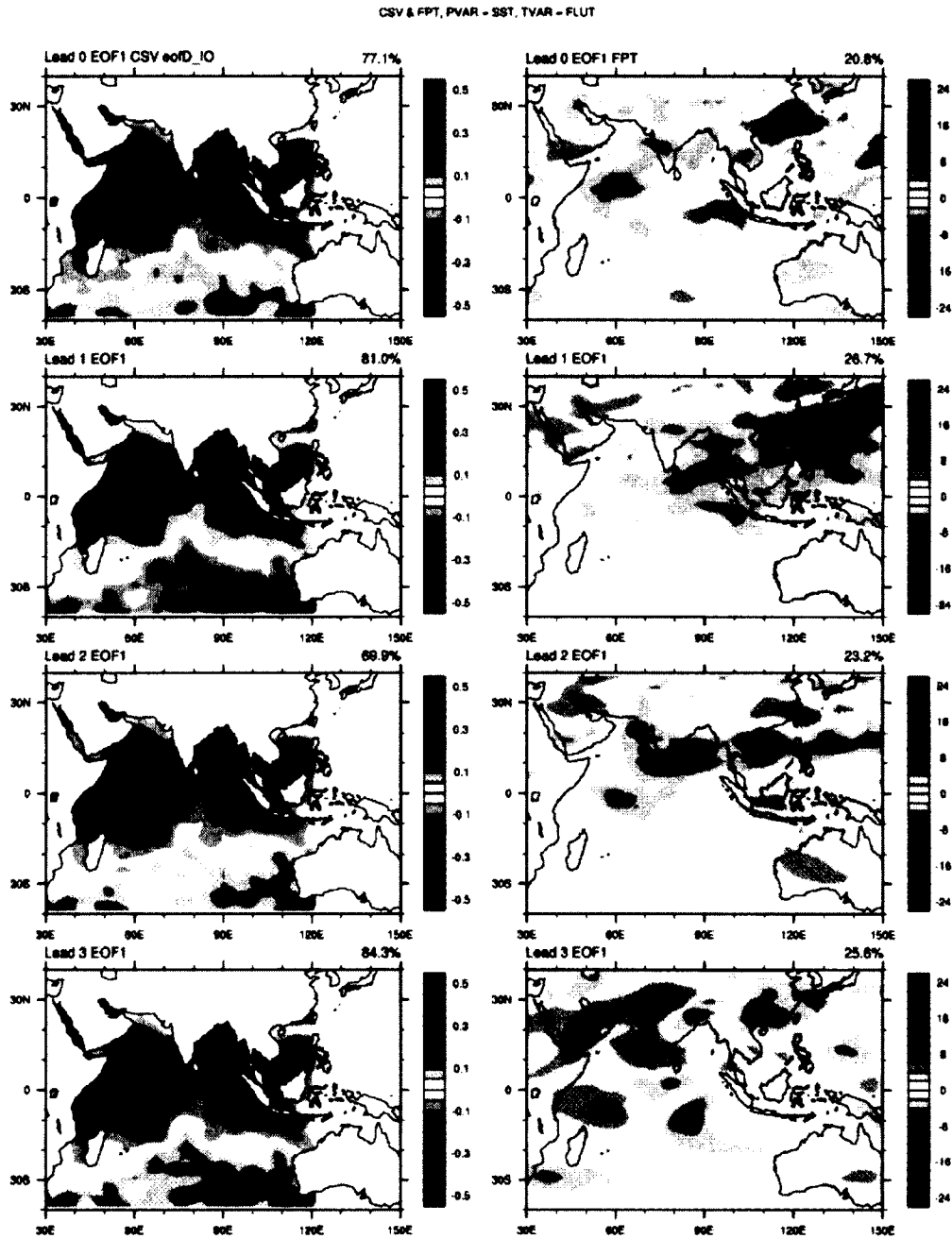


Figure 4.5: The first leading EOF patterns of the CSVs (left) and FPTs (right) computed over 10 individual CSV patterns for all the 4 lead times. CSVs are extracted over Indian Ocean. The SST units are in $^{\circ}\text{C}$ and OLR is in W/m^2 .

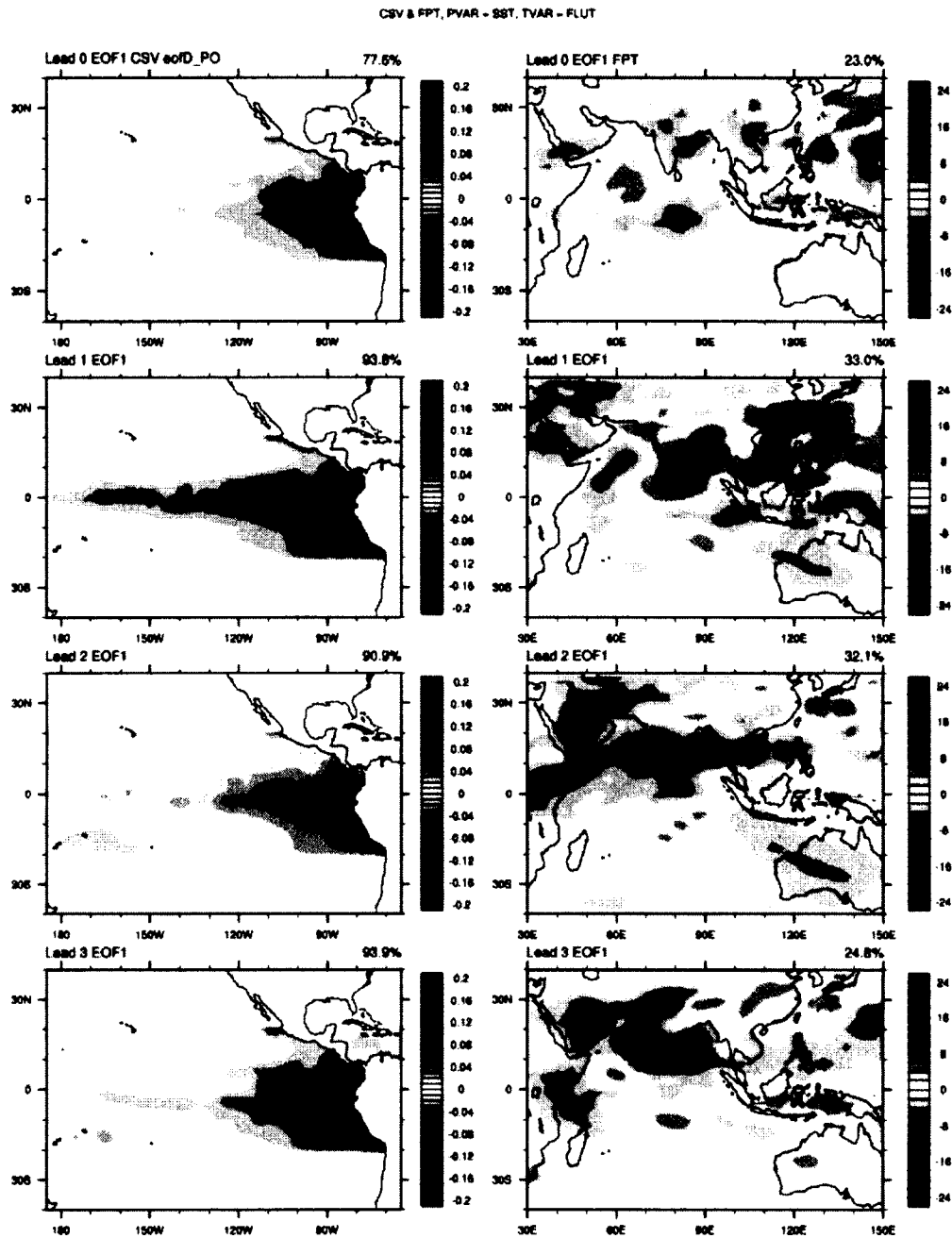


Figure 4.6: Same as Figure 4.5 but for CSVs calculated over Pacific Ocean and corresponding FPs over SAM region. The SST units are in $^{\circ}\text{C}$ and OLR is in W/m^2 .

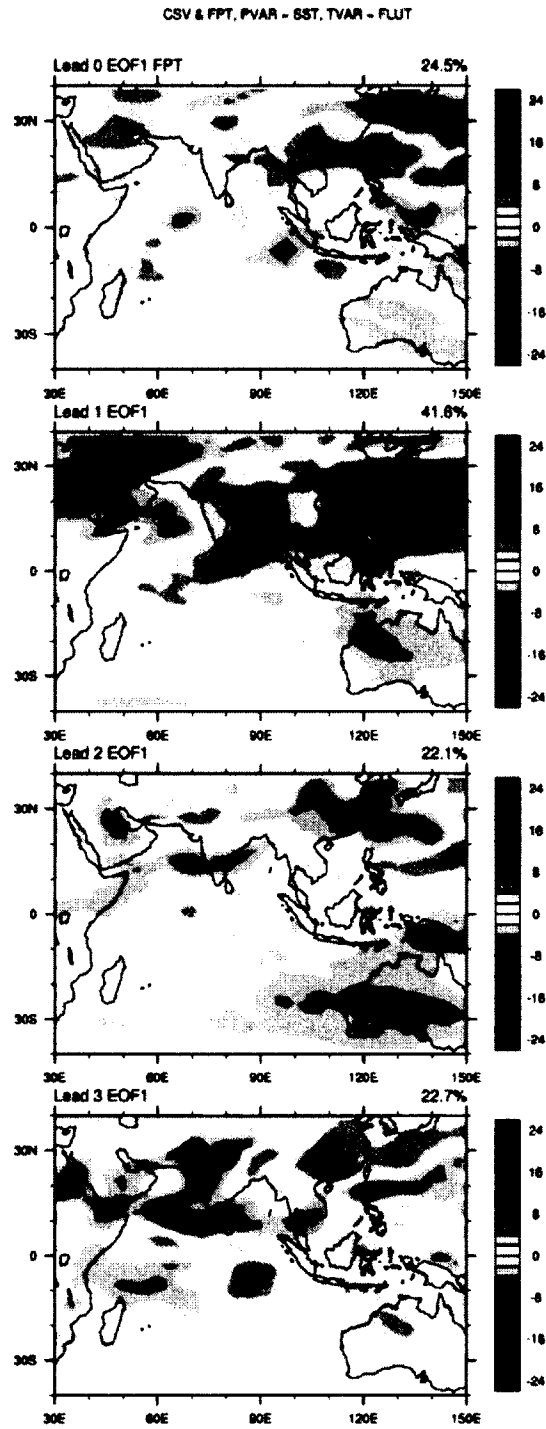


Figure 4.7: Same as Figure 4.6 but for CSV calculated over combined Indian-Pacific Ocean.

Only FPs are shown here.

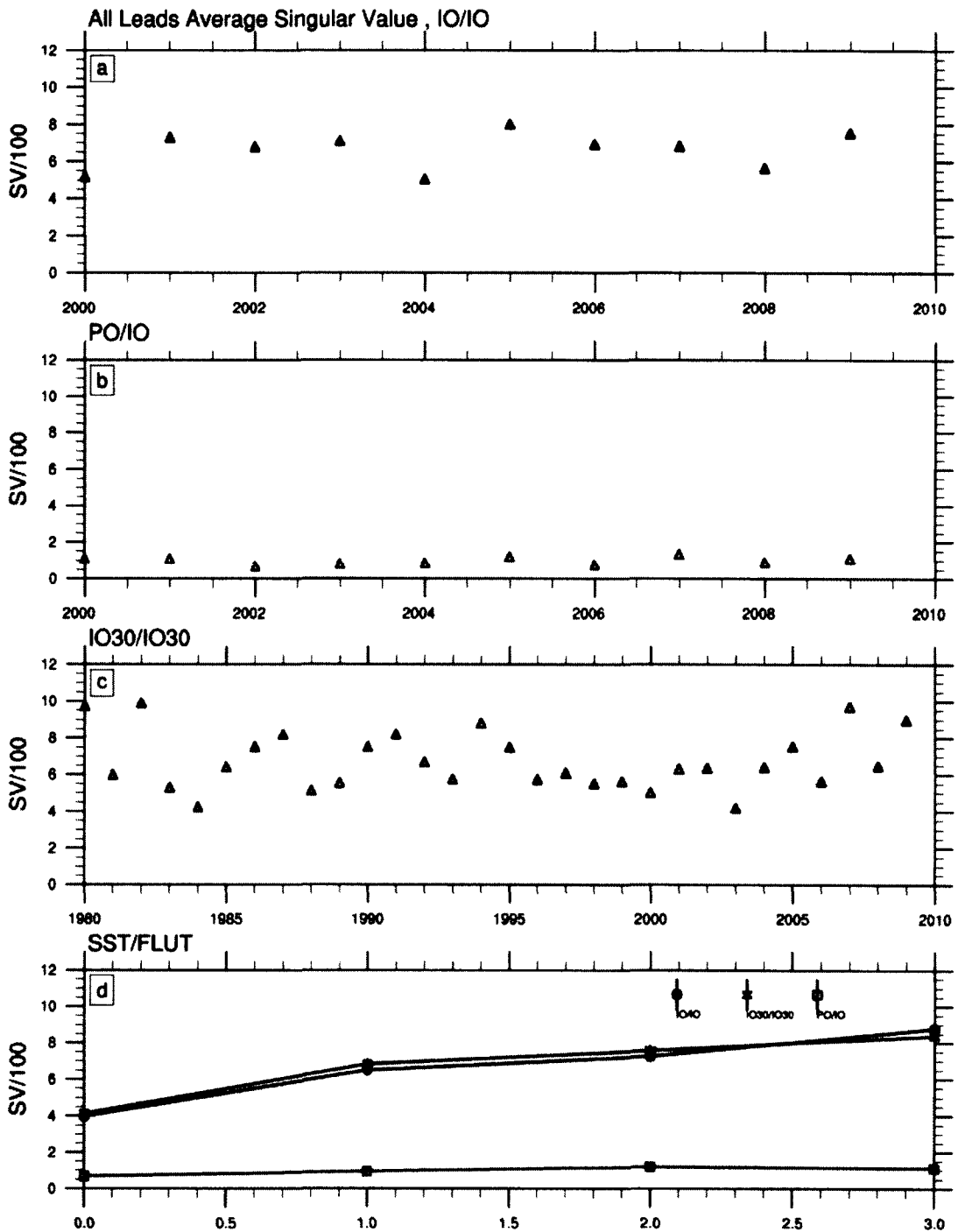


Figure 4.8: Annual variation of singular values averaged over all the lead times for (a) Indian Ocean (b) Pacific Ocean and (c) IO30 experiments. (d) The lead time variation of singular values over all the three cases (see text for detail).

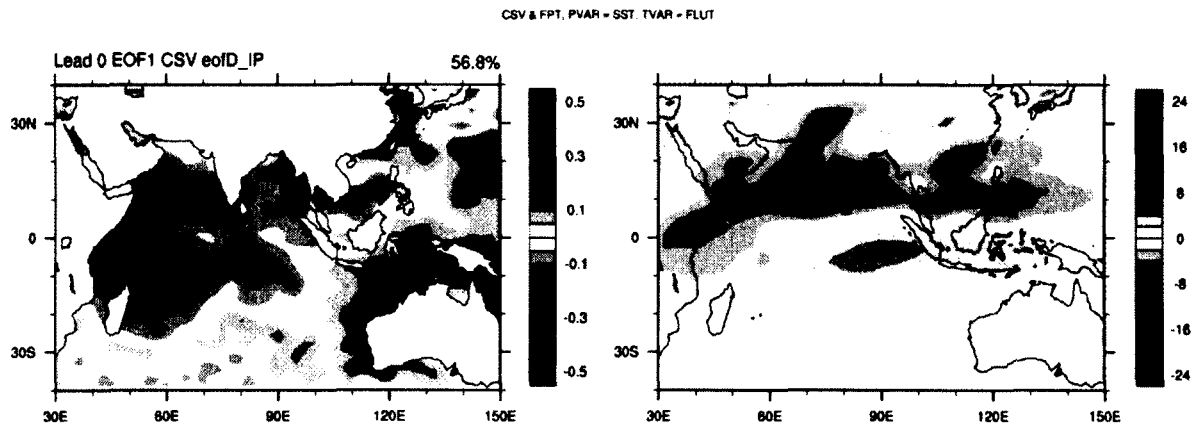


Figure 4.9: Same as Figure 4.5 but for CSVs and FPs calculated over Indian Ocean using IO30 experiment. 30 years CSVs and FPs are used for EOF analysis. The initial conditions for IO30 experiment are generated using CAM4 prescribed SST run.

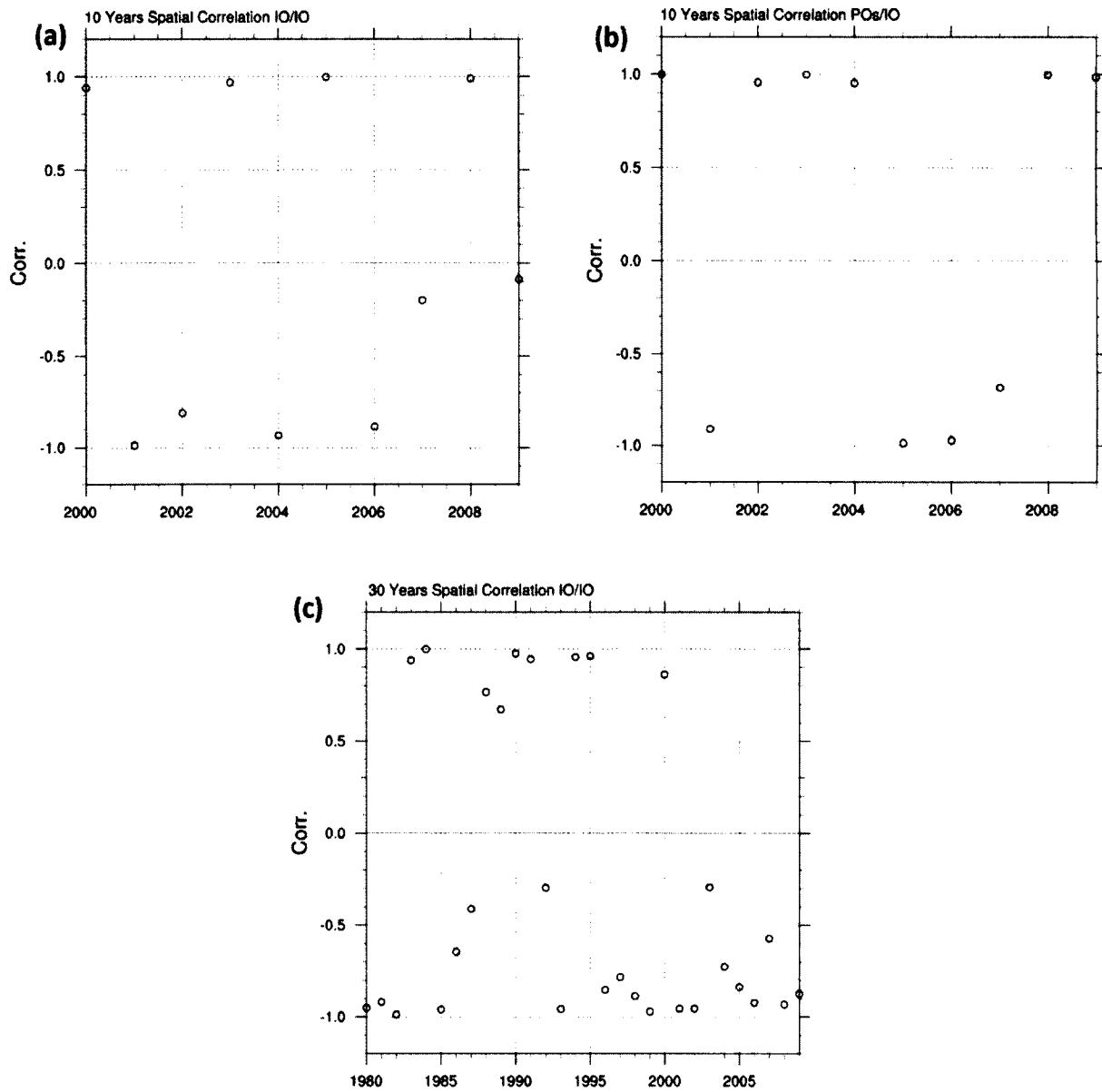


Figure 4.10: The spatial correlation for (a) Indian Ocean, (b) Pacific Ocean and (c) IO30 experiments. It is computed between the first EOF mode (obtained by all CSVs) and each individual CSV pattern, same as in Tang and Deng (2011).

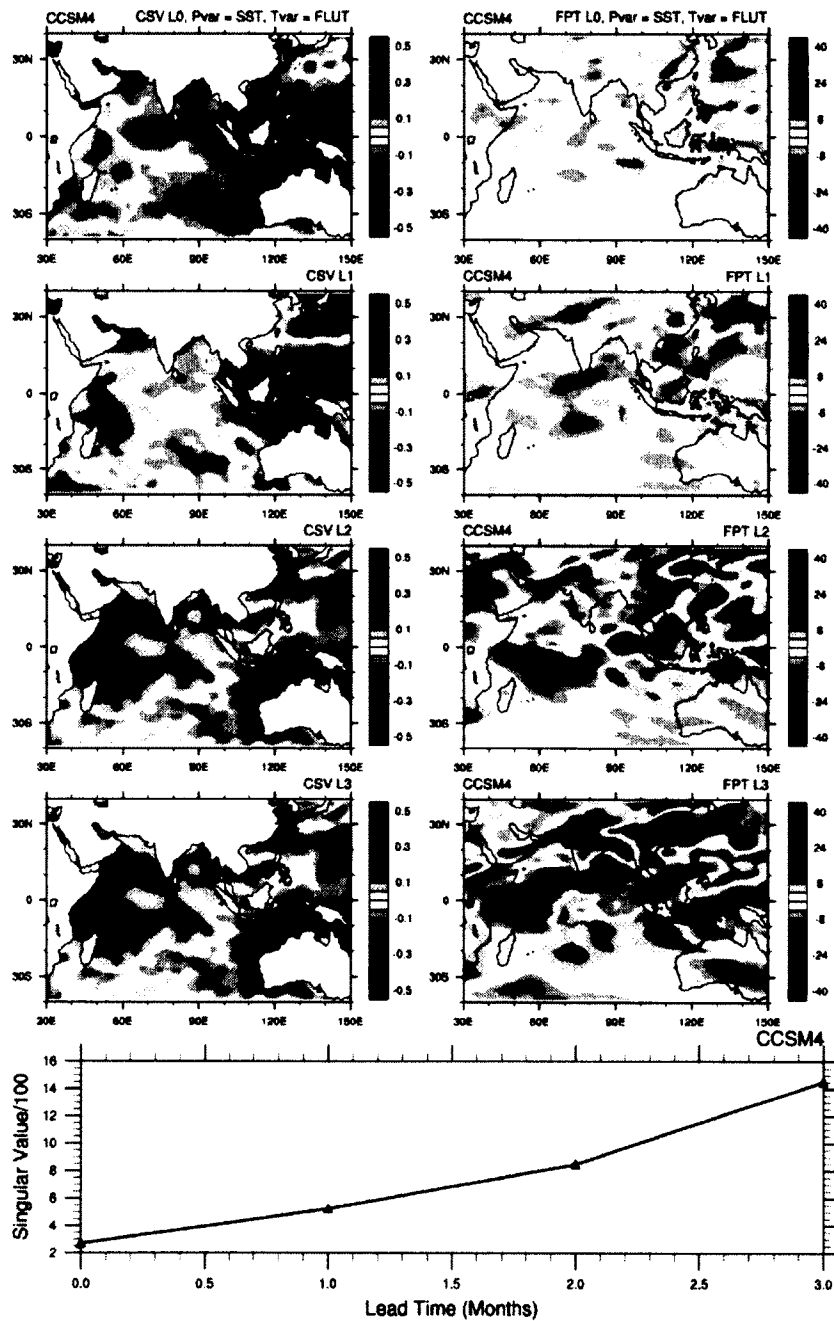


Figure 4.11: (Spatial) The optimal leading SST CSVs and OLR FPs for lead time 0, 1, 2 and 3 obtained using CCSM4 model. The domain of perturbation is Indian Ocean. The SST units are $^{\circ}\text{C}$ and OLR is in W/m^2 . (Line) Lead time variation of CCSM4 singular values over Indian Ocean.

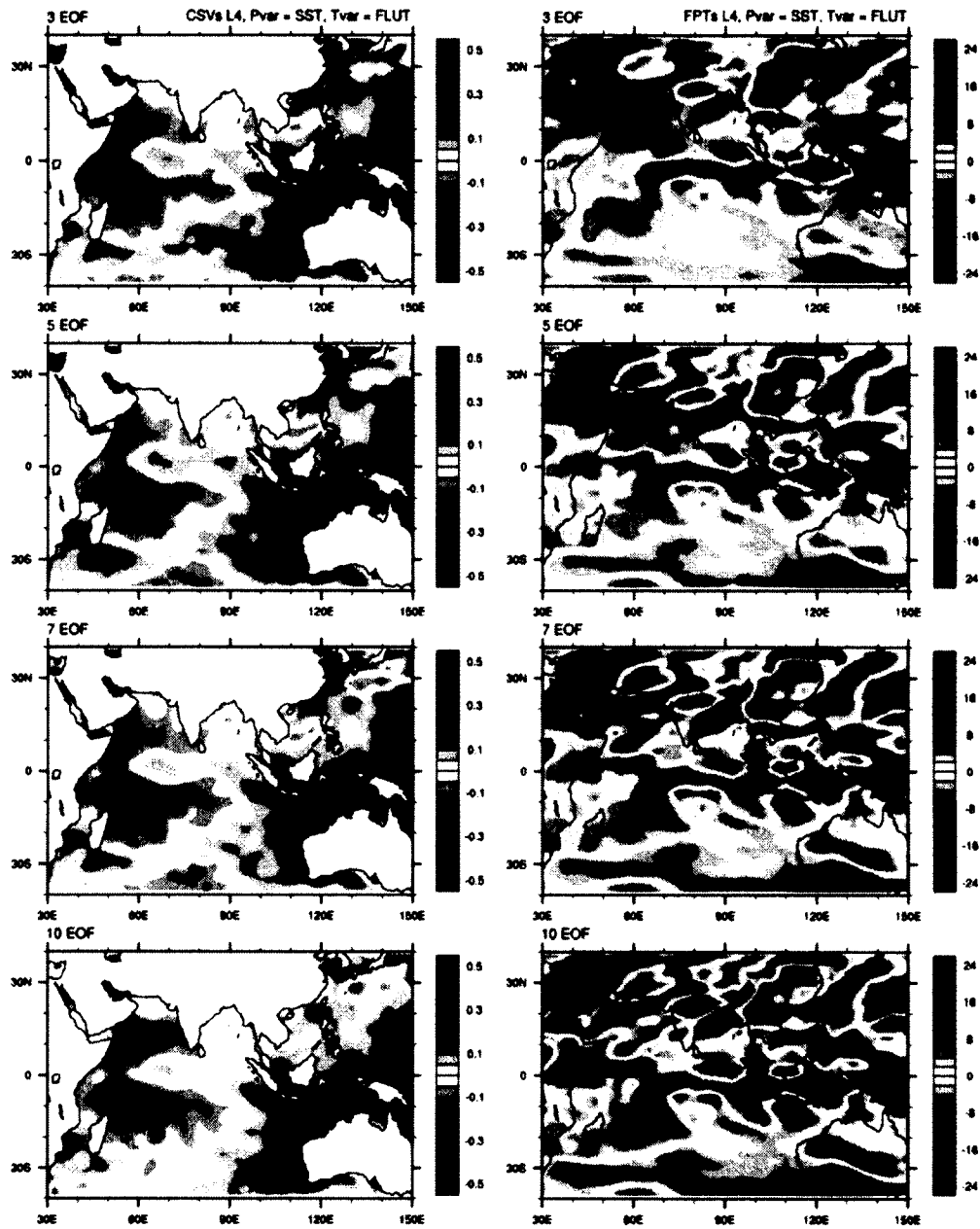


Figure 4.12: Spatial patterns of the leading CSV (left column) based on the increasing number of EOFs used in the perturbation. 10 leading SST correlation EOFs are used by increasing EOFs from 3 to 10 in each CSV and FPs calculation. The optimization time is 4 months. Right column shows associated FPs. The SST units are in $^{\circ}\text{C}$ and OLR is in W/m^2 .

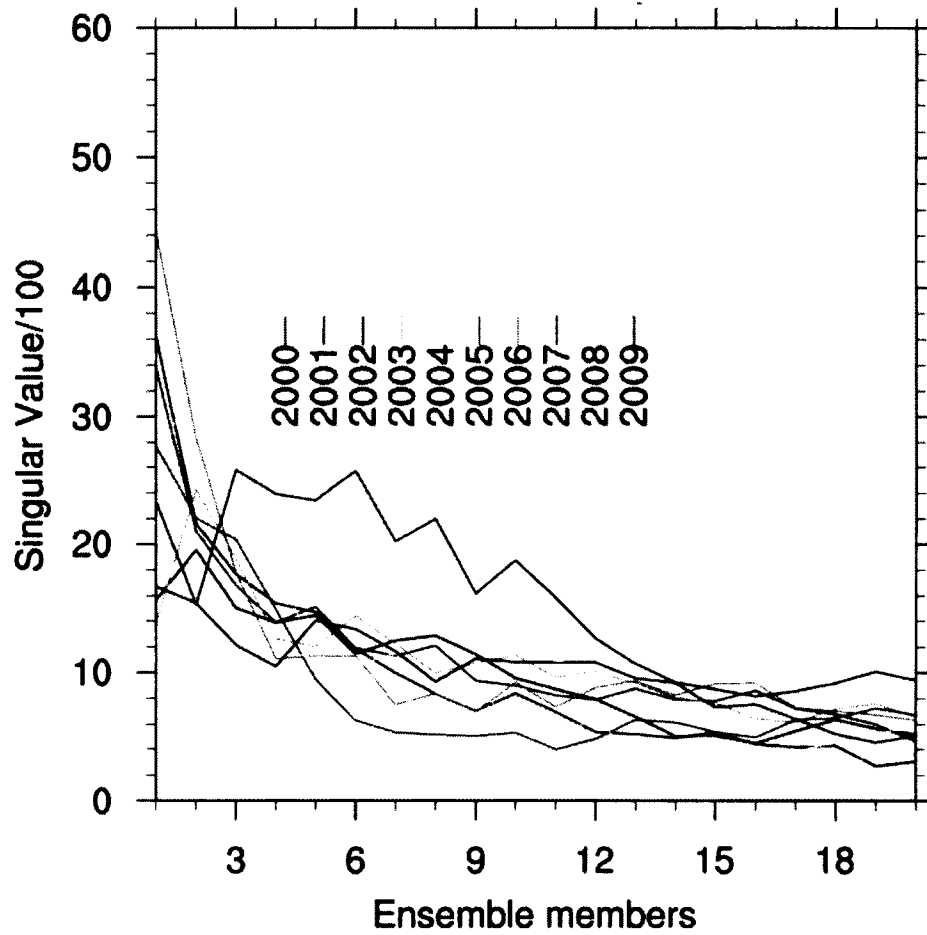


Figure 4.13: The convergence of the leading singular values with increasing number of ensemble members, optimized for 4 month time interval. Each color line represent individual year. In each year, 20 singular values are calculated by increasing the ensemble size from 1 to 20 in the CSV method.

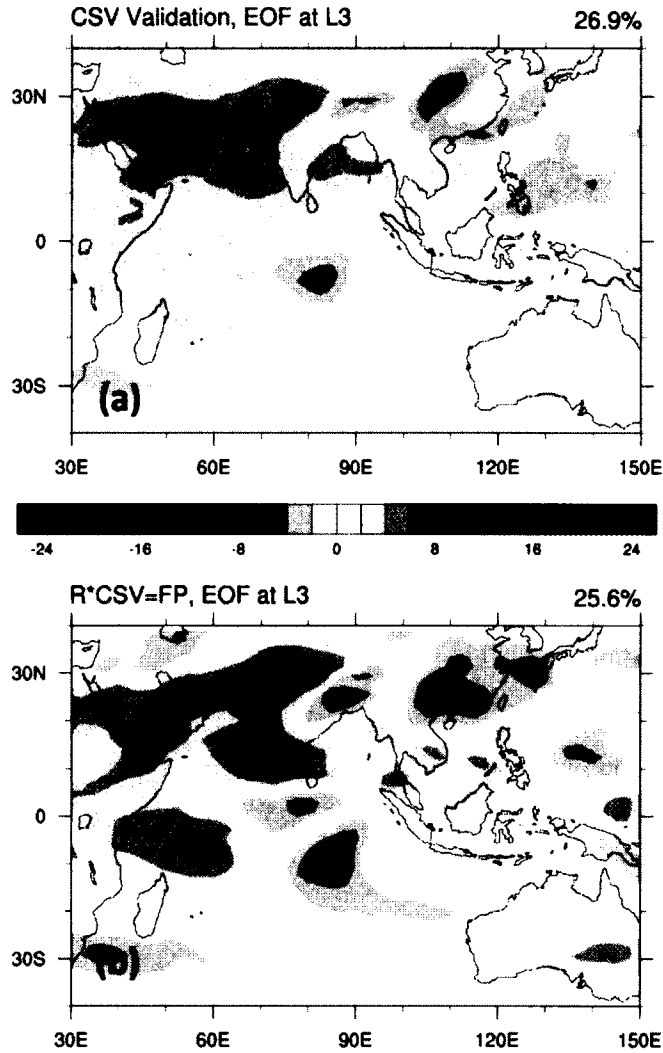


Figure 4.14: Leading EOF of OLR FPs, at lead time 3, (a) calculated using CSV as perturbation and (b) estimated by applying linear propagator R to CSV i.e. by linear approximation. For (a), the difference of perturbed and control forecast is calculated each year and leading EOF is extracted using all the differences. In (b), EOF pattern is calculated using estimated FPs from linear approximation for all the 10 years (2000-2009).

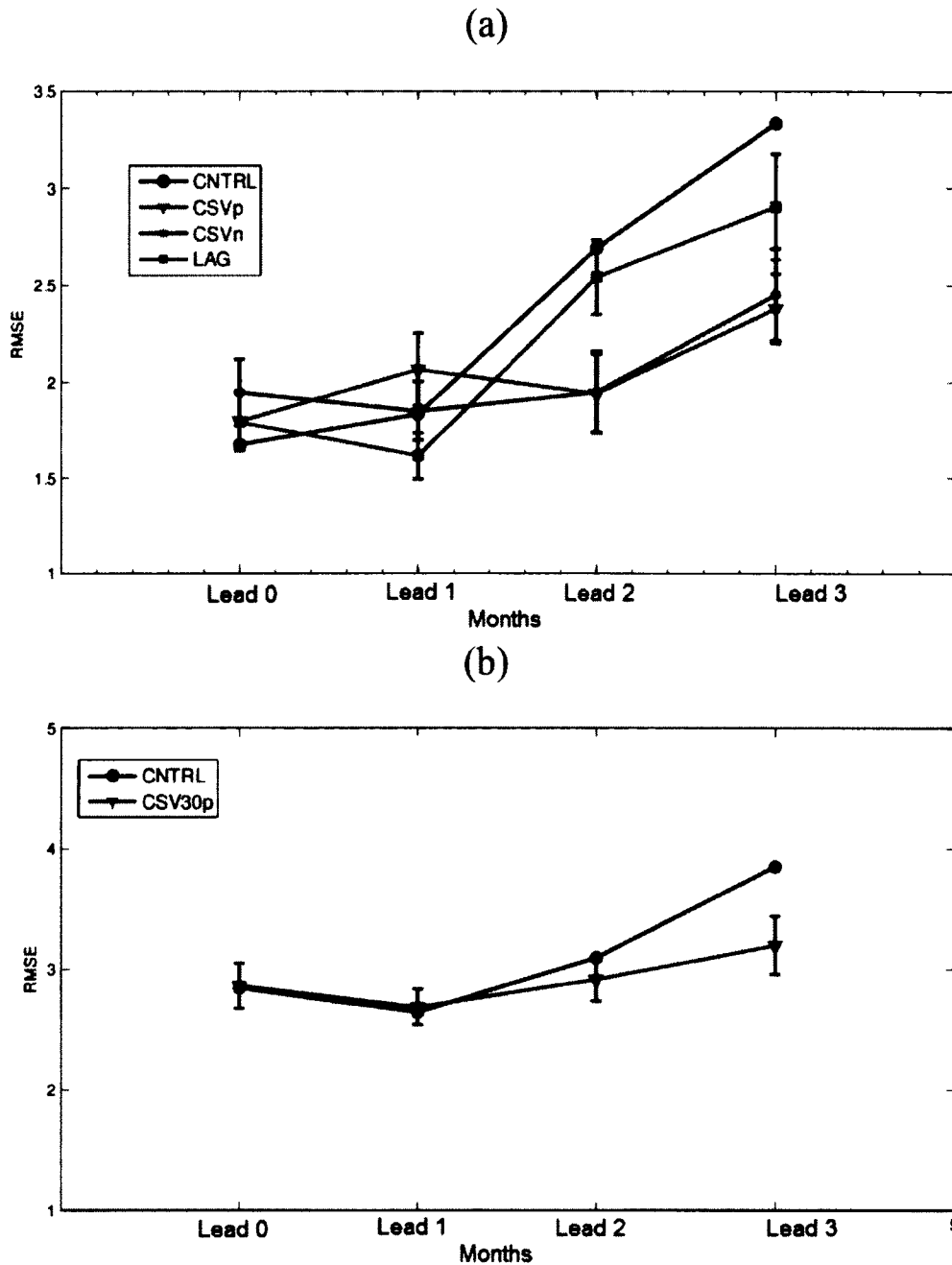


Figure 4.15: Root mean square error (RMSE) of the SAM ensemble forecast generated using CSV perturbation. (a) RMSE calculated over 10 years (2000-2009 using observed initial conditions) whereas in (b) RMSE is for 30 years forecast (1980-2009 using CAM4 control initial conditions). Error bar is drawn using bootstrap method.

Chapter 5

Summary and Discussion

5.1 Thesis Summary

This thesis investigates some important issues related to South Asian Monsoon (SAM) simulation and its seasonal predictability using comprehensive climate models. A number of findings and conclusions are obtained through detailed analysis of model experiments and simulation outputs, which are summarized below.

The different features of the SAM precipitation in the simulations of NCAR's uncoupled (CAM4/5) and coupled (CCSM4) climate models are discussed in Chapter 2. The comparison of simulations is performed against observations to identify strengths and discrepancies in these models. The mean climatology of the SAM, its interannual variability and air-sea interactions are evaluated using different measures. The impact of SST biases on the SAM simulation and the importance of air-sea coupling are also explored in this chapter.

The results reveal numerous key aspects of CAM4 and CCSM4 in simulating SAM precipitation. Compared to the versions previous to CAM4 and CCSM4, improvements in eliminating many regional biases are seen in both models. The spatial pattern and the seasonal cycle of monsoon precipitation is fairly well reproduced in the simulations along with the monsoon onset between May and June, the high precipitation during June-August and slow withdrawal during September-October. The large northward shift of the ITCZ from January to July is also well simulated. A pronounced improvement in precipitation simulation, such as the regional bias reduction over complex terrain, is seen when the CAM4

resolution is increased. The improved SAM monsoon is seen in CCSM4 simulations with the reduction of many biases particularly over the Arabian Peninsula and the western coast of India. The period of ENSO is found to be more realistic in CCSM4 than in the previous version (e.g. CCSM3).

Along with improvements, the systematic errors of both models are also identified. Inconsistencies in the oscillatory period and amplitude of monsoon interannual variability are seen in CAM4 simulations. The bias in the CAM4 seasonal mean climatology results in excessive precipitation over the Arabian Sea and over the Western Ghats of India and reduced precipitation over the eastern Indian Ocean extending into the Bay of Bengal. In CAM4, the East Asian summer monsoon precipitation is simulated better than the SAM precipitation.

The interrupted northward progression and delayed onset of the monsoon over the SAM region is seen in the CCSM4 simulation including the double ITCZ problem that was also present in the previous versions of the CCSM model (CCSM3). A systematic cold SST bias over the tropical Pacific Ocean is revealed in simulations. Significant cold biases over the equatorial Pacific Ocean are found in CCSM4, particularly in winter and early summer.

The importance of air-sea coupling is investigated by forcing CAM4 with coupled model SST which revealed that the local air-sea coupling over the SAM region acts to modulate the SAM summer rainfall activity. Further, it is seen that along with air-sea interaction, SST bias in the CCSM4 model plays an important role in modulating the variability and magnitude of SAM precipitation. The influence of the coupled model SST bias in the northern Indian

Ocean on SAM precipitation is investigated, with a conclusion that the reduction in excessive SAM rainfall in CCSM4 simulation is mainly due to a cold SST bias in the Arabian Sea.

Chapter 3 focuses on a detailed investigation of ENSO-SAM relationships in CAM4 and CCSM4, attempting to identify the strength and discrepancies of these models in preserving different types of ENSO-SAM relationships. The analyses in this chapter are performed on the basis of a recent classification scheme of the ENSO-SAM relationships by Wu et al, (2012). They have identified three different types of ENSO influences on the SAM using observations (DJF-only, JJAS-only and DJF&JJAS). We have extended their analysis to our simulation results, and further explored the physical understanding of particular types of ENSO influence on SAM using sensitivity experiments.

Using the composite analysis for model simulations and observations, the performance of CAM4 and CCSM4 is evaluated for the ENSO-SAM relationship. It is seen that the CAM4 simulation in DJF-only type is better than CCSM4, and can reproduce a realistic anomalous rainfall over the east Pacific reasonably well along with some biases over the western Pacific Ocean and Maritime continent. In contrast, the CCSM4 showed large systematic errors including significant rainfall anomaly biases in the Indian Ocean from the preceding winter to the early spring, probably due to the errors in SST simulation. In DJF-only years, the CAM4 performed better than CCSM4.

For JJAS-only type, the CAM4 showed significant disagreement for SAM rainfall anomalies as compared to observations and CCSM4 simulation. It is found that ENSO induced warming in northern Indian Ocean via atmospheric circulation is absent in CAM4 simulation of the JJAS-only type, probably due to the lack of air-sea coupling. The CCSM4 simulation has

shown strong convergence over the SAM region, intensifying the anomalous SAM. The CCSM4 results are found to be more realistic than CAM4 as compared with observation.

In the DJF&JJAS type, realistic anomalous rainfall is reproduced by CAM4 as compared to CCSM4 which has a very weak simulation of rainfall anomalies. Compared to the other two types, the CAM4 has the better simulation of the ENSO-SAM relationship in the DJF&JJAS type, including a more realistic simulation in moisture content and thickness difference.

The role of the Indian Ocean in controlling the DJF&JJAS type ENSO-SAM teleconnection is further investigated by CAM4 sensitivity experiments. It is found that in the absence of Indian Ocean SST anomalies, the anomalous SAM summer rainfall is suppressed in the DJF&JJAS type, suggesting the importance of Indian Ocean SST in modulating the east equatorial Pacific SST and SAM interaction.

In Chapter 4, both the CAM4 and CCSM4 models are used to implement a recently developed technique of climatologically relevant Singular Vector (CSV) to examine the error growth of OLR prediction over SAM region. Both the Indian and Pacific Oceans are used as perturbation domains and different optimal growth intervals are chosen to identify the perturbation structures most favorable for the error growth of SAM prediction. The CSVs and corresponding final patterns (FP) are calculated for both uncoupled and coupled simulations. The robustness of CSVs is confirmed by sensitivity experiments. Different parameters such as the number of the EOF modes used for initial perturbation and the number of ensemble members are tested in these sensitivity experiments. The CSVs over the Indian Ocean are used to perform SAM ensemble forecasts.

It is seen that the magnitude of error growth (singular value) is different over the Indian Ocean and over the Pacific Ocean. The growth rates over the Indian Ocean are found to be more consistent with the increase of lead time and generally larger than the growth rates over the Pacific Ocean. The CSVs are found to be insensitive to initial conditions whereas FPs are much different from case to case.

The optimized CSVs over the Indian Ocean are further used to construct a SAM ensemble forecast. The CSV-based ensemble forecast is compared with that by Time Lag Ensemble (TLE) and the single control forecast for the period from 2000-2009. A more realistic ensemble mean is obtained in the CSV-based ensemble forecast as compared to TLE and the control forecast. There is also a significantly lower RMSE in the CSV ensemble forecast than in other methods at lead time beyond 2 months. The hindcast is also extended to the period of 30 years, from 1980-2009, further confirming the merits of the CSV ensemble method for SAM prediction.

5.2 Discussion

The simulation of South Asian summer monsoon by models depends mainly on how realistically they simulate the mean state and variability of the SAM, and how well they represent the monsoon internal dynamics and air-sea interactions. In general, modeling SAM fluctuations depends mainly on understanding the fundamental processes of SAM, model parameterization schemes and the methods used for numerical implementation of these processes.

The NCAR climate modeling system, including CAM4 and CCSM4, has been widely used to improve our capability in simulating and predicting climate, and made significant progress in

various aspects. However biases in these models can adversely affect the SAM simulation, particularly in the region where the ENSO-monsoon relationship is important. Thus, further efforts are required in model development, including improving model physics and model resolution as well as coupling processes, particularly over the complex SAM topography. The reliability of current coupled models, due to their SST biases, is not at a level where the local air-sea feedbacks can be used to improve the seasonal predictability of SAM.

In case of the seasonal prediction, the skill of comprehensive climate models may be increased up to the theoretical limit of predictability inherent in the nonlinear and stochastic processes of climate system. Since there are uncertainties in initial and boundary conditions, a single forecast is of limited value. Instead, an ensemble of forecasts is necessary to capture the most likely range of forecast states that are expected to arise given the uncertainties in the initial and boundary conditions. The methods used to sample the initial uncertainty are crucial and can be achieved by using the advanced ensemble construction methods such as the one discussed in this thesis. The challenging issue is to design and implement a reliable ensemble forecast strategy that should include the major uncertainties of forecast initial states.

The work reported in this thesis is subject to some cautions. For example, the perturbation growth method used in this study can be significantly influenced by the model used in its implementation. The main implementation model is an atmospheric general circulation model (CAM4), which lacks coupled air-sea dynamics and has systematic biases in SAM simulation. The small sample size used in perturbation theory analysis may limit the generality and robustness of results. Nevertheless, this work has theoretical significance and practical importance in SAM simulation and prediction. For example, the perturbation

growth theory presented in this research is to our knowledge the first to explore the optimal error growth of SAM seasonal prediction. This research offers a valuable insight on SAM predictability and proposes a practical method in constructing optimal SAM ensemble predictions.

References

- AchutaRao KM and Sperber KR (2006), ENSO simulation in coupled ocean-atmosphere models: are the current models better? *Climate Dynamics*, 27:1-15. doi: 10.1007/s00382-006-0119-7
- Acharya N, Kar SC, Mohanty UC, Kulkarni MA and Dash SK (2011), Performance of GCMs for seasonal prediction over India - a case study for 2009 monsoon. *Theoretical Applied Climatology*, 105:505-520.
- Achuthavarier D, Krishnamurthy V, Kirtman BP and Huang B (2012), Role of the Indian Ocean in the ENSO-Indian summer monsoon teleconnection in the NCEP climate forecast system. *Journal of Climate*, 25(7):2490-2508.
- Annamalai H and Liu P (2005), Response of the Asian Summer Monsoon to changes in El Niño properties. *Quarterly Journal of the Royal Meteorological Society*, 131:805-831.
- Annamalai H, Hamilton K and Sperber KR (2007), South Asian summer monsoon and its relationship with ENSO in the IPCC AR4 simulations. *Journal of Climate*, 20:1071-1092. doi:10.1175/JCLI4035.1
- Anderson J, Hoar T, Raeder K, Liu H, Collins N, Torn N, and Avellano A (2009), The data assimilation research testbed: A community facility. *Bulletin of the American Meteorological Society*, 90:1283-1296.

- Ashok K, Guan Z, and Yamagata T (2001), Impact of the Indian Ocean Dipole on the relationship between the Indian monsoon rainfall and ENSO. *Geophysical Research Letters*, 28:4499-4502.
- Bamzai AS and Shukla J (1999), Relation between Eurasian snow cover, snow depth and the Indian summer monsoon: an observational study. *Journal of Climate*, 12:3117-3132.
- Becker BD, Slingo JM, Ferranti L, and Molteni F (2000), Seasonal predictability of the Indian Summer Monsoon: What role do land surface conditions play? *Mausam*, 52:47-62.
- Boschat G, Terray P and Masson S (2012), Robustness of SST teleconnections and precursory patterns associated with the Indian summer monsoon. *Climate Dynamics*, 38(11-12):2143-2165.
- Bollasina M and Nigam S (2009), Indian Ocean SST, evaporation, and precipitation during the South Asian summer monsoon in IPCC AR4 coupled simulations. *Climate Dynamics*, 33:1017-1032. doi:10.1007/s00382-008-0477-4
- Buizza R and TN Palmer (1995), The singular vector structure of the atmosphere global circulation. *Journal of Atmospheric Science*, 52:1434-1456.
- Buizza, R, and TN Palmer (1998), Impact of ensemble size on ensemble prediction. *Monthly Weather Review*, 126:2503-2518.
- Cane MA, Zebiak SE and Dolan SC (1986), Experimental forecasts of El Niño. *Nature*, 321:827-832

- Charabi Y, and Abdul-Wahab SA (2009), Synoptic aspects of the summer monsoon of southern Oman and its global teleconnections, *Journal of Geophysical Research*, 114:D07107. doi:10.1029/2008JD010234.
- Chang EC, Yeh SW, Hong SY, Wu R (2011), The role of air-sea interaction over the Indian Ocean in the in-phase transition from the Indian summer monsoon to the Australian boreal winter monsoon, *Journal of Geophysical Research*, 116:D 01107.
- Chen YQ, Battisti DS, Palmer TN, Barsugli J, Sarachik ES (1997), A study of the predictability of Tropical Pacific SST in a coupled atmosphere-ocean model using singular vector analysis: the role of the annual cycle and the ENSO cycle. *Monthly Weather Review*, 125:831-845.
- Chen D, Cane MA, Kaplan A, Zebiak SE and Huang D (2004), Predictability of El Niño over the past 148 years. *Nature*, 428:733-736.
- Cheng Y, Tang Y, Zhou X, Jackson PL, Chen D (2010), Further analysis of singular vector and ENSO predictability in the Lamont model - Part I: singular vector and the control factors, *Climate Dynamics*, 35:807-826. doi:10.1007/s00382-009-0595-7.
- Cherchi A and Navarra A (2007), Sensitivity of the Asian summer monsoon to the horizontal resolution: differences between AMIP-type and coupled model experiments. *Climate Dynamics*, 28:273-290. doi:10.1007/s00382-006-0183-z
- Charney JG and Shukla J (1981), Predictability of monsoons, in *Monsoon Dynamics*, edited by J. Lighthill and R. P. Pearce, *Cambridge University Press*, 99-109.

- Chowdary J, Xie SP, Lee JY, Kosaka Y and Wang B (2010), Predictability of summer Northwest Pacific climate in eleven coupled model hindcasts: local and remote forcing, *Journal of Geophysical Research*, 115:D22121, doi:10.1029/2010JD014595
- Chung C and Nigam S (1999), Asian summer monsoon–ENSO feedback on the Cane–Zebiak model ENSO. *Journal of Climate*, 12:2787-2807
- Collins WD, Rasch PJ, Boville BA, Hack JJ, McCaa JR, Williamson DL, Briegleb BP, Bitz CM, Lin S and Zhang M, (2006a), The Formulation and Atmospheric Simulation of the Community Atmosphere Model Version 3 (CAM3). *Journal of Climate*, 19:2144-2161. doi: 10.1175/JCLI3760.1
- Collins WD, Bitz CM, Blackmon ML, Bonan GB, Bretherton CS, Carton JA, Chang P, Doney SC, Hack JJ, Henderson TB, Kiehl JT, Large WG, McKenna DS, Santer BD and Smith RD, (2006b), The Community Climate System Model Version 3 (CCSM3). *Journal of Climate*, 19:2122-2143. doi: 10.1175/JCLI3761.1
- Covey C, AchutaRao KM, Lambert SJ and Taylor KE (2000), Intercomparison of present and future climates simulated by coupled ocean–atmosphere GCMs. PCMDI report no 66. Program for climate model diagnosis and intercomparison, Lawrence Livermore National Laboratory. *University of California, Livermore*
- Covey C, AchutaRao KM, Cubasch U, Jones P, Lambert SJ, Mann ME, Phillips TJ and Taylor KE (2003), An overview of results from the coupled model intercomparison project (CMIP). *Global and Planetary Change*, 37:103-133. doi:10.1016/S0921-8181(02) 00193-5

- Dai A (2006), Precipitation characteristics in eighteen coupled climate models. *Journal of Climate*, 19:4605-4630. doi:10.1175/JCLI3884.1
- DelSole T and Shukla J (2012), Climate models produce skillful predictions of Indian summer monsoon rainfall. *Geophysical Research Letter*, 39:L09-703, doi:10.1029/2012GL051279.
- Delsole T Shukla J (2002), Linear prediction of Indian monsoon rainfall. *Journal of Climate*, 15:3645-3658.
- Doblas-Reyes FJ, Deque M and Piedelievre JP (2000), Multi-model spread and probabilistic seasonal forecasts in PROVOST. *Quarterly Journal of the Royal Meteorological Society*, 126:2069-2087.
- Drbohlav HL and Krishnamurthy V (2010), Spatial Structure, Forecast Errors, and Predictability of the South Asian Monsoon in CFS Monthly Retrospective Forecasts. *Journal of Climate*, 23:4750-4769. doi: <http://dx.doi.org/10.1175/2010JCLI2356.1>
- Du H, Doblas-Reyes FJ, García-Serrano J, Guemas V, Souf-flet Y and Wouters B (2012), Sensitivity of decadal predictions to the initial atmospheric and oceanic perturbations, *Climate Dynamics*, 7(8):2013-2023.
- Efron B and Tibshirani RJ (1993), An Introduction to the Bootstrap. *Chapman and Hall/CRC*, New York, USA, ISBN: 0412042312.
- Fu C and Fletcher JO (1985), The relationship between Tibet-tropical Ocean thermal contrast and interannual variability of Indian monsoon rainfall. *Journal of Climate and Applied Meteorology*, 24:841-847.

- Fu X, Wang B, Bao Q, Liu P and Lee JY (2009), Impacts of initial conditions on monsoon intraseasonal forecasting. *Geophysical Research Letters*, 36:L08801.
- Fu X, Wang B, Lee JY, Wang W and Gao L (2011), Sensitivity of dynamical intraseasonal prediction skills to different initial conditions. *Monthly Weather Review*, 139:2572-2592.
- Gadgil S, Rajeevan M and Nanjundiah R (2005), Monsoon prediction Why yet another failure? *Current Science*, 88:1389-1400.
- Gadgil S and Sajani S (1998), Monsoon precipitation in the AMIP runs. *Climate Dynamics*, 14:659-689.
- Gent P, Danabasoglu G, Donner L, Holland M, Hunke E, Jayne S, Lawrence D, Neale R, Rasch P, Vertenstein M, Worley P, Yang ZL and Zhang M (2011), The Community Climate System Model Version 4. *Journal of Climate*, 24:4973-4991. doi: 10.1175/2011JCLI4083.1
- Gimeno L, Drumond A, Nieto R, Trigo RM, Stohl A (2010), On the origin of continental precipitation. *Geophysical Research Letter*, 37:L13804. doi:10.1029/2010GL043712
- Goswami BN, Krishnamurthy V and Annamalai H (1999), A broad-scale circulation index for the interannual variability of the Indian summer monsoon. *Quarterly Journal of the Royal Meteorological Society*, 125:611-633.
- Goswami BN, Ajaya RS (2001), Intra-seasonal oscillations and inter-annual variability of the Indian summer monsoon. *Journal of Climate*, 14:1180-1198.

- Griffies SM, Winton M, Samuels B, Danabasoglu G, Yeager S, Marsland S, Drange H and Bentsen M (2012), Datasets and protocol for the CLIVAR WGOMD Coordinated Ocean-sea ice Reference Experiments (COREs), *WCRP Report*, No. 21/2012, pp. 21
- Hack JJ, Kiehl JT and Hurrell JW (1998), The hydrologic and thermodynamic characteristics of the NCAR CCM3. *Journal of Climate*, 11:1179-1206.
- Hastenrath S and Polzin D (2004), Dynamics of the surface wind field over the equatorial Indian Ocean. *Quarterly Journal of the Royal Meteorological Society*, 130: 503-517.
- Hawkins ED, Sutton R (2010), Estimating climatically relevant singular vectors for decadal predictions of the Atlantic Ocean, *Journal of Climate*, 24:109-123. doi:10.1175/2010JCLI3579.1
- Holtslag A, Boville B (1993), Local versus nonlocal boundary-layer diffusion in a global climate model. *Journal of Climate*, 6:1825.
- Houtekamer PL, Mitchell HL, Pellerin G, Buehner M, Charron M, Spacek L and Hansen B (2005), Atmospheric Data Assimilation with an Ensemble Kalman Filter: Results with Real Observations. *Monthly Weather Review*, 133:604-620. doi:10.1175/MWR-2864.1
- Hunke EC and Lipscomb WH (2008), CICE: the Los Alamos sea ice model user's manual, version 4. *Los Alamos National Laboratory Technical Report*, LA-CC-06-012.
- Iacono MJ, Delamere J, Mlawer E, Shephard M, Clough S and Collins W (2008), Radiative forcing by long-lived greenhouse gases: Calculations with the AER radiative transfer models. *Journal of Geophysical Research*, 113:D13103. doi:10.1029/2008JD009944.

IPCC (2007), *Climate Change 2007, The Physical Science Basis. Contribution of Working Group I to the Fourth Assessment Report of the Intergovernmental Panel on Climate Change* [Solomon, S., D. Qin, M. Manning, Z. Chen, M. Marquis, K.B. Averyt, M. Tignor and H.L. Miller (eds.)]. *Cambridge University Press*, Cambridge, United Kingdom and New York, NY, USA.

Islam S, Tang Y and Jackson P (2013), Asian monsoon simulations by Community Climate Models CAM4 and CCSM4, *Climate Dynamics*, 41(9-10):2617-2642. doi:10.1007/s00382-013-1752-6

Jin EK, Kinter JL, Wang B, Park CK, Kang IS, Kirtman BP, Kug JS, Kumar A, Luo JJ, Schemm J, Shukla J and Yamagata T (2008), Current status of ENSO prediction skill in coupled ocean-atmosphere models, *Climate Dynamics*, 31(6):647-664. doi:10.1007/s00382-008-0397-3.

Joseph R and Nigam S (2006), ENSO evolution and teleconnections in IPCC's twentieth-century climate simulations: realistic representation? *Journal of Climate*, 19:4360-4377. doi:10.1175/JCLI3846.1

Jhun JG and Lee EJ (2004), A new East Asian winter monsoon index and associated characteristics of winter monsoon. *Journal of Climate*, 17:711-726.

Ju J and Slingo J (1995), The Asian summer monsoon and ENSO. *Quarterly Journal of the Royal Meteorological Society*, 121:1133-1168.

Kalnay E and Toth Z (2003), Bred Vectors of the Zebiak-Cane Model and Their Application to ENSO Predictions. *Journal of Climate*, 16:40-56.

- Kanamitsu M and Krishnamurti TN (1978), Northern summer tropical circulation during drought and normal rainfall months. *Monthly Weather Review*, 106:331-347.
- Kang IS, Jin K, Wang B, Lau KM, Shukla J, Krishnamurthy V, Schubert SD, Wailser DE, Stern WF, Kitoh A, Meehl GA, Kanamitsu M, Galin VY, Satyan V, Park CK and Liu Y (2002), Intercomparison of the climatological variations of Asian summer monsoon precipitation simulated by 10 GCMs. *Climate Dynamics*, 19:383-395.
- Kang IS, Lee JY and Park CK (2004), Potential predictability of summer mean precipitation in a dynamical seasonal prediction system with systematic error correction. *Journal of Climate*, 17:834-844.
- Kang IS and Shukla J (2006), Dynamic seasonal prediction and predictability (Chap. 15). *The Asian Monsoon, Springer Praxis, Chichester*, 585-612.
- Kiehl JT, and Gent PR (2004), The Community Climate System Model, version 2. *Journal of Climate*, 17:3666-3682.
- Kirtman BP and Shukla J (2000), Influence of the Indian summer monsoon on ENSO. *Quarterly Journal of the Royal Meteorological Society*, 126:213-239.
- Kistler R, Kalnay E, Collins W, Saha S, White G, Woollen J, Kalnay E, Chelliah M, Ebisuzaki W, Kanamitsu M, Kousky V, Dool H, Jenne R and Fiorino M (2001), The NCEP–NCAR 50–Year Reanalysis: Monthly Means CD–ROM and Documentation. *Bulletin of the American Meteorological Society*, 82:247-267. doi:10.1175/1520-0477(2001)082<0247:TNNYRM>2.3.CO;2

- Kitoh A and Arakawa O (1999), On overestimation of tropical precipitation by an atmospheric GCM with prescribed SST. *Geophysical Research Letter*, 26:2965-2968.
- Kleeman R, Tang Y and Moore AM (2003), The calculation of climatically relevant singular vectors in the presence of weather noise as applied to the ENSO problem. *Journal of Atmospheric Science*, 60:2856-2868.
- Kosaka Y, Chowdary JS, Xie SP, Min YM and Lee JY (2012), Limitations of seasonal predictability for summer climate over East Asia and the Northwestern Pacific. *Journal of Climate*, 25:7574-7589.
- Kousky VE and Kayano MT (1994), Principal modes of outgoing longwave radiation and 250 mb circulation for the South American sector. *Journal of Climate*, 7:1131-1143.
- Kripalani RH and Kulkarni A (1999), Climatology and variability of historical Soviet snow depth data: some new perspectives in snow-Indian monsoon teleconnections. *Climate Dynamics*, 15:475-489.
- Kripalani RH, Oh JH, Kulkarni A, Sabade SS and Chaudhari HS (2007), South Asian summer monsoon precipitation variability: Coupled climate model simulations and projections under IPCC AR4. *Theoretical Applied Climatology*, 90:133-159.
doi:10.1007/s00704-006-0282-0
- Krishnamurti TN, Bedi HS, Subramaniam M (1989), The summer monsoon of 1987. *Journal of Climate*, 2:321-340.
- Krishnamurthy V and Shukla J (2000), Intraseasonal and interannual variability of rainfall over India. *Journal of Climate*, 13:4366-4377.

- Krishnamurthy V and Shukla J (2008), Seasonal persistence and propagation of intraseasonal patterns over the Indian monsoon region. *Climate Dynamics*, 30, 353-369.
- Kumar K, Hoerling M and Rajagopalan B (2005), Advancing dynamical predictions of the Indian monsoon rainfall. *Geophys Res Lett* 32:L08704. doi:10.1029/2004GL021979
- Kulkarni MA, Acharya N, Kar SC, Mohanty UC, Tippett MK, Robertson AW, Luo JJ and Yamagata T (2011), Probabilistic Prediction of Indian Summer Monsoon Rainfall Using Global Climate Models, *Theoretical and Applied Climatology*, 107(3-4):441-450. doi:10.1007/s00704-011-0493-x
- Kug JS, Ham YG, Lee EJ and Kang IS (2011), Empirical singular vector method for ensemble El Niño–Southern Oscillation prediction with a coupled general circulation model. *Journal of Geophysical Research*, 116:C08029.
- Liang J, Yang S, Hu ZZ, Huang B, Kumar A, Zhang Z (2009), Predictable patterns of Asian and Indo-Pacific summer precipitation in the NCEP CFS. *Climate Dynamics*, 32:989-1001.
- Lacono M, Delamere J, Mlawer E, Shephard M, Clough S and Collins W (2008), Radiative forcing by long-lived greenhouse gases: Calculations with the AER radiative transfer models. *Journal of Geophysical Research*, 113D, 13103.
- Lau NC and Nath MJ (2000), Impact of ENSO on the variability of the Asian-Australian monsoons as simulated in GCM experiments. *Journal of Climate*, 13:4287-4309.
- Lau KM and Li MT (1984), The monsoon of east Asia and its global associations - A survey. *Bulletin of the American Meteorological Society*, 65:114-125.

- Lal M, Bengtsson L, Cubash U, Esch M, and Schlese U (1995), Synoptic scale disturbances of the Indian summer monsoon as simulated in a high resolution climate model. *Climate Research*, 5:243-258.
- Lee JY, Wang B, Kang IS, Shukla, Kumar A, Kug JS, Schemm JKE, Luo JJ, Yamagata T, Fu X, Alves O, Stern B, Rosati T and Park CK (2010), How are seasonal prediction skills related to models' performance on mean state and annual cycle? *Climate Dynamics*, doi:10.1007/s00382-010-0857-4
- Lee WJ and Coauthors (2009), APEC Climate Center for climate information services, *APCC Final Report* (www.apcc21.org/eng/research/pub/repo/japcc040602_lst.jsp)
- Leith CE (1974), Theoretical skill of Montecarlo forecasts. *Monthly Weather Review*, 102: 409-418.
- Leutbecher M and Palmer TN (2008), Ensemble forecasting. *Journal of Computational Physics*, 227(7):3515-3539.
- Li C and Yanai M (1996), The onset and interannual variability of the Asian summer monsoon in relation to land-sea thermal contrast, *Journal of Climate*, 9:358-375.
- Li T and Hogan TF (1999), The Role of the Annual-Mean Climate on Seasonal and Interannual Variability of the Tropical Pacific in a Coupled GCM. *Journal of Climate*, 12:780-792.
- Liang J, Yang S, Hu ZZ, Huang B, Kumar A, Zhang Z (2009), Predictable patterns of the Asian and Indo-Pacific summer precipitation in the NCEP CFS. *Climate Dynamics*, 32:989-1001.

- Lin JL (2007), The double-ITCZ problem in IPCC AR4 coupled GCMs: ocean-atmosphere feedback analysis. *Journal of Climate*, 20:4497-4525. doi:10.1175/JCLI4272.1
- Liu X, Easter RC, Ghan SJ, Zaveri R, Rasch P, Shi X, Lamarque JF, Gettelman A, Morrison H, Vitt F, Conley A, Park S, Neale R, Hannay C, Ekman AML, Hess P, Mahowald N, Collins W, Iacono MJ, Bretherton CS, Flanner MG and Mitchell D (2011), Toward a minimal representation of aerosol direct and indirect effects: model description and evaluation, *Geoscientific Model Development Discussion*, 4:3485-3598. doi:10.5194/gmdd-4-3485-2011
- Lorenz EN (1963), Deterministic Nonperiodic Flow, *Journal of the Atmospheric Sciences*, 20(2):130-141.
- Lorenz EN (1965), A study of the predictability of a 28-variable atmospheric model. *Tellus*, 17:321-333.
- Loschnigg JG and Webster PJ (2000), A coupled ocean-atmospheric system of SST regulation for the Indian Ocean. *Journal of Climate*, 13:3342-3360.
- Malik N, Marwan N and Kurths J (2010), Spatial structures and directionalities in monsoonal precipitation over south Asia. *Nonlinear Process Geophysics*, 17:371-381.
- Manganello, Julia V, Huang and Bohua (2008), The influence of systematic errors in the Southeast Pacific on ENSO variability and prediction in a coupled GCM. *Climate Dynamics*, DOI:10.1007/s00382-008-0407-5
- Meehl GA (1994), Influence of the land surface in the Asian summer monsoon: Internal conditions versus internal feedback, *Journal of Climate*, 7:1033-1049.

- Meehl GA and Arblaster JM (1998), The Asian-Australian monsoon and El Niño-Southern Oscillation in the NCAR climate system model. *Journal of Climate*, 11:1356-1385
- Meehl GA and Arblaster JM (2002), Indian monsoon GCM sensitivity experiments testing tropospheric biennial oscillation transition conditions. *Journal of Climate*, 15:923-944.
- Meehl GA, Covey C, McAvaney B, Latif M and Stouffer RJ (2005), Overview of the coupled model intercomparison project. *Bulletin of the American Meteorological Society*, 86:89-93. doi:10.1175/BAMS-86-1-89
- Meehl, GA, Washington WM, Santer BD, Collins WD, Arblaster JM, Hu A, Lawrence DM, Teng H, Buja LE and Strand WG (2006), Climate change projections for the twenty-first century and climate change commitment in the CCSM3. *Journal of Climate*, 19:2597-2616.
- Meehl GA, Arblaster JM, Caron JM, Annamalai H, Jochum M, Chakraborty A and Murtugudde R (2012), Monsoon Regimes and Processes in CCSM4. Part I: The Asian–Australian Monsoon. *Journal of Climate*, 25(8):2583-2608.
- Moore AM and Kleeman R (1996), The dynamics of error growth and predictability in a coupled model of ENSO. *Quarterly Journal of the Royal Meteorological Society*, 122:1405-1446.
- Mooley DA and B. Parthasarathy (1984), Fluctuations in All-India summer monsoon rainfall during 1871-1978. *Climatic Change*, 6:287-301.

- Molteni F and Palmer TN (1993), Predictability and finite time instability of the northern winter circulation. *Quarterly Journal of the Royal Meteorological Society*, 119:269-298.
- Morrison H and Gettelman A (2008), A new two-moment bulk 688 stratiform cloud micro physics scheme in the NCAR Community Atmosphere Model (CAM3), Part I: Description and numerical tests. *Journal of Climate*, 21:3642-3659.
- Moron V (1995), Variability of the African convection centre as viewed by outgoing longwave radiation records and relationships with sea surface temperature patterns. *International Journal of Climatology*, 15:25-34.
- Mureau R, Molteni F and Palmer TN (1993), Ensemble prediction using dynamically conditioned perturbations. *Quarterly Journal of the Royal Meteorological Society*, 119:299-323.
- Neale RB, Jochum M and Richter JH (2008), The impact of convection on ENSO: From a delayed oscillator to a series of events. *Journal of Climate*, 21:5904-5924.
- Neale RB, Richter JH, Andrew JC, Park S, Lauritzen PH, Gettelman A, Williamson DL, Rasch PJ, Vavrus SJ, Taylor MA, Collins WD, Zhang M, Lin S (2010a), Description of the NCAR Community Atmosphere Model (CAM 4.0). *NCAR Technical Note*, NCAR/TN-485+STR, National Center for Atmospheric Research, Boulder, Colorado.
- Neale RB and Coauthors (2010b), Description of the NCAR Community Atmosphere Model (CAM 5.0). *NCAR Technical Note*, NCAR/TN-486+STR, National Center for Atmospheric Research, Boulder, Colorado.

- Nigam S (1994), On the dynamical basis for the Asian summer monsoon rainfall-El Niño relationship. *Journal of Climate*, 7:1750-1771.
- Palmer TN, Molteni F, Mureau R, Buizza R, Chapelet P and Tribbia J (1993), Ensemble prediction. Proceedings of the ECMWF Seminar on Validation of models over Europe: vol. I, *ECMWF*, Shinfield Park, Reading, RG2 9AX, UK.
- Palmer TN, Brankovic C, Viterbo P, Miller MJ (1992), Modelling interannual variations of summer monsoons. *Journal of Climate*, 5:399-417.
- Palmer TN, Alessandri A, Andersen U, Cantelaube P, Davey M, Décluse P, Déqué M, Díez E, Doblas-Reyes FJ, Feddersen H, Graham R, Gualdi S, Guérémy JF, Hagedorn R, Hoshen M, Keenlyside N, Latif M, Lazar A, Maisonnavé E, Marletto V, Morse AP, Orfila B, Rogel P, Terres JM and Thomson MC (2004), Development of a European multimodel ensemble system for seasonal-to-interannual prediction (DEMETER). *Bulletin of the American Meteorological Society*, 85:853-872.
- Park S and Bretherton CS (2009), The University of Washington shallow convection and moist turbulence schemes and their impact on climate simulations with the Community Atmosphere Model. *Journal of Climate*, 22:3449-3469.
- Parthasarathy B, Munot AA and Kothawale DR (1995), All India monthly and seasonal rainfall series: 1871–1993. *Theoretical Applied Climatology*, 49:217-224.
doi:10.1007/BF00867461

- Pokhrel S, Chaudhari HS, Saha SK, Dhakata A, Yadav RK, Salenke K, Mahaptra S and Rao SA (2012), ENSO, IOD and Indian summer monsoon in the NCEP climate forecast system. *Climate Dynamics*, doi:10.1007/s00382-012-1349-5
- Randall DA, Wood RA, Bony S, Colman R, Fichefet T, Fyfe J, Kattsov V, Pitman A, Shukla J, Srinivasan J, Stouffer RJ, Sumi A and Taylor KE (2007), Climate Models and Their Evaluation. In: *Climate Change 2007: The Physical Science Basis. Contribution of Working Group I to the Fourth Assessment Report of the Intergovernmental Panel on Climate Change. Cambridge University Press, Cambridge, United Kingdom and New York, NY, USA*
- Rajeevan M, Unnikrishnan CK and Preethi B (2011), Evaluation of the ENSEMBLES multi-model seasonal forecasts of Indian summer monsoon variability. *Climate Dynamics*, doi:10.1007/s00382-011-1061-x.
- Rasmusson EM and Carpenter TH (1983), The relationship between eastern equatorial Pacific sea surface temperature and rainfall over India and Sri Lanka. *Monthly Weather Review*, 111:517-528.
- Rayner NA, Parker DE, Horton EB, Folland CK, Alexander LV, Rowell DP, Kent EC and Kaplan A (2003), Global analyses of sea surface temperature, sea ice, and night marine air temperature since the late nineteenth century. *Journal of Geophysical Research*, 108:4407. doi:10.1029/2002JD002670
- Reynolds RW, Rayner NA, Smith TM, Stokes DC and Wang W (2002), An improved in situ and satellite SST analysis for climate. *Journal of Climate*, 15:1609-1625.

- Richter J and Rasch P (2008), Effects of convective momentum transport on the atmospheric circulation in the Community Atmosphere Model, version 3. *Journal of Climate*, 21:1487-1499.
- Ropelewski CF and Halpert MS (1987), Global and regional scale precipitation patterns associated with the El Niño/Southern Oscillation, *Monthly Weather Review*, 115:1606-1626.
- Rowell DP, Folland CK, Maskell K and Ward MN (1995), Variability of summer rainfall over tropical north Africa (1906-92): Observations and modelling. *Quarterly Journal of the Royal Meteorological Society*, 121:669-674.
- Rodwell MJ and BJ Hoskins (1995), A Model of the Asian Summer Monsoon. Part II: Cross-Equatorial low and PV Behavior. *Journal of Atmospheric Science*, 52:1341-1356.
- Saji NH, Goswami BN, Vinayachandran PN and Yamagata T (1999), A dipole mode in the tropical Indian Ocean. *Nature*, 401:360-363.
- Saha SK, Halder S, Krishna Kumar K and Goswami BN (2011), Pre-onset land surface processes and 'internal' interannual variabilities of the Indian summer monsoon. *Climate Dynamics*, 36:2077-2089.
- Saha S, Nadiga S, Thiaw C, Wang J, Wang W, Zhang Q, Van-den Dool HM, Pan HL, Moorthi S, Behringer D, Stokes D, Peña M, Lord S, White G, Ebisuzaki W, Peng P and Xie P (2006), The NCEP Climate Forecast System. *Journal of Climate*, 19:3483-3517. doi:10.1175/JCLI3812.1

- Schmetz J and Liu Q (1988), Outgoing longwave radiation and its diurnal variation at regional scales derived from Meteosat. *Journal of Geophysical Research*, 93(D9):11192-11204.
- Schott FA, Xie SP, McCreary J (2009), Indian Ocean circulation and climate variability. *Reviews of Geophysics*, 47:RG1002. doi:10.1029/2007RG000245
- Sikka DR (1999), Monsoon drought in India. Joint *COLA/CARE Technical Report No. 2*. Center for Ocean–Land–Atmosphere Studies and Center for the Application of Research on the Environment, 93pp
- Sikka DR (1980), Some aspects of the large scale fluctuations of summer monsoon rainfall over India in relation to fluctuations in the planetary and regional scale circulation parameters. *Proceedings of the Indian Academy of Sciences - Earth and Planetary Sciences*, 89(2):179-195.
- Sikka DR and Gadgil S (1980), On the maximum cloud zone and the ITCZ over Indian longitudes during the southwest monsoon, *Monthly Weather Review*, 108:1840-1853.
- Shukla J (1981), Dynamical predictability of monthly means. *Journal of Atmosphere Science*, 38:2547-2572.
- Shukla J and Mintz Y (1982), Influence of Land-Surface Evapotranspiration on the Earth's Climate. *Science*, 215:1498-1501.
- Shukla J and Wallace JM (1983), Numerical simulation of the atmospheric response to equatorial Pacific sea surface temperature anomalies. *Journal of Atmospheric Science*, 40:1613-1630.

- Shukla J and Paolino DA (1983), The Southern Oscillation and long-range forecasting of the summer monsoon rainfall over India. *Monthly Weather Review*, 111:1830-1837.
- Shukla J and Mooley DA (1987), Empirical prediction of the summer monsoon rainfall over India. *Monthly Weather Review*, 115: 695-703.
- Shukla J (1987), Interannual variability of monsoons. Monsoons, Ed. J.S. Fein and P.L. Stephens, *John Wiley and Sons*, pp 399-463.
- Sperber KR, Brankovic C, Deque M, Frederiksen CS, Graham, R., Kitoh A, Kobayashi C, Palmer T, Puri K, Tennant W and Volodin E (2001), Dynamical Seasonal Predictability of the Asian Summer Monsoon. *Monthly Weather Review*, 129:2226-2248. doi:10.1175/1520-0493(2001)129<2226:DSPOTA>2.0.CO;2
- Sperber, KR, and Palmer TN (1996), Interannual tropical rainfall variability in general circulation model simulations associated with the Atmospheric Model Intercomparison Project. *Journal of Climate*, 9:2727-2750.
- Singh A, Acharya N, Mohanty UC, Robertson AW and Mishra G (2012), On the predictability of Indian Summer Monsoon Rainfall in general circulation model at different lead time, *Dynamics of Atmospheres and Oceans*, 58:108-127.
- Slingo JM and Annamalai H (2000), 1997: The El Niño of the century and the response of the Indian summer monsoon. *Monthly Weather Review*, 128:1778-1797.
- Smith RD and Gent P (2002), Reference manual for the Parallel Ocean Program (POP). *Los Alamos Unclassified Report*, LA-UR-02-2484.

- Smith RD and S Kortas (1995), Curvilinear coordinates for global ocean models. *Los Alamos Unclassified Report*, LA-UR-95-1146
- Sohn SJ, Tam CY, Ashok K and Ahn JB (2012), Quantifying the reliability of precipitation datasets for monitoring large-scale East Asian precipitation variations, *International Journal of Climatology*, doi:10.1002/joc.2380
- Soman, MK and Slingo J (1997), Sensitivity of the Asian summer monsoon to aspects of sea-surface-temperature anomalies in the tropical Pacific Ocean. *Quarterly Journal of the Royal Meteorological Society*, 123:309-336.
- Tang Y, Kleeman R and Moore A (2005), On the reliability of ENSO dynamical predictions. *Journal of Atmospheric Science*, 62(6):1770-1791.
- Tang Y, Kleeman R and Miller S (2006), ENSO predictability of a fully coupled GCM model using singular vector analysis. *Journal of Climate*, 19:3361-3377.
- Tang Y and Deng Z (2011), ENSO bred vectors and predictability in a hybrid coupled model from 1881-2000, *Journal of Climate*, 24(1):298-314.
- Trenberth KE, Jones PD, Ambenje P, Bojariu R, Easterling D, Klein TA, Parker D, Rahimzadeh F, Renwick JA, Rusticucci M, Soden B, Zhai P (2007), Observations: Surface and Atmospheric Climate Change. In: Solomon S, Qin D, Manning M, Chen Z, Marquis M, Averyt KB, Tignor M, Miller HL (ed) *Climate Change 2007: The Physical Science Basis. Contribution of Working Group I to the Fourth Assessment Report of the Intergovernmental Panel on Climate Change. Cambridge University Press, Cambridge, United Kingdom and New York, NY, USA*

- Toth Z and Kalnay E (1993), Ensemble forecasting and NMC: the generation of perturbations. *Bulletin of the American Meteorological Society*, 74:2317-2330.
- Turner AG, Inness PM, Slingo JM (2005), The role of the basic state in the ENSO-monsoon relationship and implications for predictability. *Quarterly Journal of the Royal Meteorological Society*, 131: 781-804
- Vavrus S and Waliser D (2008), An improved parameterization for simulating Arctic cloud amount in the CCSM3 climate model. *Journal of Climate*, 21:5673-5687.
- Waliser D, Seo KW, Schubert S and Njoku E (2007), Global water cycle agreement in the climate models assessed in the IPCC AR4. *Geophysical Research Letters*, 34:L16705. doi:10.1029/2007GL030675
- Walker GT (1924), Correlation in seasonal variations of weather, IV, A further study of world weather. *Monthly Weather Review*, 24:275-332.
- Walker J and Rowntree PR (1977), The effect of soil moisture on circulation and rainfall in a tropical model. *Quarterly Journal of the Royal Meteorological Society*, 103:29-46.
- Wang B and Fan Z (1999), Choice of South Asian summer monsoon indices. *Bulletin of the American Meteorological Society*, 80:629-638.
- Wang B, Wu R and Lau KM (2001), Interannual variability of the Asian summer monsoon: Contrasts between the Indian and the western North Pacific-East Asian monsoons. *Journal of Climate*, 15:4073-4090.

- Wang B, Wu R and Li T (2003), Atmosphere warm ocean interaction and its impacts on the Asian-Australian monsoon variation. *Journal of Climate*, 16, 1195-1211.
- Wang B, Kang IS and Li JY (2004), Ensemble simulation of Asian-Australian monsoon variability by 11 AGCMs. *Journal of Climate*, 17:803-818.
- Wang B, Ding QH, Fu XH, Kang IS, Jin K, Shukla J and Doblas-Reyes F (2005), Fundamental challenge in simulation and prediction of summer monsoon rainfall. *Geophysical Research Letters*, 32:L15711.
- Wang B, Bao Q, Hoskins B, Wu G and Liu Y (2008), Tibetan Plateau warming and precipitation change in East Asia. *Geophysical Research Letters*, 35:L14702. doi:10.1029/2008GL034330.
- Wang B, Lee JY, Kang IS, Shukla J, Park CK, Kumar A, Schemm J, Cocke S, Kug JS, Luo JJ, Zhou T, Fu X, Yun WT, Alves O, Jin EK, Kinter J, Kirtman B, Krishnamurti T, Lau NC, Lau W, Liu P, Pegion P, Rosati T, Schubert S, Stern W, Suarez M and Yamagata T (2009), Advance and prospectus of seasonal prediction: assessment of the APCC/CliPAS 14-model ensemble retrospective seasonal prediction (1980-2004). *Climate Dynamics*, 33:93-117. DOI 10.1007/s00382-008-0460-0
- Webster PJ (1987), The elementary monsoon. In: Fein JS, Stephens PL (eds) *Monsoons*. John Wiley, New York, NY, pp 3-32.
- Webster PJ and Yang S (1992), Monsoon and ENSO: selectively interactive systems. *Quarterly Journal of the Royal Meteorological Society*, 118:877-926.

- Webster PJ, Moore A, Loschnigg J and Leban M (1999), Coupled dynamics in the Indian Ocean during 1997-1998. *Nature*, 401:356-360.
- Webster, PJ, VO M, Palmer TN, Shukla J, Tomas RA, Yanai M and Yasunari T (1998), Monsoons: processes, predictability and the prospects for prediction. *Journal of Geophysical Research*, 103:14451-14510.
- Wu X, Liang X and Zhang GJ (2003), Seasonal migration of ITCZ precipitation across the equator: Why can't GCMs simulate it? *Geophysical Research Letters*, 30(15):1824-1828.
- Wu R and Kirtman B (2004), Impacts of the Indian Ocean on the Indian Summer Monsoon-ENSO Relationship. *Journal of Climate*, 17, 3037-3054.
- Wu G, Liu Y, Wang T, Wan R, Liu X, Li W, Wang Z, Zhang Q, Duan A and Liang X (2007), The Influence of Mechanical and Thermal Forcing by the Tibetan Plateau on Asian Climate. *Journal of Hydrometeorology*, 8:770-789.
- Wu R, Chen JL and Chen W (2012), Different types of ENSO influences on the Indian summer monsoon variability. *Journal of Climate*, 25:903-920.
- Xie SP (1994), On the Genesis of the Equatorial Annual Cycle. *Journal of Climate*, 7:2008-2013.
- Xie P and Arkin PA (1997), Global Precipitation: A 17-Year Monthly Analysis Based on Gauge Observations, Satellite Estimates, and Numerical Model Outputs. *Bulletin of the American Meteorological Society*, 78:2539-2558.

- Xue Y, Cane MA and Zebiak SE (1997a), Predictability of a coupled model of ENSO using singular vector analysis. PartI: optimal growth in seasonal background and ENSO cycles. *Monthly Weather Review*, 125:2043-2056.
- Xue Y, Sales F, Li WP, Mechoso CR, Nobre CA and Juang HM (2006), Role of land surface processes in South American monsoon development. *Journal of Climate*, 19:741-762.
- Xue Y, Cane MA and Zebiak SE (1997b), Predictability of a coupled model of ENSO using singular vector analysis. PartII: optimal growth and forecast skill. *Monthly Weather Review*, 125:2057-2073.
- Yasunari T (1990), Impact of Indian monsoon on the coupled atmosphere/ocean systems in the tropical Pacific. *Meteorology and Atmospheric Physics*, 44:29-41.
- Younas W and Tang Y (2013), PNA Predictability at Various Time Scales. *Journal of Climate*, 26:9090-9114. doi:10.1175/JCLI-D-12-00609.1
- Yoo JH and Kang IS (2005), Theoretical examination of a multi-model composite for seasonal prediction. *Geophysical Research Letters*, 32:L18707.
- Zhou X, Tang Y and Deng Z (2007), The impact of nonlinear atmosphere on the fastest error growth of ENSO prediction. *Climate Dynamics*, 30:519-531. DOI: 10.1007/s00382-007-0302-5.